Active Power Damping Control using Renewable Energy Sources

by

Mayur Basu

A dissertation submitted to the Graduate Faculty of
Auburn University
in partial fulfillment of the
requirements for the Degree of
Doctor of Philosophy

Auburn, Alabama
December 9, 2023

Approvals:

Dr. Eduard Muljadi, Chair, Professor, Department of Electrical and Computer Engineering
Dr. R. Mark Nelms, Professor and Chair of Department of Electrical and Computer Engineering
Dr. Mark S. Halpin, Professor, Department of Electrical and Computer Engineering
Dr. Yin Sun, Associate Professor, Department of Electrical and Computer Engineering
University Reader, Dr. Jordan Roberts, Senior Lecturer, Department of Mechanical Engineering

Abstract

This Ph.D. report navigates the global energy landscape shaped by ambitious carbon reduction goals. Solar photovoltaic (PV) and wind energy, driving the growth of renewable energy sources (RESs), signal a significant transformation in power systems. Despite their benefits, the intermittent nature of these sources poses challenges for stability. Inverter-based resources (IBRs), featuring power electronic converters, differ from conventional synchronous machines, impacting system inertia and dynamics. Consequently, grid codes mandate RESs to comply with stringent requirements like ride-through capabilities, frequency regulation, and power regulation.

The report proposes a dual Power Oscillation Damping (POD) scheme for RESs to address these challenges. This innovative approach prioritizes active POD during faults, strategically allocating the remaining capacity for reactive POD in a two-area system. Notably, an Automatic Voltage Regulator tailored for Type 5 wind farms, with a synchronous generator and torque converter, yields substantial damping improvements due to dynamics resembling conventional generators.

A comparative study using Prony analysis identifies exponential sinusoids in the damped curve, revealing the Type 5 wind turbine's superior damping capabilities. This underscores its pivotal role in fortifying modern power grids. The report advocates for continued research to optimize RES contributions to the evolving power landscape.

Acknowledgements

I would like to express my deepest gratitude to several individuals who have played instrumental roles in completing my Ph.D. dissertation. First and foremost, I extend my heartfelt thanks to my late mother, Arati Basu, whose unwavering encouragement and support throughout my life have been a source of inspiration. Her enduring influence remains a guiding force in my academic journey. I am profoundly grateful to my father, Gouranga Kumar Basu, for his consistent care and dedication to our family. His support has been a pillar of strength, enabling me to focus on my academic pursuits. Their encouragement and understanding have been invaluable, contributing significantly to my academic endeavors. I owe a debt of gratitude to my esteemed supervisor, Dr. Eduard Muljadi, whose constant mentorship has been pivotal in shaping my confidence and knowledge. Dr. Jinho Kim was an inspiration for me throughout my time at Auburn University. His guidance has been instrumental in my academic and professional development. I extend my thanks to Dr. Mark Halpin for the impactful power system classes that provided me with a wealth of confidence, ideas, and in-depth knowledge. His teachings have been a cornerstone of my academic journey. A heartfelt acknowledgment is due to Dr. Robert Nelms for his unwavering support and attentiveness to every departmental need. His prompt responses and constructive reviews have played a crucial role in shaping me as both an educator and a student. I express my appreciation to Dr. Vahan Gevorgian and Dr. Weihang Yan of NREL for granting me the opportunity to work on a project for NREL. This experience has significantly enriched my capabilities as a Power System Engineer. In conclusion, I am grateful to each individual mentioned for their invaluable contributions and unwavering support, which have collectively fueled the successful completion of my Ph.D. dissertation.

Table of Contents

List of Figures

List of Abbreviations

IBR	Inverter-based resources
TSO	Transmission system operators
ISO	Independent system operators
RRO	Regional reliability organization
RES	Renewable energy sources
POD	Power Oscillation Damping
WPP	Wind Power Plant
FRT	Fault ride-through
BESS	Battery energy storage
FACTS	Flexible AC transmission system
AVR	Automatic Voltage Regulators
MPPT	Maximum Power Point Tracking
PSS	Power System Stabilizer
SG	Synchronous Generator
GSC	Grid-side Converter
POI	Point of Interconnection
BLE	Brushless Excitor
DR	Duty Ratio

Chapter 1 Introduction

The recent proliferation of inverter-based resources (IBR) forced the regional reliability organization (RRO) to make specific changes in modern grid codes. In the year 2021, there was a global grid connection of 167.8 Gigawatts (GW) of solar capacity, which reflects a growth of 21% in comparison to the previous year's addition of 139.2 GW. The increase in the adoption of solar photovoltaic (PV) signifies the transition of international markets towards renewable energy systems. As of 2021, China and the United States dominated the global PV market, with a combined cumulative PV capacity of 429 GW, of which China accounts for 307 GW and the United States accounts for 122 GW [1]. We expect solar PV growth accelerates the most from now to 2050, among other renewable energy sources (RESs) [2].
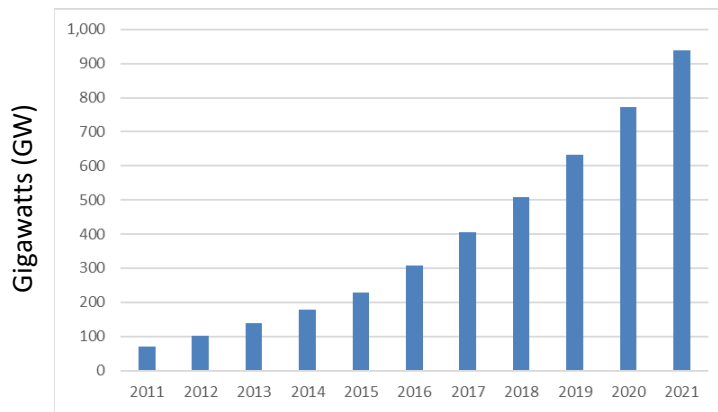
Fig. 1.1: Global cumulative installed solar PV capacity in GW from 2011-2021[1]
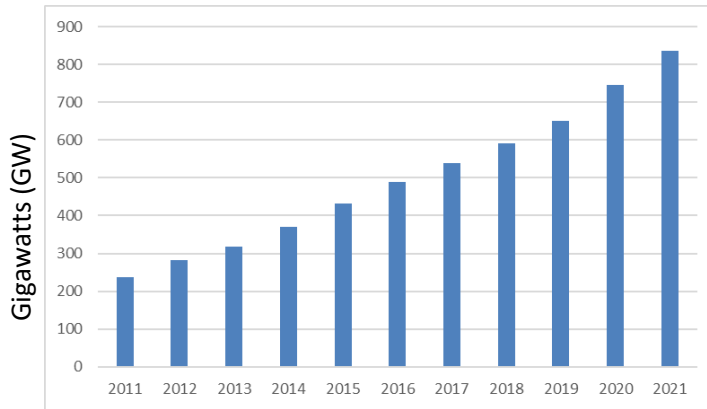
Fig. 1.2: Global cumulative installed Wind power capacity in GW from 2011-2021[3]

According to the Global Wind Energy Council (GWEC), the global onshore wind capacity saw an addition of 72.5 GW in 2021, thereby increasing the cumulative onshore wind capacity to 780 GW. Although Europe, Latin America, Africa & Middle East had a remarkable year for new onshore installations, the overall installation numbers in 2021 are still 18% lower than the previous year. This decline is attributed to the deceleration of onshore wind growth in the two leading wind power markets worldwide, namely China and the US. However, in contrast to onshore wind, 2021 witnessed a remarkable milestone in the offshore wind sector, with a global grid connection of 21.1 GW of offshore wind capacity. This achievement set a record in the history of offshore wind worldwide and elevated the total global offshore wind capacity to 57.2 GW by the end of 2021 [3]. In ERCOT, the installed capacity of wind accounts for 23.3% of the total generating capacity in 2020; however, the instantaneous wind penetration level reached 59.3% in May 2020 [4]. A similar example is the Southwest Power Pool (SPP), where the installed capacity of wind accounts for 24.9% of the total generating capacity, but the instantaneous penetration level of wind reached 72.4% in April 2020 [5]–[6]. The Global Electricity Review 2022 reports that, in 2021, wind and solar energy sources contributed to more than 10% of the total electricity generation worldwide, marking the first time this threshold has been surpassed. [7]

However, the intermittent nature of the RESs is one of the major concerns in power system studies. Moreover, the inertial and dynamic characteristics of IBRs are much different compared to the conventional synchronous machines-based power generations. Because of the increased RES penetration levels, power system stability and reliability have become the major concerns for modern power grids. Utility-scale RESs are now required to meet specific grid code requirements and sometimes to behave like conventional power plants - capable of supporting the power system when requested to maintain stability [8]–[9].

Unlike conventional generators, PV plants do not possess the inherent capability to provide an inertial response, making the grid system more vulnerable during large-frequency excursions [6]. IBRs have power electronic converters at the grid interface, which decouples the dynamic of the PV plant from the AC grid system. IBRs affect the system's dynamic behavior by i) system inertia reduction, ii) withdrawal of governor response, and iii) decrease in synchronizing and damping torques [10]. Moreover, IBRs operate on maximum power point tracking. Hence, it cannot provide increased power output when needed [11]. Therefore, it is apparent that the PV plants can neither provide the inertial response nor participate in frequency regulation. Thus, technical issues regarding frequency regulation, voltage stability, and fault ride-through (FRT) have become an integral part of power systems with high penetrated PV plants [12]−[14]. Hence, shifting the focus to auxiliary control schemes of PV plants has become imminent to provide some promising solutions to its shortcomings [15]−[16].

On the other hand, the characteristics of the Wind Power Plants (WPPs) are also entirely different from conventional power plants, such as hydraulic, nuclear, or thermal [17]. Due to this, the TSOs are also proposing auxiliary services for the WPPs in the recent grid codes. According to these codes, WPPs must comply with requirements including ride-through capabilities [18],

frequency regulation [19], and active and reactive power regulation [20]. In the future, more WPP contributions is required by the RROs. The capability to damp power system oscillations plays a vital role in securing the extensive deployment of renewables. A new draft of the Spanish grid code is already considering inertia emulation and power oscillation damping for their newly installed WPPs [21].

Damping out low-frequency electromechanical power oscillations (typically 0.1 - 2 Hz) is one of the major modern grid problems due to weak grid (long transmission), control interactions, and less available inertia in the power systems (as the level of penetration of IBRs increases overtime). Regarding this, energy storage systems (ESSs), e.g., battery energy storage (BESS), super-capacitor storage (SCESS), and flywheel energy storage have been used as auxiliary devices with IBRs to provide oscillation damping during any frequency excursions [22]–[23]. Additional Flexible AC transmission system (FACTS) devices are installed in the middle of the transmission line to provide reactive power in the system for better power transfer capability and improved power oscillation damping [24]–[26]. All this equipment comes with a requirement of additional capital cost. A better solution would have been if the IBRs' active and reactive power could be modulated for the same purpose without further capital investment.

1.1 Dissertation Outline

This comprehensive report not only delves into the implementation of a dual power oscillation damper (POD) in IBRs but also extends its investigation into the dynamics of Automatic Voltage Regulators (AVRs) for Type 5 wind turbine synchronous generators. Chapter 2 rigorously examines the efficiency of dual POD within a utility-scale photovoltaic (PV) plant, conducting a meticulous comparative study involving active and reactive power damping. Moving

forward, Chapter 3 elevates the scope to Type 4 wind power plants, showcasing a notable enhancement in oscillation damping. Chapter 4 introduces a coordinated control scheme for a utility-scale PV power plant and a WPP, strategically synchronized to optimize their complementary characteristics. This scheme integrates two distinct power oscillation damping (POD) control loops for active and reactive power modulation in both PV and WPP. The proposed coordinated scheme, simulated using PSCAD, demonstrates remarkable efficacy in supporting voltage stability and facilitating rapid recovery post-grid faults in high-penetration renewable energy systems. Chapter 5 represents a significant advancement in the theoretical underpinnings, with an in-depth exploration of the dynamic model of various types of AVRs tailored for Type 5 synchronous generators. The chapter proceeds to develop dynamic models of the chosen AVRs using electromagnetic transient modeling software "PSCAD." Case studies within this chapter substantiate the chosen AVR models' effectiveness, emphasizing their impact on damping power oscillations within a two-area model. In the final chapter, Chapter 6, the culmination of the oscillation damping data is subjected to Prony analysis. This rigorous processing allows for the identification of exponential sinusoids present in the output, unveiling the damping provided by all the schemes proposed in this dissertation. Remarkably, the findings underscore the superiority of Type 5 wind turbines, attributing their efficacy to increased inertia and dynamics akin to traditional wind turbines.

This narrative reflects a seamless integration of theoretical exploration, simulation, and empirical analysis, positioning the proposed dual POD and AVR models as transformative solutions in the dynamic landscape of power system oscillation damping. The limitations of current inverter levels in IBRs, identified through these studies, emphasize the importance of ongoing research and development in the pursuit of more robust renewable energy systems.

1.2 Distribution of Publications

A list of publications related to the thesis is given below. It contains 3 journal papers and 4 conference papers. They have been published or under review, where the journal papers are marked as J1-J3 and the conference papers are marked as C1-C4.

Journal Papers:

J1. M. Basu, V. R. Mahindara, J. Kim, R. M. Nelms and E. Muljadi, "Comparison of Active and Reactive Power Oscillation Damping With PV Plants," in IEEE Transactions on Industry Applications, vol. 57, no. 3, pp. 2178-2186, May-June 2021, doi: 10.1109/TIA.2021.3059810.

J2. M. Basu, J. Kim, R. M. Nelms and E. Muljadi, "Coordination of Utility-Scale PV Plant and Wind Power Plant in Interarea-Oscillation Damping," in IEEE Transactions on Industry Applications, vol. 59, no. 4, pp. 4744-4751, July-Aug. 2023, doi: 10.1109/TIA.2023.3257829.

J3. M. Basu, W. Yan, V. Gevorgian and E. Muljadi, "Development of Dynamic Model of Automatic Voltage Regulator (AVR) for a Type 5 Wind Turbine Generator," in Renewable Energy, Elsevier (submitted).

Conference Papers:

C1. M. Basu, V. R. Mahindara, J. Kim and E. Muljadi, "Effect of high penetrated reactive power support-based Inverter-Based-Resources on the power stability of microgrid distribution system during faults," 2020 IEEE Industry Applications Society Annual Meeting, Detroit, MI, USA, 2020, pp. 1-4, doi: 10.1109/IAS44978.2020.9334877.

C2. M. Basu, J. Kim, R. M. Nelms and E. Muljadi, "Interarea-Oscillation Damping with Dual Power Oscillation Damping Controller of a Utility-Scale Wind Power Plant," 2021 3rd International Conference on High Voltage Engineering and Power Systems (ICHVEPS), Bandung,

Indonesia, 2021, pp. 581-585, doi: 10.1109/ICHVEPS53178.2021.9601127.

C3. M. Basu, J. Kim, R. M. Nelms and E. Muljadi, "Utilization of Local Phasor Measurements for Interarea-Oscillation Damping with Utility-Scale PV Plant," 2021 IEEE Energy Conversion Congress and Exposition (ECCE), Vancouver, BC, Canada, 2021, pp. 871-876, doi: 10.1109/ECCE47101.2021.9595540.

C4. M. Basu, W. Yan, V. Gevorgian and E. Muljadi, "Inter-area Oscillation Damping with Type-5 Wind Power Plant," 2023 IEEE Green Technologies Conference (GreenTech), Denver, CO, USA, 2023, pp. 181-185, doi: 10.1109/GreenTech56823.2023.10173819.

Chapter 2
Power Oscillation Damping with PV

A PV plant's operation and dynamic characteristics are much different from conventional power plants, equipped with synchronously rotating machines (i.e., the intermittent nature, integration through power converters, and zero inertia of PV plants). Many articles [10],[27]–[28] describe the impact of high PV penetration on a power system. Reference [10] analyzed large PV plants' effect on the power system with a rapid variation of power injection of the PV. The study results indicate that the system's vulnerability increases with the increase in PV power plants' penetration. Reference [27] found that the decentralized PV plants located at a distribution network are superior to the centralized large PV plants in a power system in terms of transient stability enhancement. Reference [28] studied the impact of various penetration levels of PV plants on power system stability. The result in [28] shows that an appropriate penetration of PV can enhance the system's stability, whereas extensive penetration may deteriorate the transient stability of the system. The adverse effect of integrated PV plants on the system stability depends upon the penetration level, location, and control schemes [29]−[31]. Thus, technical issues regarding frequency regulation, voltage stability, and fault ride-through (FRT) have become an integral part of power system studies [32]−[34]. It is imminent to shift the focus of grid-supporting control schemes for PV plants regarding grid disturbances. Several countries have revised their grid codes to dictate the PV plants' ride through the voltage sags caused by grid faults [35]–[37]. For instance, the new Australian grid codes suggest the PV plants remain connected for 440 ms, even if the voltage reaches zero. Finland's grid code uses two FRT curves - one for RESs with a capacity of 0.5-10 MVA and the other for RESs greater than 10 MVA. Italy's grid code has different FRT

curves for different voltage levels at the point of interconnection (POI) [38].

2.1 Contribution of PV in auxiliary services

Replacing traditional synchronous machines with IBRs decreases the overall power system inertia and oscillation-damping capabilities. Hence, newly installed IBRs should provide the network with virtual inertia and oscillation damping by modifying its control system. Fortunately, the IBRs can provide flexible services in active and reactive control schemes due to power converter technology. FACTS devices are generally used in transmission networks to enhance the power transfer capability and damp out any low-frequency interarea oscillations [24]–[26]. Thus, as a FACTS device, PV plants inject reactive power to damp out low-frequency oscillations in [39]–[41]. An additional supplementary control loop in these PV converter controllers can achieve the same characteristics as FACTS. Reference [39] proposed coordinating PV-STATCOM and PSS to dampen oscillations. Reference [40] recommends temporary cessation of maximum power point tracking (MPPT) active power operation during the fault to utilize the full inverter capacity of the PV plant as a damping resource. The work in [41] curtailed real power to achieve damping during and after the disturbance. In [42], the effect of penetration of reactive power-based PV plant in the distribution system has been tested and promised effectiveness to maintain system resiliency during and after the faults. Despite an improvement in oscillation damping with the strategies mentioned above, the requirement to place the PV in the transmission lines or between the operating machines is not always a feasible option [43]. The time taken for damping oscillation is also relatively slow in each case. The curtailment of active power to utilize the inverter's capacity defies the idea of providing the maximum real power to the grid for more significant revenues. Fortunately, the need to operate as an oscillation damper is temporary (only when the power system

oscillation exists); thus, the temporary deviation from MPPT operation does not affect the annual energy production.

An alternate way to achieve efficient and fast damping might be to insert a supplementary damping controller in the active power injection. Regarding this, energy storage systems (ESSs), e.g., battery energy storage (BESS), super-capacitor storage (SCESS), and flywheel energy storage, have been used as auxiliary devices with IBRs to provide oscillation damping by responding to the variations of the system frequency [44]–[45]. The work in [44] examined the performance of ESSs in damping the oscillations caused by grid faults. In [45], the proposed control parameter tuning for the ESSs in coordination with the grid effectively reduces the changes, even though ESS is not an economical solution.

2.1.1 Use of Active Power modulation of PV in auxiliary services

The PV panels' active power control loop is entirely dedicated to harvesting the maximum power from the PV panels. With a proper tracking algorithm, a maximum power point tracker (MPPT), irrespective of the temperature and solar irradiance, serves that purpose for the PV plant. In some research work [46]–[47], an active power control loop has been utilized to dampen inter-area oscillation and has shown promising and fast damping performance. However, curtailment of the active power of the PV plants was common in all these cases. Using an active power control loop is not frequent as it is bound to curtail real power for providing extra power for damping. Long-term active power curtailment can adversely affect the capacity factor and lead to revenue losses. A sensible way to provide active power damping of inter-area oscillation without hampering the PV capacity might temporarily operate the PV plant's DC-DC converter in off-peak mode. This action creates extra headroom for the PV plant to dampen the oscillation faster.

2.1.2 Use of Reactive Power modulation of PV in auxiliary services

Any post-fault system with generators may lead to severe oscillation without a proper damping controller. This control has been done with the reactive power loop in [39]–[41]. Reactive power oscillation damping the reactive power loop is fed with external signals like frequency, phase angle, and bus voltage from remote signal measurements. In [43], active power modulation has been done on the MPPT controller to dampen the system effectively. Hence, combining both damping controllers can be an efficient and fast control scheme to modulate the two current loops and observe the effect of damping when both controllers act simultaneously.

2.2 The PV plant model
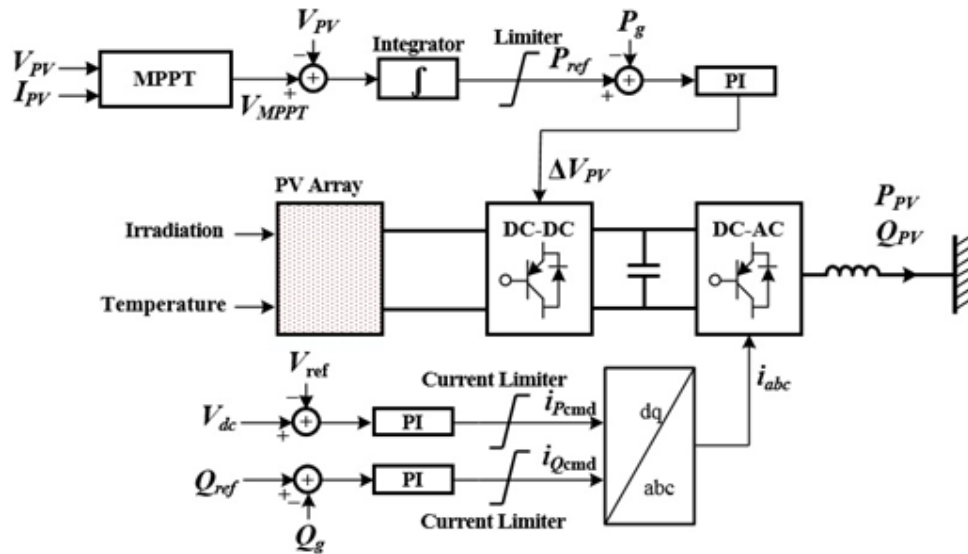
Fig. 2.1: Configuration of a PV system model.

Fig. 2.1 shows the configuration of a PV system model used in this investigation. The PV system consists of a PV array, a boost converter, a DC circuit, and a grid-side converter (GSC).

The boost converter controller employs MPPT mode to fetch the maximum power output

from the PV panels. To achieve this, perturb and observe algorithms determine a voltage reference, V_{MPPT}, for the MPPT at the array based on the line current, I_{PV}, and internal voltage, V_{PV}, of the PV array. The MPPT power reference, P_{ref}, is calculated through an integral controller based on the error between V_{MPPT} and V_{PV}. The controller then generates switching signals for the boost converter to fetch the maximum power from the array.

On the other hand, the GSC regulates the DC link voltage, V_{dc}, continuously and controls reactive power at the GSC terminal, Q_g. The GSC controller generates an active current reference, i_{Pcmd}, to achieve the former using a proportional-integral controller. For the latter, the controller generates a reactive current reference, i_{Qcmd}, through a proportional-integral (PI) controller. In this paper, the GSC is simplified as a current source. Thus, the current references are being transformed into three-phase references and fed into the current source, as shown in Fig. 2.1.

2.2.1 The proposed Control Scheme of the PV plant

This section describes the proposed features of control schemes that effectively support the electrical system during fault and post-fault conditions.

This chapter discusses and compares three POD control schemes. The damping control schemes are 1) Reactive POD control, 2) Active POD control, and 3) a combination of both Reactive and Active Power Damping control schemes. The schemes are explained below.

The PV plant has a current limit (constraint) to protect the insulated gate bipolar transistor (IGBT) switches from exceeding its current rating in the converters. During the fault, the PV plant works in Q priority mode, where the maximum current capacity is used for reactive power injection ($I_{qmax} = I_{Limit}$). Then, the available maximum and minimum active currents can be obtained by:

$$I_{pmax} = \sqrt{I_{Limit}^2 - I_{qcmd}^2} \tag{2.1}$$

$$I_{pmin} = 0 \tag{2.2}$$

P priority is enabled during normal operation. The real power will be prioritized to use the inverter's highest current capacity ($I_{pcmd} = I_{pmax} = I_{Limit}$). The value for I_{qmax} and I_{qmin} can be calculated by:

$$I_{qmax} = \sqrt{I_{Limit}^2 - I_{pcmd}^2} \tag{2.3}$$

$$I_{qmax} = -I_{qmin} \tag{2.4}$$

A. Reactive POD scheme in the GSC Controller

Fig. 2.2 shows the Reactive POD controller used in this study. To achieve this oscillation damping, the angular speed of the nearest synchronous generator, ω, is taken as the input for the damping control loop; actually, the system frequency detected by the phase-locked loop in the PV model can be used as well. Then, high-frequency components of ω are captured by a washout filter. The reactive current reference for the damping control, $i_{dp\text{-}ref}$, is obtained by a washout filter. $i_{dp\text{-}ref}$ is obtained by:

$$i_{dp-ref} = \omega \times G \times \frac{sT_w}{1+sT_w} \tag{2.5}$$

G and T_w are the washout filter's gain and time constant, respectively. T_w is set to 10 sec in this paper.
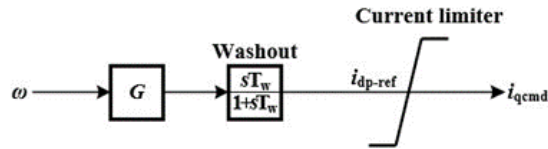
Fig. 2.2: Block diagram of Reactive POD controller mode of FCS in DC-AC converter.

B. Active POD scheme in the Boost Converter Controller

Fig. 2.3 shows the typical characteristics curve of a 250 kW PV panel simulated in PSCAD.
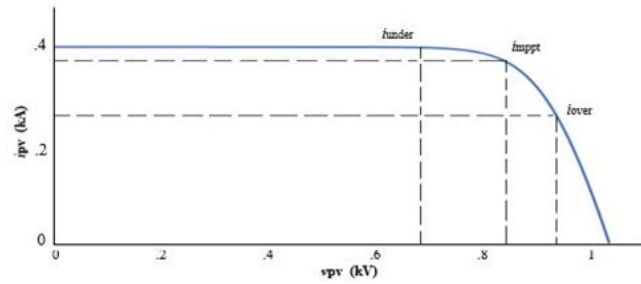
(a)
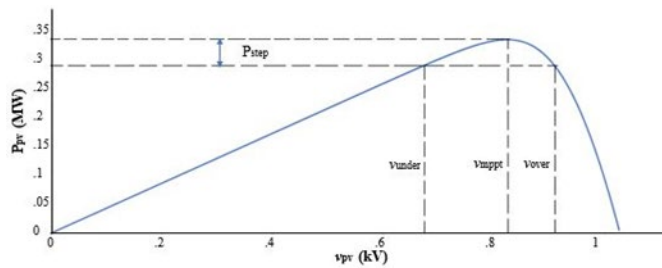
(b)

Fig. 2.3: Typical PV characteristics curves. (a) current, and (b) power versus PV voltage curve.

From the characteristic curves, it is prominent that if the PV plant can operate under or overvoltage conditions, it should have extra headroom to control the oscillation measured at its terminal. It can be observed that the slope between v_{mppt} and v_{over} is much steeper than that of v_{mppt} and v_{under}. Hence it can be concluded that the performance of the MPPT can be made more dynamic if it is operated in v_{over} condition. Though the overvoltage operation might harm the dc-link capacitor and the power electronic switches, proper knowledge of dc-link capacitor and future IGBT switches with a slightly higher voltage rating positively impact the overall system performance.

As shown in Fig. 2.4, an additional control function $\varDelta V$ was added to modulate the MPPT. From the lookup table of the characteristics curve, we can find the v_{over} at which the PV panel will

provide necessary headroom for residual real power to dampen the inter-area oscillation. The value of ΔV can be found by:

$$\Delta V = K_{dv} \cdot v_{pv} \tag{2.6}$$

where K_{dv} is a constant and can be determined from the characteristics curve.

The active POD works with the principle of operating the PV panel with a slightly higher voltage and manipulating the reference power P_{ref} during the oscillation. In the pre-fault condition, the reference power for the PV panel is $P_{ref} = P_{mppt}$ and $\Delta V = 0$.
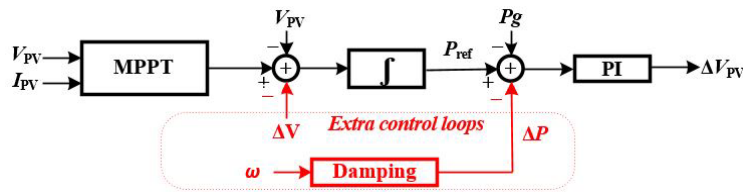
Fig. 2.4: Block diagram of Active POD controller mode of FCS in DC-DC converter.

Fig. 2.4 demonstrates the block diagram of the proposed active POD controller. The active POD gets activated whenever an oscillation is detected by the measuring unit placed on its terminal or any measuring units nearby to the PV plant. Increasing PV panel voltage within its voltage limits will provide an extra margin ΔP to dampen the oscillation. The angular speed of the nearest synchronous generator, ω, is taken as the input for the damping control loop to achieve this oscillation damping. Then, ω is filtered by a washout filter. The residual real power function feedback for the damping control, ΔP is obtained by a washout filter. ΔP is obtained by:

$$\Delta P = \omega \times G_1 \times \frac{sT_{w1}}{1+sT_{w1}} \tag{2.7}$$

G_1 and T_{w1} are the washout filter's gain and time constant, respectively. T_{w1} is set to 10 sec in this paper. ΔV_{PV} is meant to regulate the PV panel voltage according to the modes at which the PV plant is working.

When the oscillation is damped correctly for a certain time, the value of ΔV and ΔP again comes to zero. Hence the recovery mode can be adjusted with a very slow decrease in voltage to its rated v_{mppt} voltage. The real power will be automatically adjusted with the change of voltage in the PV panel terminal.

C. Active and reactive POD controller scheme or Dual POD controller scheme

In this controller, the reactive power capacity of the PV plant has also been utilized along with the active POD. The inverter will operate on the P priority, and the rest of the current limit will be used for the reactive power damping.

2.3 Inter-area oscillation damping using PV plant.

A two-area system consisting of two 2 GW hydro generators has been developed in PSCAD to investigate the efficacy of the PV plants in inter-area low-frequency oscillation. A 100 MW large-scale PV has been installed in area 2, as shown in Fig. 2.5. The objective is to examine the effectiveness of the damping controller proposed in the paper during the inter-area low-frequency oscillation. There are no power system stabilizers (PSSs) connected to the hydro generators, while the PV plant is supposed to serve like the PSS.
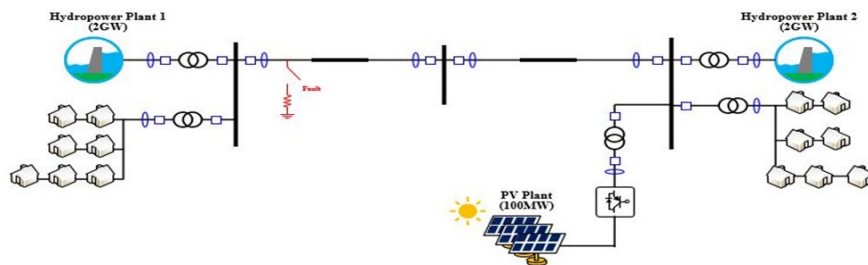
Fig. 2.5: Two-area system with the PV plant in area 2 and fault in area 1.

TABLE 2.1

THE TEST SYSTEM

No.	Model components	Comments
1	**PV Plant (Area 2)**	Made from the PSCAD library *-100MW, .69 kV*
2	**Synchronous Generator 1 & 2**	Made from the PSCAD library *-2GW, 230 kV*
4	**Loads**	- 1000 MW & 400 MVAR for each area
5	**Fault**	A three phase to ground fault of 0.2 s has been made at 10 s.

POD has three control modes. Each control mode will be observed separately with the same fault in the system. A three-phase to-ground fault for 0.2 s is simulated in area 1. We will try to damp out the oscillation from a PV plant connected in area 2.

Reactive power cannot be transmitted over long distances as it operates locally. An efficient way to damp power oscillation with reactive POD can be reasonable for local distribution networks. However, locating the PV plant in the middle of the transmission line might not be feasible. Furthermore, presumably, it's possible to locate the PV plant; the reactive power needed to damp out the power oscillation is still in contention. Hence, damping out the power oscillations with other schemes like active POD and dual POD can be a better way to get power oscillation damping.

Figs. 2.6(a) and (b) depict the active power output of areas 1 and 2, respectively. The time scale is not as detailed as the previous case study because this study's objective is to get faster damping control schemes with the same penetration level for all the POD modes. From Fig. 2.6, it can be concluded that all the damping controllers are working efficiently to damp the inter-area oscillation. The reactive power damping controller is the slowest among the POD schemes. Active

POD damps the power oscillation faster than reactive POD. However, the dual POD, a combination of active and reactive POD, dampens the oscillation much faster than the previous two PODs. Hence, we conclude that the PV plant can damp the oscillation efficiently and faster than any other controllers cited in this paper.

Figs. 2.6(c) and (d) depict the reactive power output of generators 1 and 2, respectively. The reactive power output among the generators is the highest for the reactive POD. This is because the reactive power is responsible for this damping scheme. For the other two schemes, the oscillation settles down after some time. We observed that the active and dual POD oscillations are also mitigating faster than the reactive POD scheme.
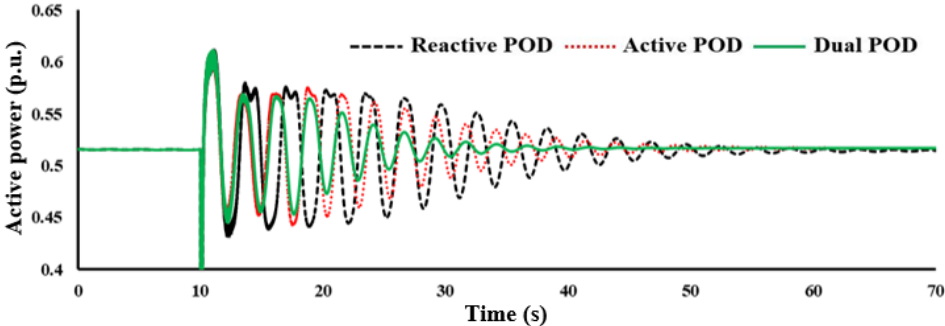
(a)
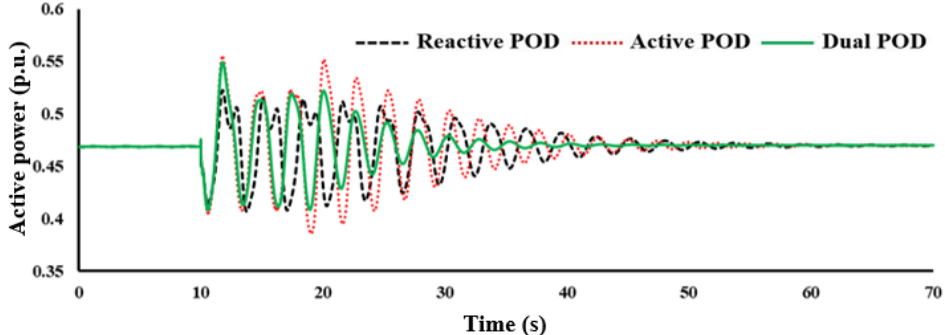
(b)
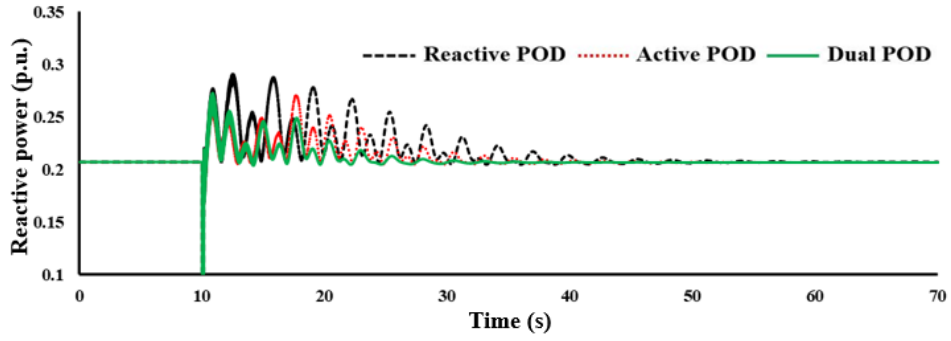
(c)
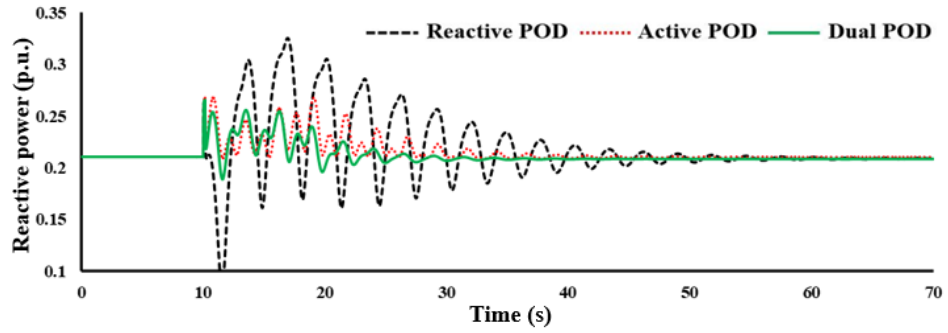
(d)
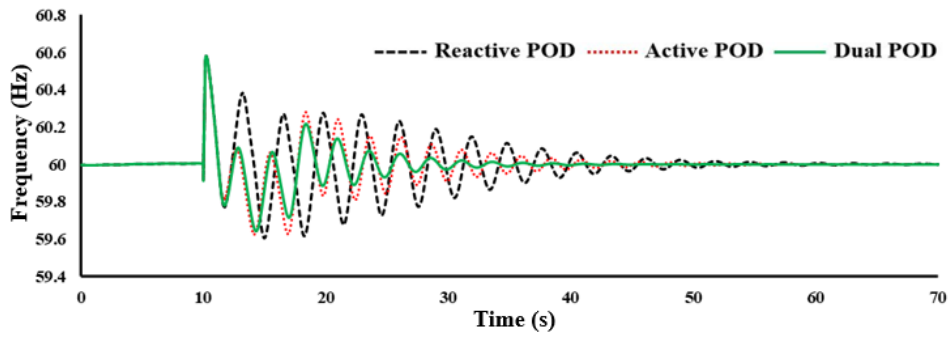
(e)
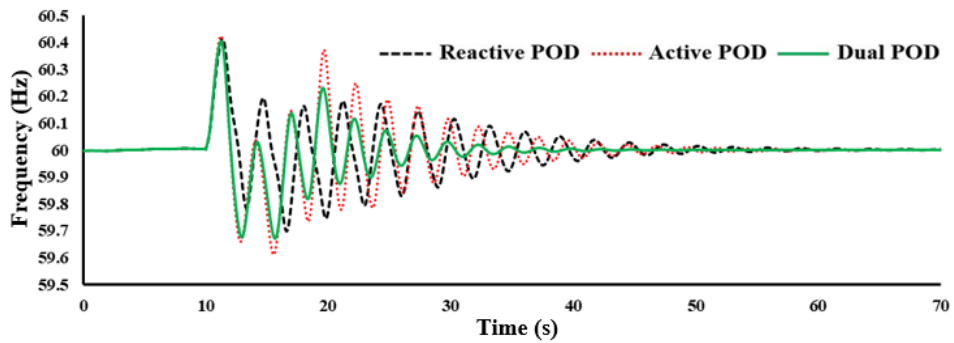
(f)

Fig. 2.6: Hydro Generators output for the three POD schemes during fault and post fault condition. (a) the active power output of Generator 1 in area 1. (b) the active power output of Generator 2 in area 2. (c) the reactive power output of Generator 1. (d) the reactive power output of Generator 2 (e) frequency output of Generator 1. (f) frequency output of Generator 2.

Figs. 2.6(e) and (f) show the frequency in bus 1 and 2 during the fault and post-fault condition, respectively. Compared to reactive POD and Active POD controllers, the frequency is settling down for dual POD.

The active power of the plant is depicted in Fig. 2.7(a). The fluctuation of active power is comparatively less for the reactive POD.
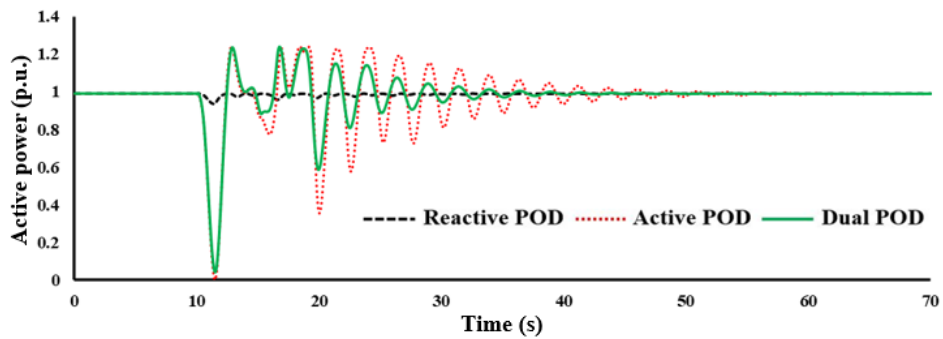
(a)
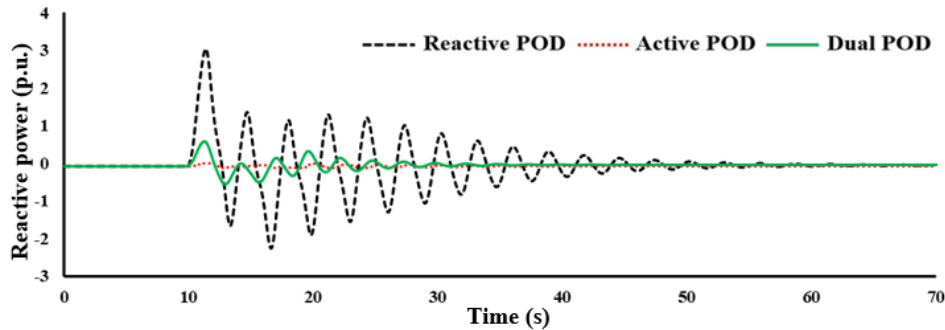
(b)
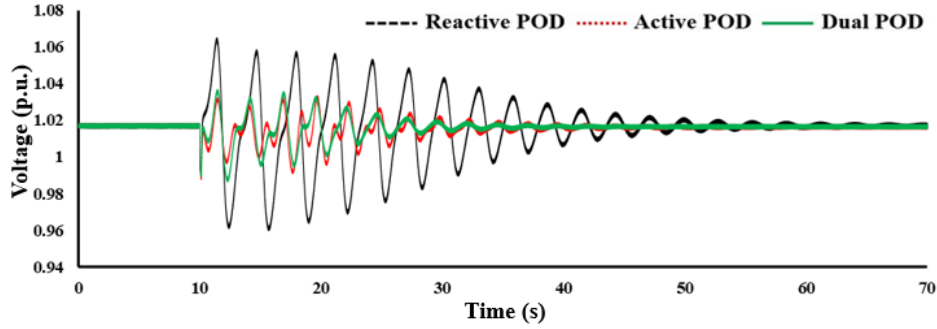
(c)

Fig. 2.7: PV plant output at the POI during fault and post fault condition. (a) active power output. (b) reactive power output. (c) voltage output.

As the active power has damped the power oscillation for the rest of the two cases, the normal range deviation is highest for these two cases. The active power gets lower after the fault. Hence, the reactive power of the PV plant can be utilized during this time.

Fig. 2.7(b) shows that the reactive power needed for damping the inter-area low-frequency oscillation is beyond the present PV plant capacity. Eliminating the current limiter from the reactive POD resulted in the waveform shown in Fig. 2.7(b). The inverter's current capacity needs to be increased by 200% more than its rated capacity (i.e., this is an expensive proposition to modify the PV inverter). For the other controllers (Fig. 2.7a and Fig. 2.7c), the reactive power output is within its limit and maintains the inverter's current constraint. The voltage fluctuation is also the most for the reactive POD shown in Fig. 2.7(c). The rest of the control schemes maintain the voltage within the permissible limit with slight fluctuations.

2.4 Conclusion

In conclusion, Chapter 2 has presented a thorough comparative study assessing the effectiveness of various Power Oscillation Damping (POD) schemes within utility-scale photovoltaic (PV) plants. Notably, a novel scheme named dual POD, combining active and

reactive POD, has been introduced and proven highly effective in dampening inter-area low-frequency oscillations. The dual POD scheme strategically modulates the PV panel voltage in the boost converter to create an active power margin. Subsequently, the remaining inverter capacity is harnessed to support reactive power through the Grid-Side Converter (GSC). The extensive simulations conducted in two distinct areas affirm the efficiency of the dual POD scheme, demonstrating its ability to dampen inter-area oscillations at a notably faster rate compared to conventional methods employed in PV plants.

Looking forward, Chapter 6 will extend the investigation by subjecting the signals generated from the simulation to further testing. This meticulous analysis aims to identify the exponential sinusoids present in the output, facilitating a comprehensive comparison with other schemes described or proposed in the subsequent chapters. This additional step in Chapter 6 is poised to provide a nuanced understanding of the dual POD scheme's performance, validating its efficacy against alternative approaches in the dynamic landscape of power system oscillation damping.

Chapter 3
Power Oscillation Damping with WPP

Over the past few years, wind power has proliferated and is gradually becoming a ubiquitous form of renewable energy. According to the International Energy Agency (IEA), in 2021, wind electricity generation increased by 273 TWh (up 17%). This was 55% higher growth than in 2020 and was the highest among all renewable power technologies. Such rapid development was possible thanks to an unprecedented increase in wind capacity additions, which reached 113 GW in 2020, compared with just 59 GW in 2019 [48]. The onshore US wind industry installed 13,413 megawatts (MW) of new wind capacity in 2021, bringing the cumulative total to 135,886 MW. This is the second-highest wind capacity installed in one year (behind 2020) and represents $20 billion of investment. Wind provides more than 9% of electricity nationwide, over 50% in Iowa and South Dakota, and over 30% in Kansas, Oklahoma, and North Dakota [49].

However, integrating renewable energy sources into the utility grids reduces the inertia in the system. Due to the replacement of conventional synchronous generators with these RES, the issues in stability and reliability have become significant.

3.1 Contribution of WPP in auxiliary services

Unlike hydro, nuclear, or thermal [17] power plants, the operation of RESs is primarily based on power electronic devices. Due to these problems, the TSOs are already proposing some ancillary services for the WPPs in the recent grid codes. According to these codes, WPPs must comply with requirements including voltage sag ride-through capabilities [18], frequency regulation [19], and active and reactive power regulation [20]. In the future, more WPP

contributions will be required by the TSOs. The capability to dampen power system oscillations plays a significant role in ensuring grid reliability.

3.1.1 Use of Active Power modulation of WPP in auxiliary services

The direct and logical approach to damp power system oscillation is regulating active power as the oscillations are produced due to the differences between the two areas. Active power can be regulated using mechanical systems [50]−[51] or by using power converters [52],[46]. Controlling the pitch angle with PID and fuzzy logic controllers has been cited in [50] and [51]. However, mechanical regulation is well known to be slower than the control of electrical variables [20]. Hence, active power regulation utilizing fast-acting power converters is much faster and more efficient. As in frequency control, the first step in an additional POD controller for WPP is to copy the PSS from the synchronous generators [52]. Simple tuning to adjust PSS parameters provided promising results in case [53]. The voltage of the POI of the WPP is selected as the input, and a variation of power reference is the controller's output. Some researchers even proposed a reduced version of PSS, which works effectively for inter-area oscillations [51].

3.1.2 Use of Reactive Power modulation of WPP in auxiliary services

As in active power regulation cases, conventional PSS schemes have also been utilized in the reactive power loop. The conventional PSS scheme has been evaluated by inputs such as local and remote signals and voltage variation as output [20]. A clear trend towards using active power control to improve power stability is observed in WPPs. Nevertheless, the effect of reactive power regulation could be important for the power systems due to their ability to change the power flow between the buses.

3.2 WPP System Model

The configuration of a wind turbine system model used in this paper is depicted in Fig. 3.1. The wind power plant model consists of a wind turbine, PMSG, a machine side converter (MSC), DC circuit, Grid Side Converter (GSC).

The power extracted by the turbine blade is given as:

$$P_w = \frac{1}{2}.\rho.\pi.R^2.V_w^3.c_p(\lambda,\beta) \tag{3.1}$$

where: R_w is the blade radius of the wind turbine, β is the blade pitch angle in degree, λ is the tip speed ratio defined by:

$$\lambda = \frac{w_t.R}{V_w} \tag{3.2}$$

where:

w_t is the mechanical rotational speed of the turbine in rad/s, and c_p is expressed as a non-linear function of the tip speed ratio and the pitch angle as

$$c_p = 0.645\left\{0.00912\lambda + \frac{-5-0.4(2.5+\beta)+116\lambda_i}{e^{21\lambda_i}}\right\} \tag{3.3}$$

where:

$$\lambda_i = \frac{1}{\lambda+0.08(2.5+\beta)} - \frac{0.035}{1+(2.5+\beta)^3} \tag{3.4}$$

The maximum output power of the wind turbine is obtained by tracking the rotor speed to the optimum point λ_{opt} that yields the maximum aerodynamic efficiency. Therefore, the optimum wind turbine speed is given as:

$$w_{t,opt} = \frac{\lambda_{opt}.V_w}{R} \tag{3.5}$$

Therefore, the maximum power is obtained as:

$$P_{MPPT} = \frac{1}{2} . \rho . \pi . R^2 . \left(\frac{w_{t,opt} . R}{\lambda_{opt}} \right)^3 . c_{p,max} \tag{3.6}$$

which can be rewritten as:

$$P_{MPPT} = K_g w_g{}^3 \tag{3.7}$$

where K_g is the coefficient of the MPPT curve.

The MSC converter controls the generator rotor speed to achieve the maximum power operating point. The maximum power operating point acts as a reference power signal for the MSC converter, which is used to regulate the power generated by the PMSG of the wind turbine to produce reference signals that feed into the control loops.

On the other hand, the GSC regulates the DC link voltage, V_{dc}, and the reactive power, Q_g, at the GSC terminal continuously. The GSC controller generates an active current reference, i_{Pcmd1}, to achieve the former using a proportional-integral controller and a current limiter. For the latter, the controller generates a reactive current reference, i_{Qcmd1}, through a PI controller and a current limiter. Current limiters were introduced to keep currents within the inverter's capacity to a minimum. The GSC is simplified as a current source in this work. As shown in Fig. 3.1, the current references are changed into three-phase references and fed into the current source.
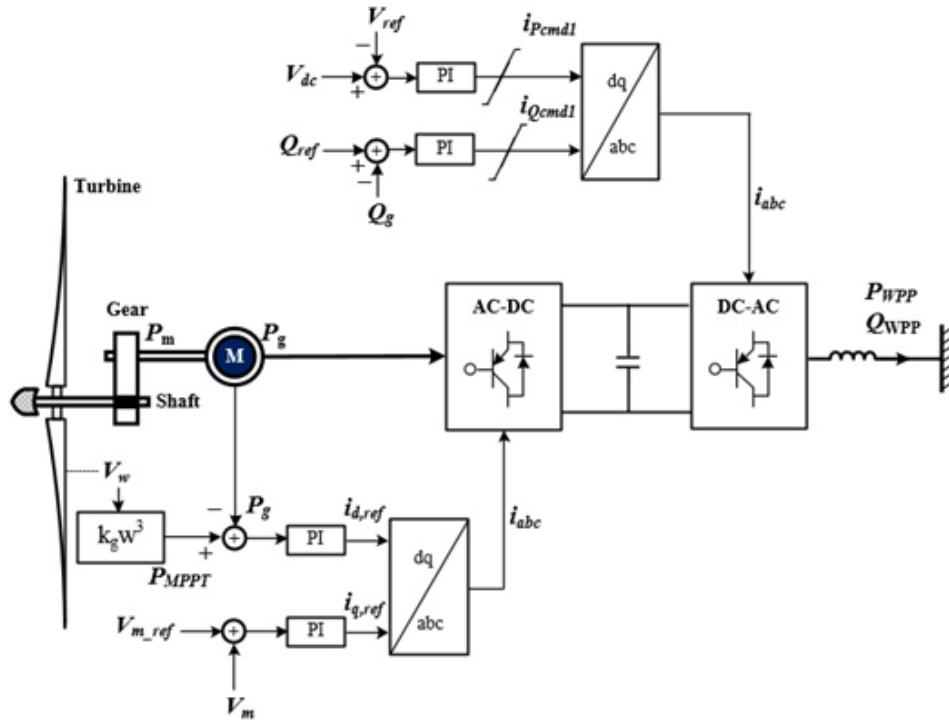
Fig. 3.1: Configuration of a WPP system model.

3.2.1 The proposed Control Scheme of the WPP plant

The proposed control schemes for Type 4 WPP is described in this section.

A. Reactive POD scheme in the Inverter Controller

Fig. 3.2 shows the reactive POD used in the proposed control scheme. The speed of the generator has been taken as feedback for the Reactive POD.
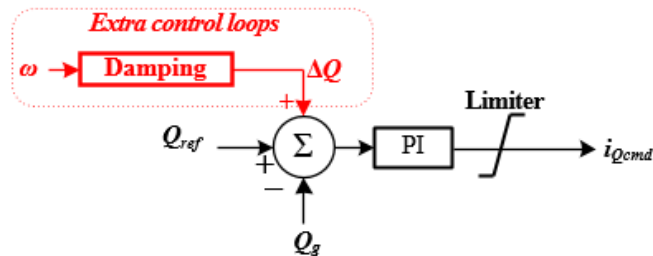
Fig. 3.2: Block diagram of Reactive POD controller mode in DC-AC converter.

The feedback associated with the speed might have involved delay due to the inertia of

these huge synchronous machines. However, those delays are not considered in this paper as we will use the feedback from the nearest synchronous generator.

The signal, ω, is fed to the washout filter to remove the steady-state component. The reactive power reference for the damping control, ΔQ, is obtained by:

$$\Delta Q = \omega \times G \times \frac{sT_w}{1+sT_w} \tag{3.8}$$

G and T_w are the washout filter's gain and time constant, respectively. T_w is set to 10 sec in this paper.

B. Active POD scheme in the AC-DC Converter Controller

Fig. 3.3 shows the active POD scheme added in the AC-DC controller. The bus angle, δ, from the POI has been taken as feedback for this loop, as active power and δ are closely related.

This damping scheme utilizes the extra power remaining kinetic energy in the wind turbine. ΔP is obtained by:

$$\Delta P = \delta \times G_1 \times \frac{sT_{w1}}{1+sT_{w1}} \tag{3.9}$$

G_1 and T_{w1} are the washout filter's gain and time constant, respectively. T_{w1} is set to 10 sec in this paper.

C. Active and reactive POD controller scheme or Dual POD controller scheme

In this controller, the full capacity of the WPP has been utilized. The WPP will be working on active power priority, and the rest of the inverter capacity has been utilized for reactive power damping. For the dual POD, the feedback signal is the speed of the nearest connected synchronous generator for the reactive POD, and the bus angle (δ) has been taken for the active POD.
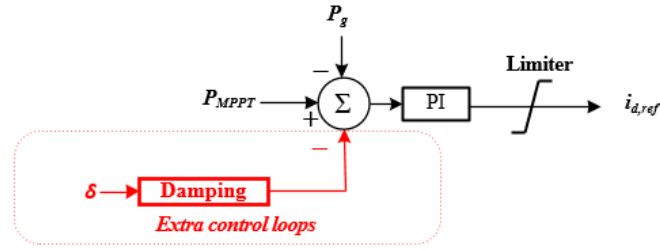
Fig. 3.3: Block diagram of Active POD controller mode of in AC-DC converter.

3.3 Inter-area oscillation damping using WPP.

This chapter investigates the efficacy of damping of interarea-oscillation with a utility-scale WPP in a two-area system. A two-area system with two 2 GW hydro generators has been taken as the test system. As shown in Fig. 3.4, a 170 MW WPP, with different power oscillation damping control loops, has been connected to area 2. No PSSs are connected at each of the hydro generators. A three-phase to-ground fault has been made at area 1 for 0.15s. And our aim is to damp the power oscillation after the fault clearance with the controllers in WPP situated in area 2. Our aim is also to examine and compare the rapidness of each POD scheme mentioned above to get the most suitable control scheme to dampen oscillation with Utility scale WPPs.

TABLE 3.1

THE TEST SYSTEM

No.	Model components	Comments
1	WPP (Area 2)	Made from the PSCAD library *-170MW, .69 kV*
2	Synchronous Generator 1 & 2	Made from the PSCAD library *-2GW, 230 kV*
4	Loads	- 1000 MW & 400 MVAR for each area
5	Fault	A three phase to ground fault of 0.15 sec has been made at 10 sec.
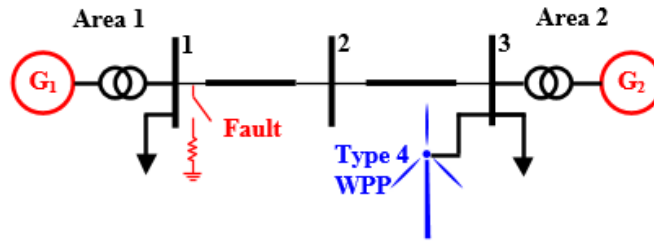
Fig. 3.4: Two-area system with the WPP plant in area 2 and fault in area 1.

The plots on Fig. 3.5 and Fig. 3.6 are per-unitized with the rated capacity of the plants and the rated voltage. The WPP is not working to its full capacity and providing only 100MW to the grid. The rest of the head room has been utilized for the Active POD.

From Figs. 3.5(a) and (b), the reactive POD takes the longest time to dampen the oscillation. The reactive POD does not contain any current limiter in it as the WPP cannot dampen out the oscillation in its present capacity. It has also been observed that the dual-power POD is slightly faster than the Active POD. Hence, it can be concluded that using the whole capacity damps out the oscillation faster than aiming for any one power oscillation damping scheme. Thus, the proposed dual POD can damp the oscillation efficiently faster than the other regular controller cited in this paper.

Figs. 3.5(c) and (d), depict the reactive power output at the two generators in the two areas. The reactive power fluctuates the most in the application of reactive POD. This is due to the abundance of reactive power supply from the WPP. It varies the most in area 2 as the WPP is connected to area 2. The variation of reactive power for active power damping is not that significant. The reactive power output in the case of dual power damping is between reactive POD and active POD as the dual POD utilizes both active and reactive power modulation to dampen the power oscillation.

(a)

(b)

(c)

(d)

(e)

(f)

41
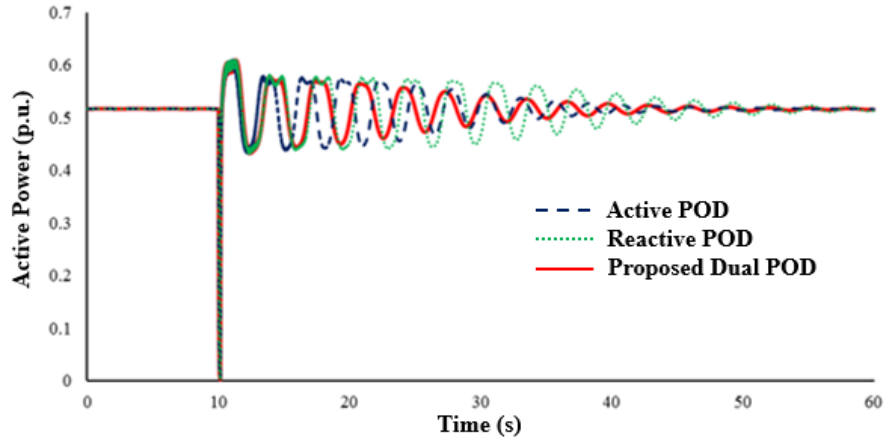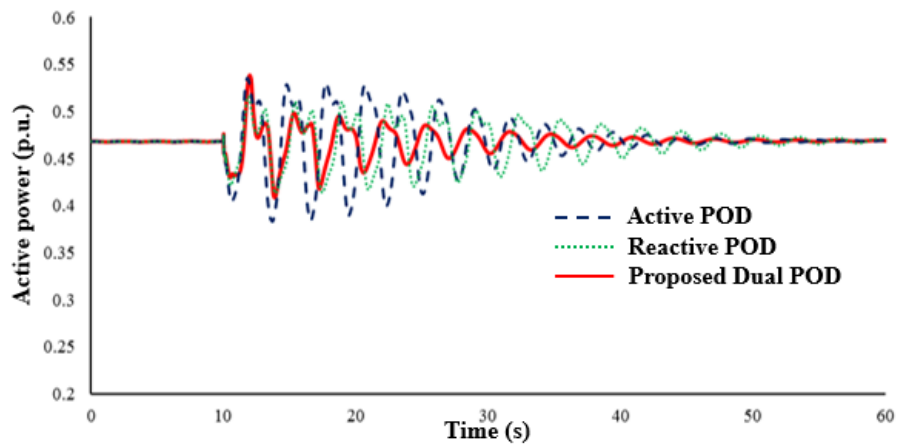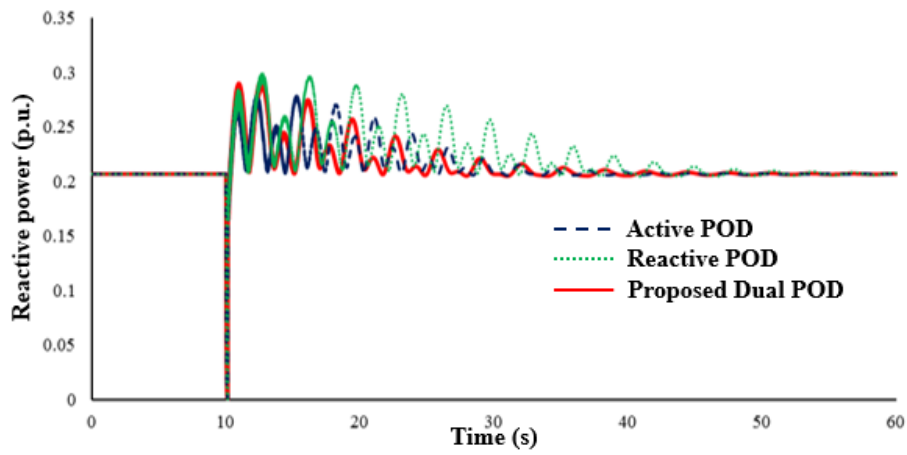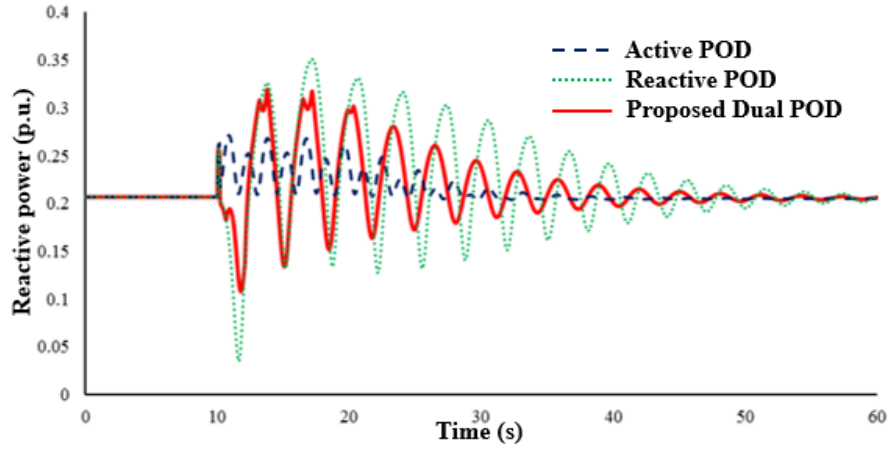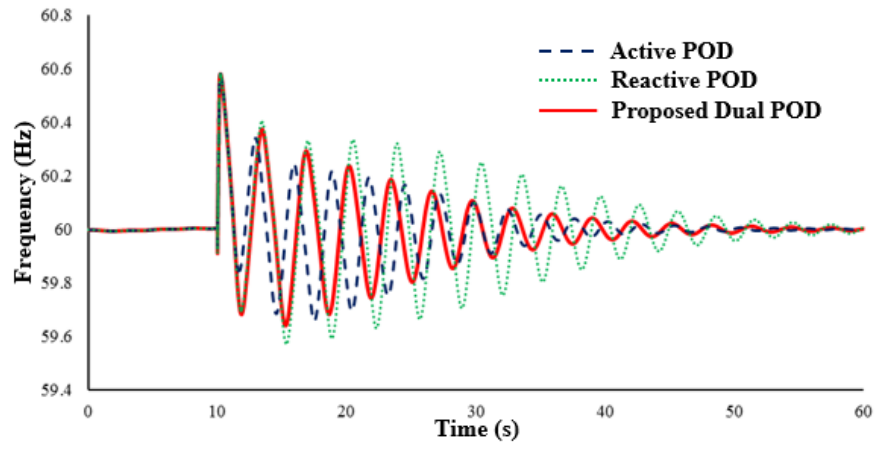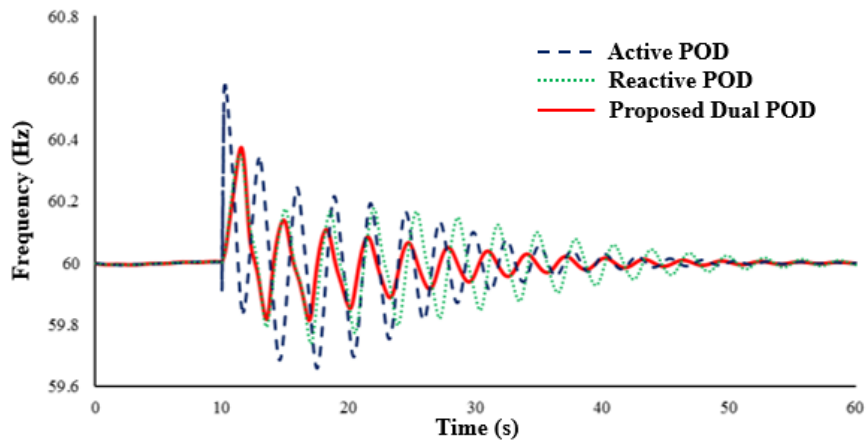
Fig. 3.5: Hydro Generators output for the three POD schemes during fault and post fault condition. (a) active power output of Generator 1 in area 1. (b) active power output of Generator 2 in area 2. (c) reactive power output of Generator 1. (d) reactive power output of Generator 2 (e) frequency output of Generator 1. (f) frequency output of Generator 2.

Figs. 3.5(e) and (f) show the generators' frequency output in the two areas. In both the cases, the frequency is stabilized faster in dual POD.

Fig. 3.6(a) shows the WPP's active power output during and after the fault clearance. As the operating voltage is the same for all the cases, the power is limited by utilizing the current limiters in the control loops. In reactive POD, the variation of active power is insignificant. The active power fluctuates within its limit for active and dual POD schemes. The performance of the dual POD scheme seems to be a bit faster than the active POD in this case as well.

Fig. 3.6(b), depicts the reactive power output of the different POD schemes used in the WPP. The reactive power output for the reactive POD is not limited, as damping the oscillation with its present capacity was impossible. Though, using reactive power modulation in dual POD within its current limitation has shown us promising results to dampen the power oscillation.

Due to the input of reactive power insertion on each POD scheme, the voltage at the POI might vary within its limit. In Fig. 3.6(c), it has been observed that the voltage fluctuates the most for the reactive POD. For dual POD, it is also fluctuating, but it is less reactive POD. There is no significant change in voltage for the active POD.
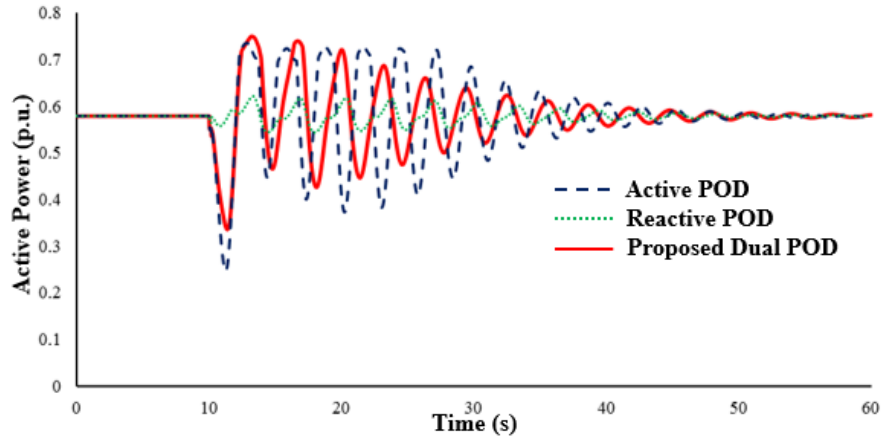
(a)
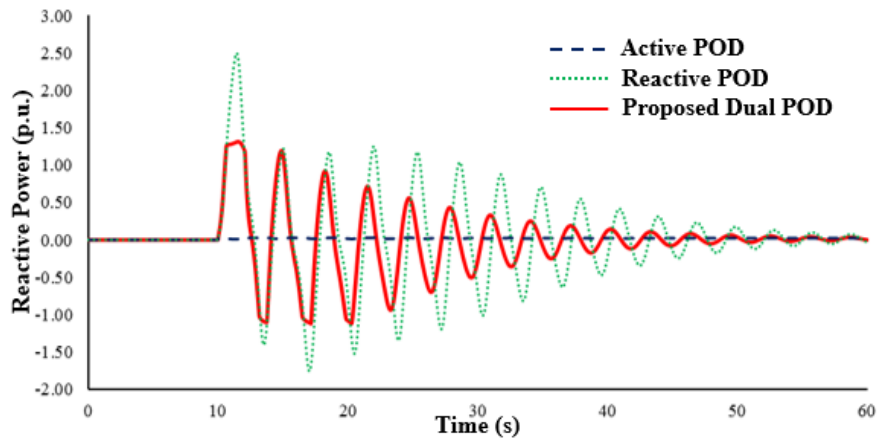
(b)
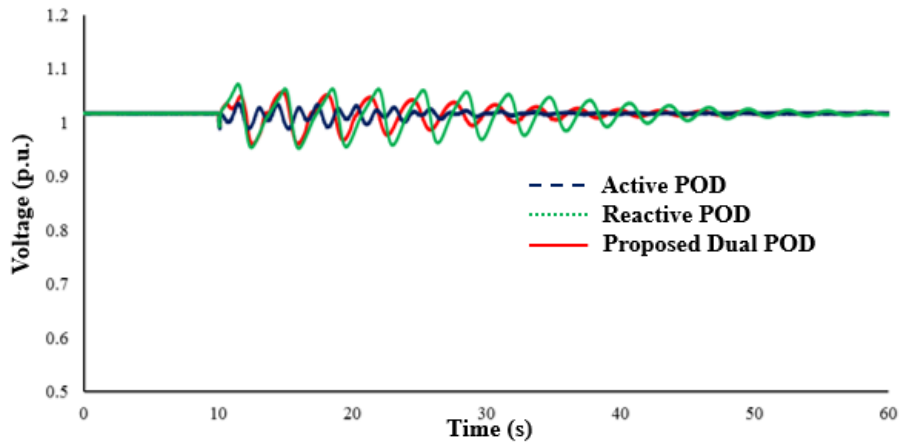
(c)

Fig. 3.6: WPP output at the POI during fault and post fault condition. (a) active power output. (b) reactive power output. (c) voltage output.

3.4 Conclusion

In conclusion, Chapter 3 has delved into the exploration of leveraging a utility-scale Wind Power Plant (WPP) to mitigate inter-area low-frequency oscillations through the application of various Power Oscillation Damping (POD) schemes. The simulation scenario involved inducing a fault in area 1, while the WPP connected to area 2 aimed to provide damping using distinct POD strategies. An important observation emerged, emphasizing the critical role of the WPP's position in achieving effective damping, particularly in scenarios where reactive power operates locally.

The capacity of the reactive POD scheme was deemed crucial, requiring an unlimited capacity for optimal performance. Comparatively, active power damping exhibited a faster dampening of oscillations than the reactive POD scheme. However, the novel dual POD scheme demonstrated a slightly quicker reduction in oscillations compared to the active POD scheme. This insightful comparative study underscores the efficacy of the dual POD scheme, positioning it as a promising approach for efficient oscillation damping in the context of utility-scale WPPs.

Looking ahead, Chapter 6 will further expand upon these findings by conducting additional analysis using Prony, facilitating a more comprehensive comparison with other schemes and diverse renewable energy sources. This enhanced analysis will contribute to a deeper understanding of the dual POD scheme's performance and its comparative advantage in the dynamic landscape of power system oscillation damping.

Chapter 4
Power Oscillation Damping with PV & WPP

PV plants and WPPs in the same vicinity optimize the utilization of available renewable resources [55], provided that solar and wind resources are abundant in the same region. The cogeneration of PV and wind power (WP) has the following advantages; i) availability of wind and solar is complementary to each other, which increases the overall efficiency [56], ii) optimized land use leading to minimized capital investment [57], iii) the moment of inertia present in the mechanical system of WPP prioritizes the PV and WPP cogeneration over PV plant acting alone [58], iv) availability of two energy sources improve the reliability [59]. Despite these advantages, PV-WPP cogeneration is not very common in utility-scale applications. A single-phase cogeneration has been cited in [60]; small-scale laboratory-based cogeneration has been tested in [61]. Several off-grid applications of PV-WP cogeneration are found in [62]–[63]. Reference [64], focused on the controller complexities and the instabilities caused by these complexities. Nevertheless, proper knowledge of control schemes might lead to certain advantages for the grid, especially when generated on a utility scale [65].

This chapter offers a coordination scheme of dual PODs in utility-scale PV and WPPs, depending on the time of the day. This coordinated scheme entails the mode of operation for both IBRs. The scheme includes two separate strategies i) during the daytime, the dual POD of the PV plant will operate, whereas the WPP will use its reactive control loop only ii) similarly, at night, the dual POD of the WPP will operate, whereas only the reactive power modulation used in the PV plant. In both PV and WPP, an active power damping function without any power curtailment and a reactive power damping function modulating the reactive current (I_Q)

on the voltage control loop have been included. This chapter uses the nearest synchronous generator's local bus angle and speed as feedback for each of these loops. Thus, the proposed coordinated scheme enables the IBRs to support the grid's voltage stability during the faults and provide fast system stabilization once the fault is cleared.

4.1 Proposed control scheme for IBRs

A. PV System Model
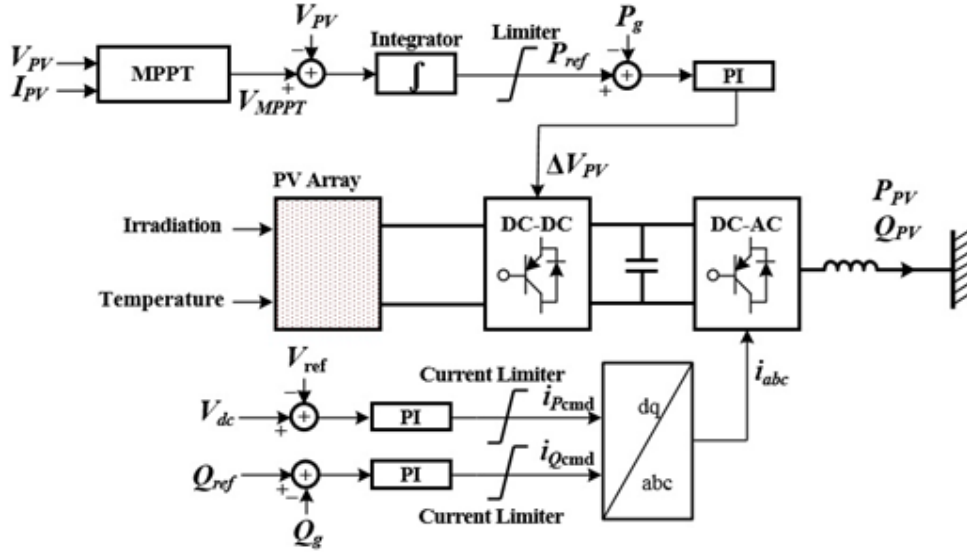
Fig. 4.1: Configuration of a PV system model.

Fig. 4.1 depicts the configuration of the PV system model utilized in this paper. PV generator, boost converter, DC circuit, and grid-side converter (GSC) are all included in the PV plant model. The MPPT mode maintains the maximum output power from the PV panels. The MPPT determines the voltage reference, V_{MPPT}, at the array based on the PV array's line current, I_{PV}, and internal voltage, V_{PV}. Based on the error between V_{MPPT} and V_{PV}, an integral controller calculates the MPPT power reference, P_{ref}. After the integrator, a limiter was applied to keep the P_{ref} within its capacity. The controller then initiates switching signals for the boost converter,

allowing the boost converter to extract the maximum power from the source.

On the other hand, the GSC regulates the DC link voltage, V_{dc}, and reactive power, Q_g, at the GSC terminal continuously. The GSC controller achieves the former by employing a PI controller and a current limiter by generating an active current reference, i_{Pcmd}. For the latter, the controller uses a PI controller and a current limiter to generate a reactive current reference, i_{Qcmd}. Current limiters keep the IGBT currents within the inverter's capacity to their allowable range. The GSC is a simplified current source in this work. As indicated in Fig. 4.1, the current references are changed into three-phase references and fed into the current source.

B. WPP System Model
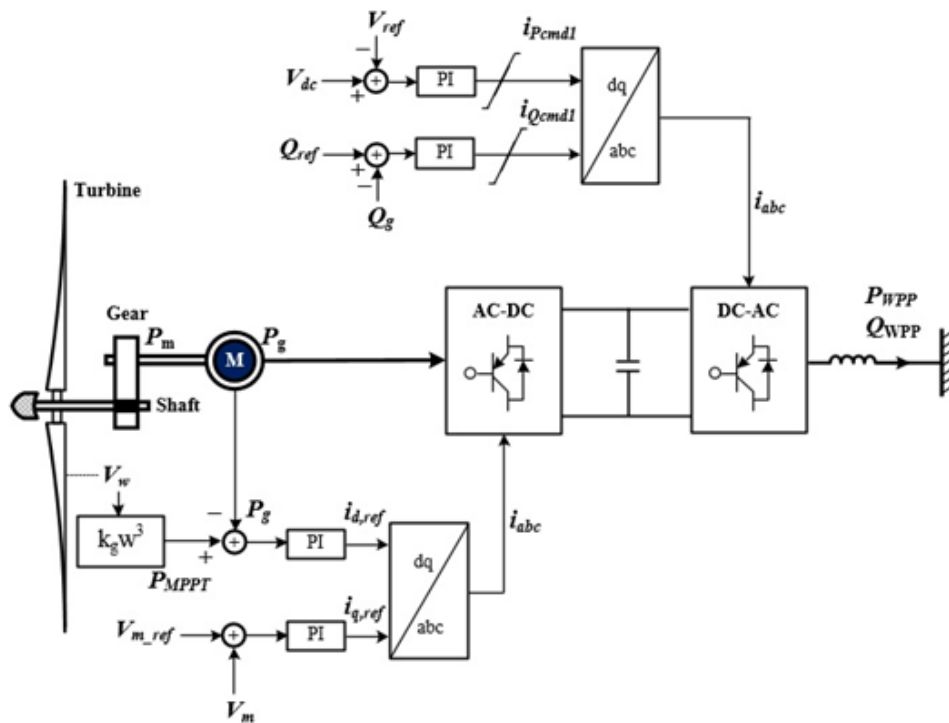
Fig. 4.2: Configuration of a WPP system model.

Fig. 4.2 shows the configuration of a wind turbine system model utilized in this paper. The wind power plant model comprises a wind turbine, PMSG, machine side converter (MSC), DC circuit, and GSC.

The power extracted by the turbine blade is given as:

$$P_w = \frac{1}{2}.\rho.\pi.R^2.V_w^3.c_p(\lambda,\beta) \qquad (4.1)$$

where: R is the blade radius of the wind turbine, β is the blade pitch angle in degree, λ is the tip speed ratio defined by:

$$\lambda = \frac{w_t.R}{V_w} \qquad (4.2)$$

where:

w_t is the mechanical rotational speed of the turbine in rad/s. c_p is expressed as a non-linear function of the tip speed ratio and the pitch angle as:

$$c_p = 0.645\left\{0.00912\lambda + \frac{-5-0.4(2.5+\beta)+116\lambda_i}{e^{21\lambda_i}}\right\} \qquad (4.3)$$

where:

$$\lambda_i = \frac{1}{\lambda+0.08(2.5+\beta)} - \frac{0.035}{1+(2.5+\beta)^3} \qquad (4.4)$$

The maximum output power of the wind turbine is obtained by monitoring the rotor speed to the optimum point, λ_{opt}, which provides the highest aerodynamic efficiency. Therefore, the optimum wind turbine speed is given as:

$$w_{t,opt} = \frac{\lambda_{opt}.V_w}{R} \qquad (4.5)$$

Therefore, the maximum power is obtained as:

$$P_{MPPT} = \frac{1}{2}.\rho.\pi.R^2.\left(\frac{w_{t,opt}.R}{\lambda_{opt}}\right)^3.c_{p,max} \qquad (4.6)$$

which can be rewritten as:

$$P_{MPPT} = K_g w_g^3 \qquad (4.7)$$

where K_g is the coefficient of the MPPT curve.

The MSC converter modulates the generator's rotor speed to reach the maximum output

operating point. The MSC converter uses a maximum power operating point as a reference power signal. It is utilized to generate the reference signal delivered to the control loop by regulating the power generated by the wind turbine's PMSG.

On the other hand, GSC maintains the DC link voltage, V_{dc}, and controls the reactive output power, Q_g, at the GSC terminal in real-time. The GSC controller generates the active current reference, i_{Pcmd1}, with the help of a PI controller and a current limiter. In the latter scenario, the controller generates the reactive current reference, i_{Qcmd1}, via the PI controller and current limiter. The GSC includes current limiters to keep the current within the inverter's capacity. As shown in Figure 2, the GSC is modeled as the current source in this work. The current reference is transformed into a three-phase reference and delivered to the current source, as shown in Fig. 4.2.

C. Reactive POD scheme in the Inverter Controller
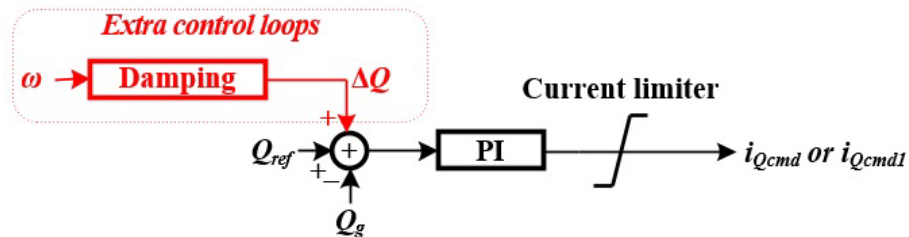
Fig. 4.3: Block diagram of Reactive POD controller mode in DC-AC converter.

The reactive power output of the Reactive POD scheme of the PV plant and WPP provides damping for the low-frequency electromechanical oscillations. In [25],[29], the generator's speed was used as feedback for the Reactive POD. Due to the inertia of these massive synchronous machines, the feedback linked with speed may have included a delay. Furthermore, the communication delay discussed in [30]–[31] could substantially impact the PODs' performance. However, those delays are not considered in this paper as the feedback from the nearest synchronous generator has been used in this paper. As a result, the plant's terminal voltage controls the reactive power injection during and after a malfunction.

49

The signal of ω, is fed to the washout filter to remove the steady-state component. The reactive power reference, for the damping control, ΔQ, is obtained by:

$$\Delta Q = \omega \times G \times \frac{sT_w}{1+sT_w} \tag{4.8}$$

where G and T_w are the washout filter's gain and time constant, respectively. T_w is set to 10 sec in this paper.
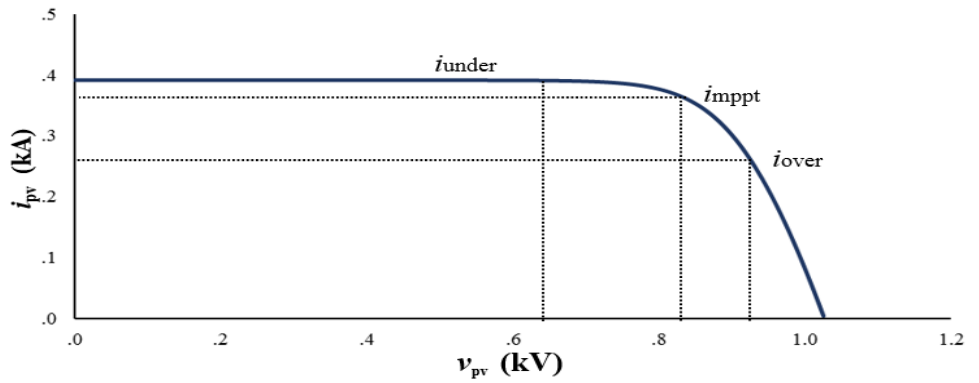
(a)
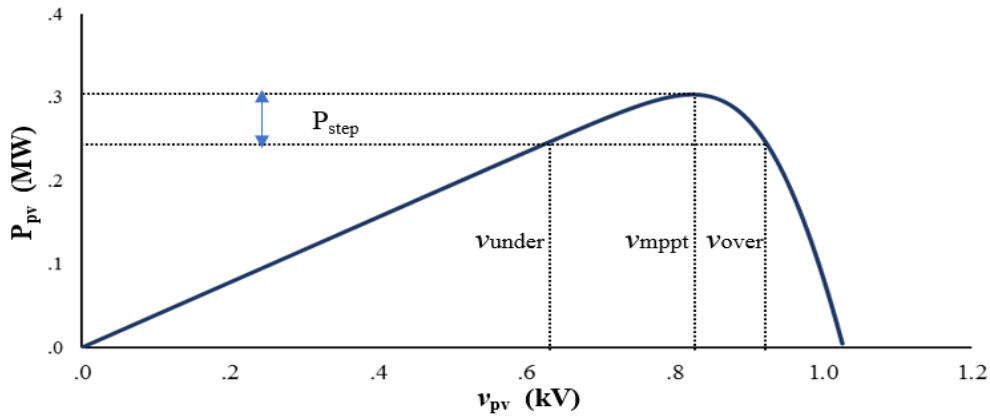
(b)

Fig. 4.4: Typical PV characteristics curves. (a) current, and (b) power versus PV voltage curve.

D. Active POD scheme in the Converter Controllers

Fig. 4.4 shows the usual characteristics curve of a 250 kW PV panel simulated in PSCAD. A PV plant is typically run on v_{mppt}, to get the most power out of the PV arrays and generate more

income. Nonetheless, any value below the maximum power point can be attained by diverting the dc voltage from this optimal operating point. As a result, if the PV plant operates under or overvoltage, it can produce additional active power. This remaining real power can be used in active power damping, providing a PV plant auxiliary service. The slope between v_{mppt} and v_{over} is steeper than that between v_{mppt} and v_{under}, as seen from the characteristic curves. As a result, if the MPPT is used in v_{over} mode, a more dynamic reaction is expected. We can eliminate the detrimental effect of an overvoltage by understanding the dc-link capacitor and future IGBT switches with a slightly higher voltage rating.

Fig. 4.5 depicts the boost converters' active POD system for the PV plant. To adjust the MPPT, an extra control function ΔV has been added. The value of ΔV can be calculated using the formula:

$$\Delta V = K_{\mathrm{dv}} \cdot v_{\mathrm{pv}} \tag{4.9}$$

where K_{dv} is a constant and can be determined from the lookup table of the characteristics curve.

The PV panel's reference power is $P_{\mathrm{ref}} = P_{\mathrm{MPPT}}$ and $\Delta V = 0$ in the pre-fault condition. The active POD is engaged when an oscillation is detected. Increased PV panel voltage within its voltage limits adds an extra margin ΔP to dampen the oscillation. The terminal bus voltage angle, δ, is used as the input for the damping control loop to achieve this oscillation damping, as this is one of the most critical indicators of system stress. Hence, a washout filter is used to filter δ from it. The residual real power function feedback for the damping control, ΔP, is obtained from the washout filter. ΔP can be calculated as follows:

$$\Delta P = \delta \times G_1 \times \frac{sT_{\mathrm{w1}}}{1+sT_{\mathrm{w1}}} \tag{4.10}$$

where G_1 and T_{w1} are the washout filters gain and time constant, respectively. In this work,

T_{w1} is set to 10 seconds.

When the oscillation is effectively damped over a period, the values of ΔV and ΔP gradually will return to zero.

Fig. 4.6 depicts MSC's active POD scheme for WPP. Because active power and the bus angle are closely related, δ from the POI has been used as feedback for this loop. This dampening technique uses the surplus power left as kinetic energy in the wind turbine. ΔP_1 is calculated as follows:

$$\Delta P_1 = \delta \times G_2 \times \frac{sT_{w2}}{1+sT_{w2}} \tag{4.11}$$

where G_2 and T_{w2} are the washout filter's gain and time constant, respectively. In this work, T_{w2} is set to 10 seconds.
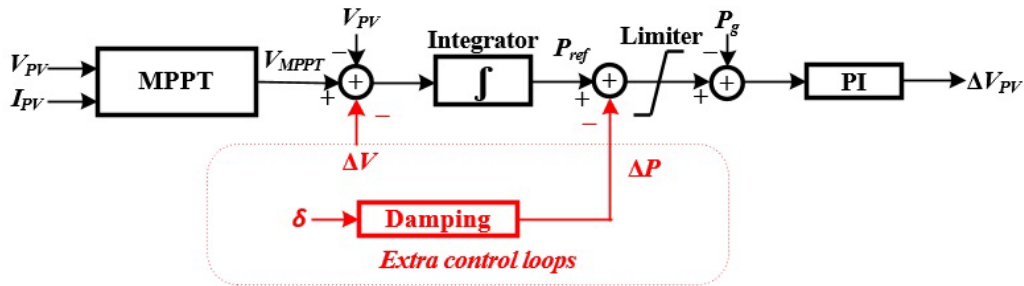
Fig. 4.5: Block diagram of Active POD controller mode of PV DC-DC converter.
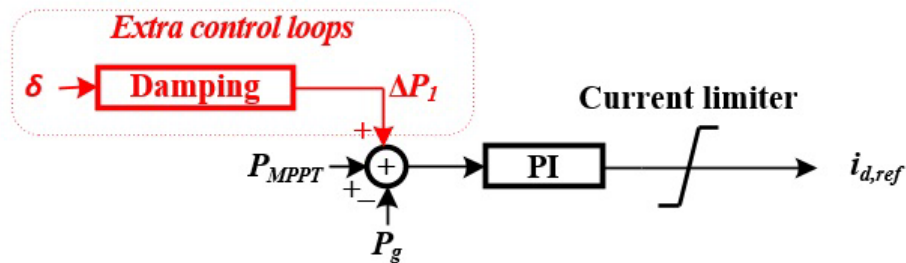
Fig. 4.6: Block diagram of Active POD controller mode of in WPP AC-DC converter.

E. Active and reactive POD controller scheme or Dual POD controller scheme

The full capacity of the PV plant is efficiently utilized using this controller. In this system, the plant's active power capacity is prioritized for active POD, while the residual reactive power capacity is likewise completely utilized for reactive POD.

The WPP's full capacity has also been used in this controller. The WPP will prioritize active power, with the remaining inverter capacity being used for reactive power damping. The feedback signal for the reactive POD is derived from the speed of the nearest connected synchronous generator, whereas the feedback signal for the active POD is taken as the bus angle from the POI.

4.2 The Coordinated control schemes of IBRs

The recommended features of control schemes that effectively support the electrical system during fault and post-fault conditions are described in this section.

The PV plant and the WPP include current limitation to safeguard the IGBT switches from large currents in the converters. The PV plant at night and WPP at day operate in Q priority mode during the fault, using the maximum current capacity for reactive power injection ($I_{qmax} = I_{limit}$). The available maximum and minimum active currents can then be calculated as follows:

$$I_{pmax} = \sqrt{I_{Limit}^2 - I_{qcmd}^2},$$
(4.12)

$$I_{pmin} = 0.$$
(4.13)

P priority, on the other hand, has traditionally been employed in post-fault situations. To employ the inverter's highest current capacity ($I_{pcmd} = I_{pmax} = I_{limit}$), active power will be given a greater priority. The values for I_{qmax} and I_{qmin} can be computed using the formulas below:

$$I_{qmax} = \sqrt{I_{Limit}^2 - I_{pcmd}^2},$$
(4.14)

$$I_{qmax} = -I_{qmin}. \tag{4.15}$$
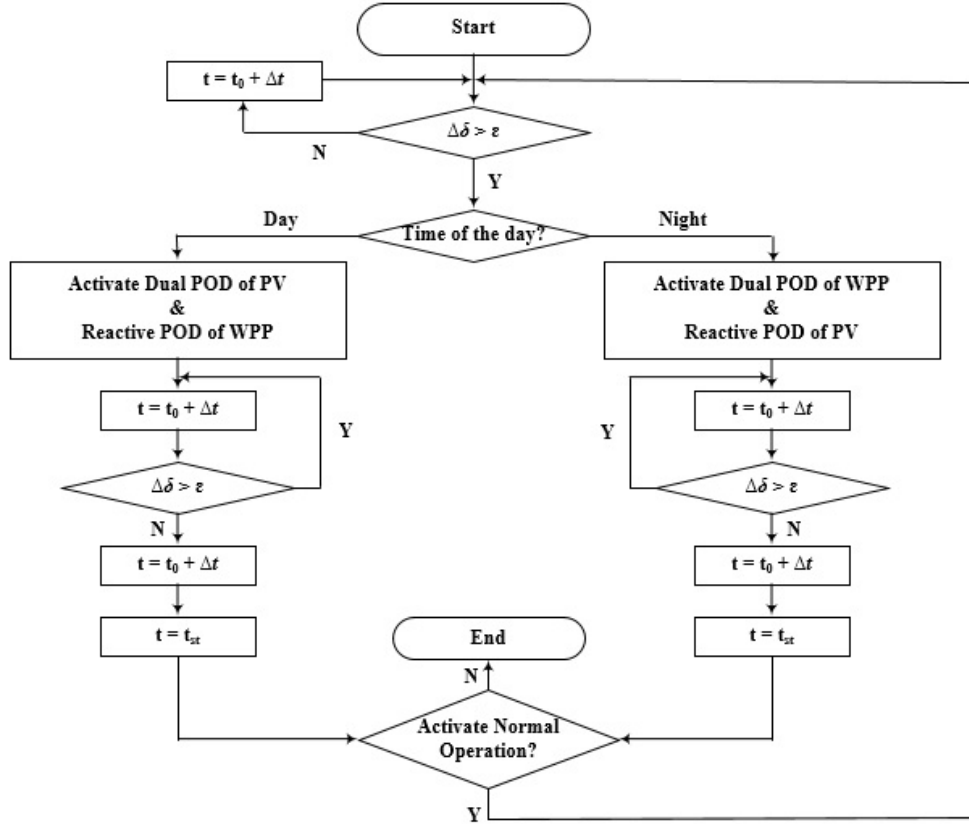
Fig. 4.7: Flow chart of the coordinated scheme.

A flowchart shown in Fig. 4.7 has been developed to coordinate the PV plant and the WPP connected to the grid. A predetermined value, $\varDelta\delta > \varepsilon$, has been set for the bus angle deviation, violating which the coordination systems get activated. The mode of operation is set according to the time of day. During the daytime, specifically between 6 am and 6 pm, the dual POD of PV and the reactive POD of WPP will be activated. At night, between 6 pm to 6 am, the dual POD of the WPP and reactive POD of the PV will be instructed to get activated. In the end, a counter has been added to check the bus angle deviation frequently for both cases. Once the oscillation is over, the system should return to its normal operation. Thus, at $t = t_{st}$, at steady-state, the normal operation

of previously planned load scheduling will be followed, and normal operation will be activated. t_{st} is the time recommended by the grid for restoration. The operator can manually stop the activation mode if the damping is not sufficient by the control scheme.

4.3 Modeling of Study Systems

This paper investigates the efficacy of POD schemes in PV and WPPs in inter-area low-frequency oscillation in a two-area system. For this, a two-area system consisting of two 2 GW hydro generators has been developed in PSCAD. The hydro generators in area 1 and area 2 are named G_1 and G_2, respectively. A 100 MW large-scale PV and a 120 MW WPP have been installed in area 2, as shown in Fig. 4.8. All the cases mentioned in Table 1 are made to examine the effectiveness of the damping controller proposed in the paper during the inter-area low-frequency oscillation. While the PV plant and WPP are supposed to function as PSS, no PSSs connected to the hydro generators.
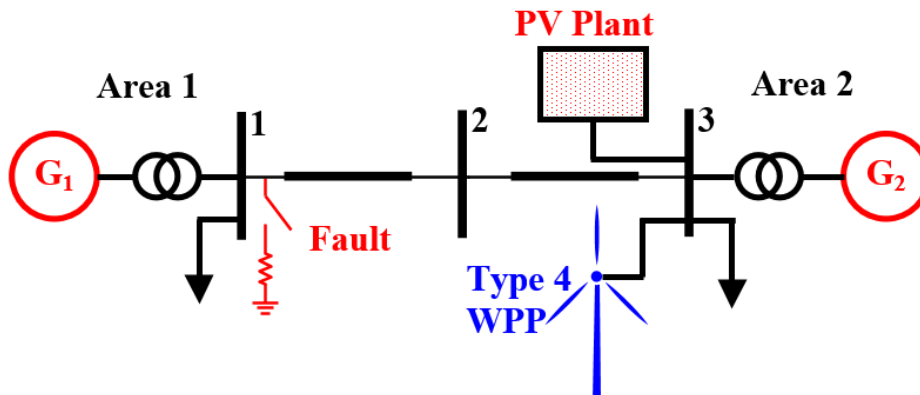
Fig. 4.8: Two-area system with utility-scale PV plant and WPP in area 2 and fault in area 1.

4.4 Case studies

All cases in Table 4.1 will be treated with an identical disturbance, a three-phase symmetrical short circuit without any fault impedance. The short circuit is located near Bus 1 in area 1 with a duration of 0.2 s. The short circuit will be eliminated from the system after 0.2 s.

TABLE 4.1
The Scenario of DIFFERENT CONTROL MODES OF POD

Case	RES	Control Modes	RES	Control Modes
Case 1	PV	Dual	WPP	OFF
Case 2	PV	OFF	WPP	Dual
Case 3	PV	Dual	WPP	Reactive
Case 4	PV	Reactive	WPP	Dual

Four Cases have been considered, where Case 1 only functions when PV dual POD is turned on. Case 2 functions when only WPP dual POD is turned on. The alternative RES is still inactive and disconnected in each of these situations. Case 3 offers damping with both a reactive POD of WPP and a dual POD of PV. In Case 4, WPP offers dual power damping, while PV offers reactive damping with corresponding PODs. With the plans above, we will attempt to reduce the oscillation caused by utility-scale PV and WPP coupled in Area 2.

A. Case Study: Two-Area System

The active power output of areas 1 and 2 are shown in Figs. 4.9(a) and (b), respectively. From Fig. 4.9, we deduced that each damping controller effectively reduces the inter-area oscillation. However, among the other examples for both areas,
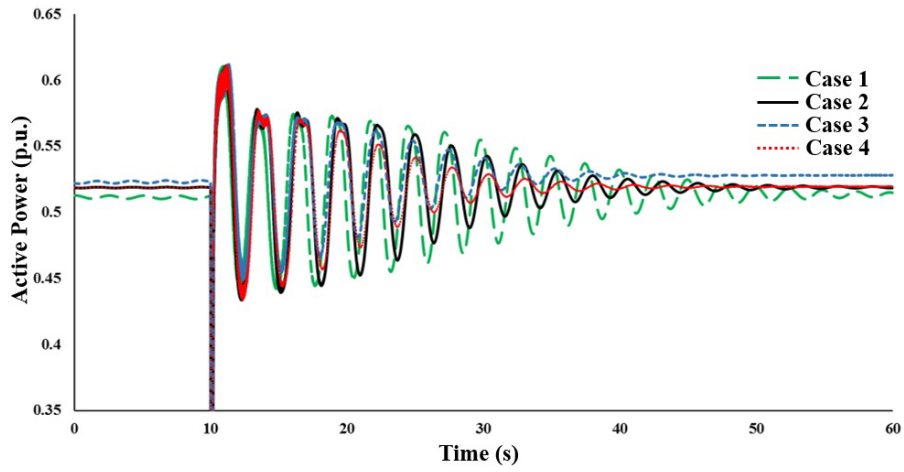
(a)
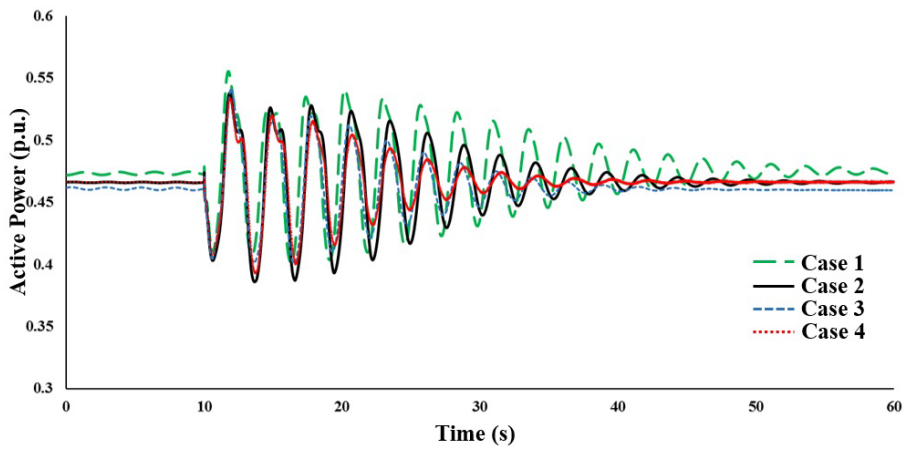
(b)
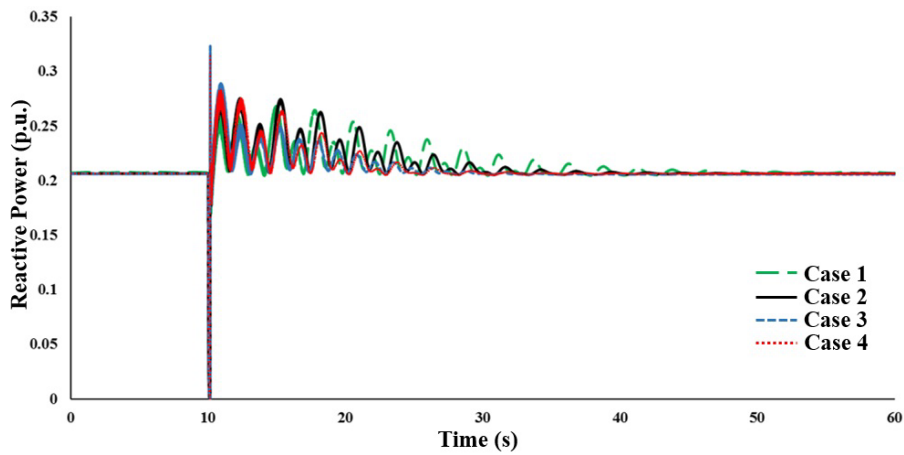
(c)
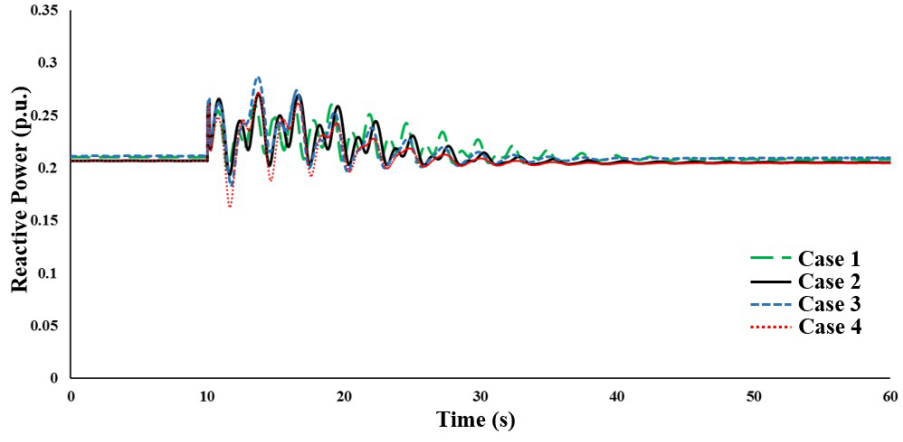
(d)
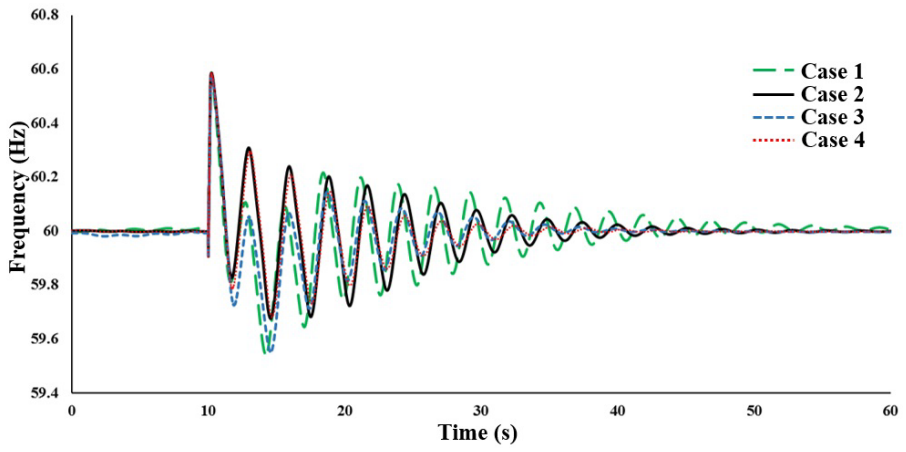
(e)
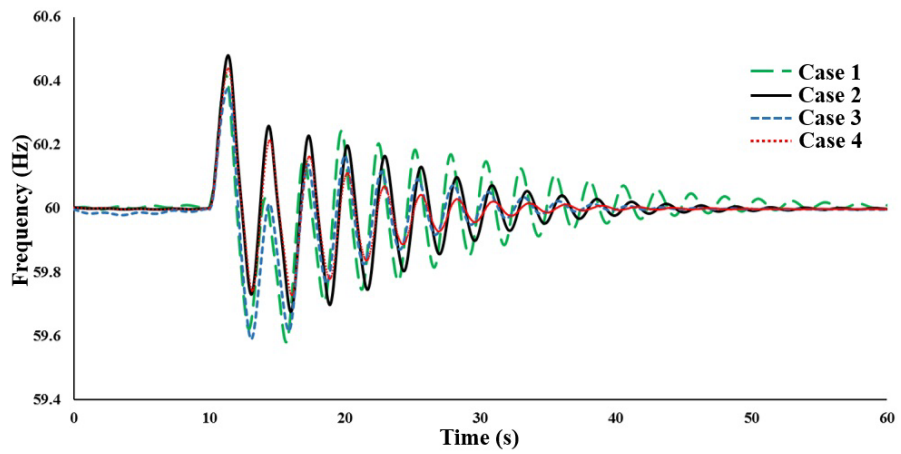
(f)

Fig. 4.9: Hydro Generators output for each of the cases during fault and post fault conditions. (a) active power output of G1 in area 1. (b) active power output of G2 in area 2. (c) reactive power output of G1. (d) reactive power output of G2 (e) frequency output of G1. (f) frequency output of G2.

Cases 3 and 4 damped power oscillation the fastest. Dual POD and Reactive POD are used in both circumstances and with the RESs available during that time of the day. Case 1 took the longest time due to the lower capacity of the PV plant than the WPP. It signifies that the capacity of the RES has a significant role in damping the oscillation. It is also apparent that the proposed scheme of combining dual POD and reactive POD of two separate RESs damped the oscillation much faster than the other two cases with regular dual POD cited in this article.

Areas 1 and 2's reactive power output plots are shown in Figs. 4.9(c) and (d). Like active power, reactive power has also shown similar results. Case 1 took the longest, while Case 3 and Case 4 settled down the quickest. Once the oscillation is completely damped, the reactive power output for all schemes returns to its initial position.

The frequency in buses 1 and 2 during the fault and the post-fault conditions are depicted in Figs. 4.9(e) and (f), respectively. For both Cases 3 and 4, the frequency settles faster than in Cases 1 and 2.
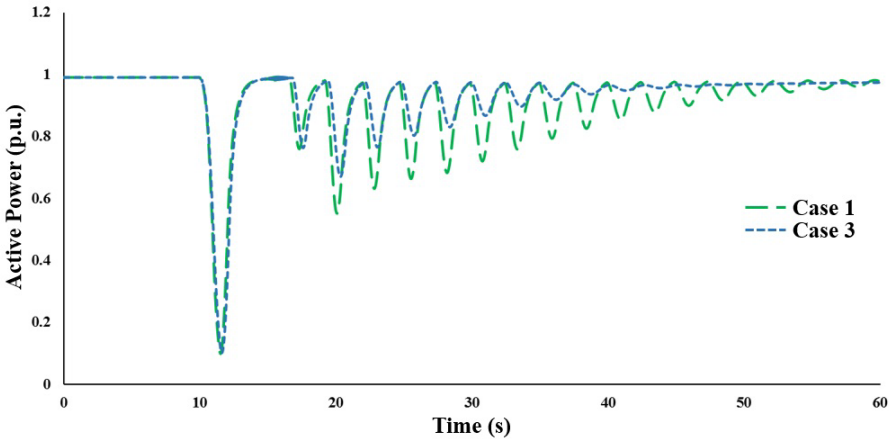
(a)
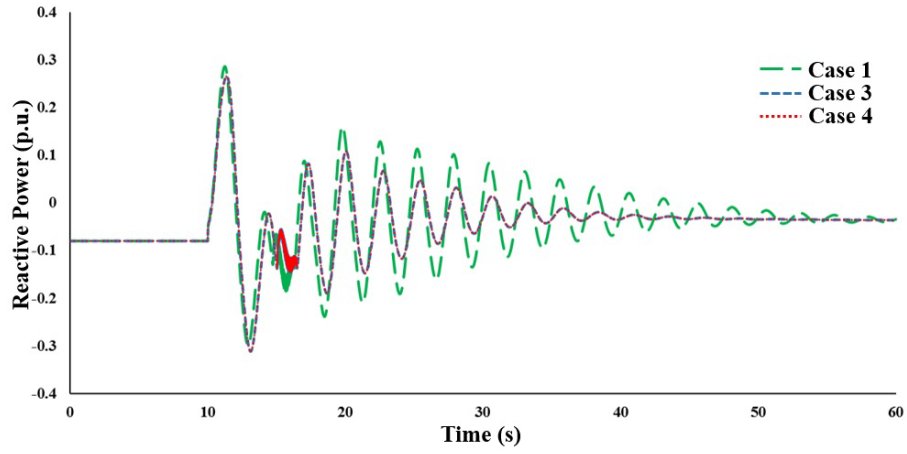
(b)
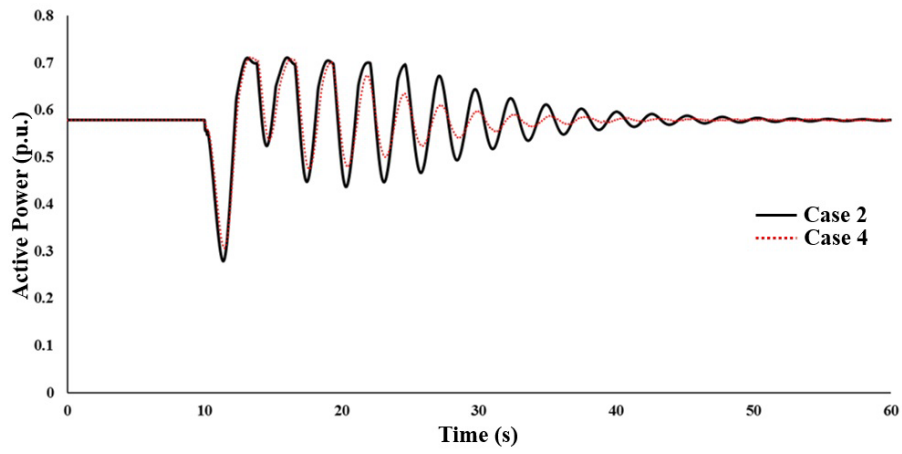
(c)
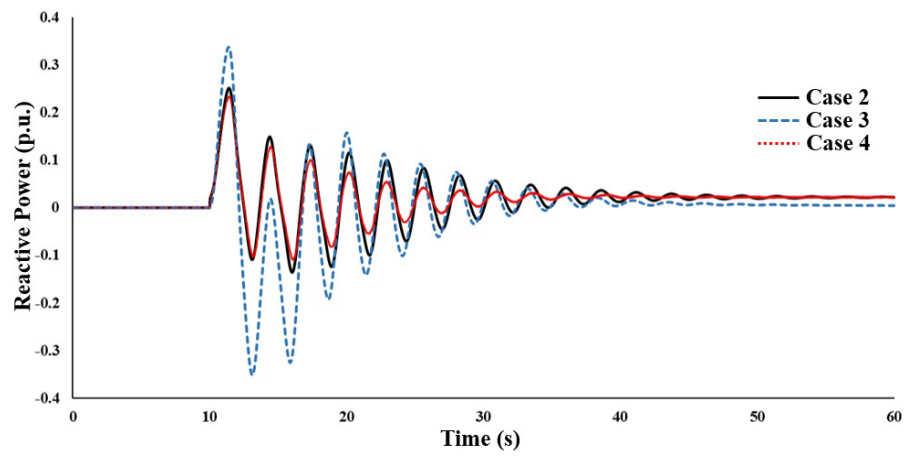
(d)
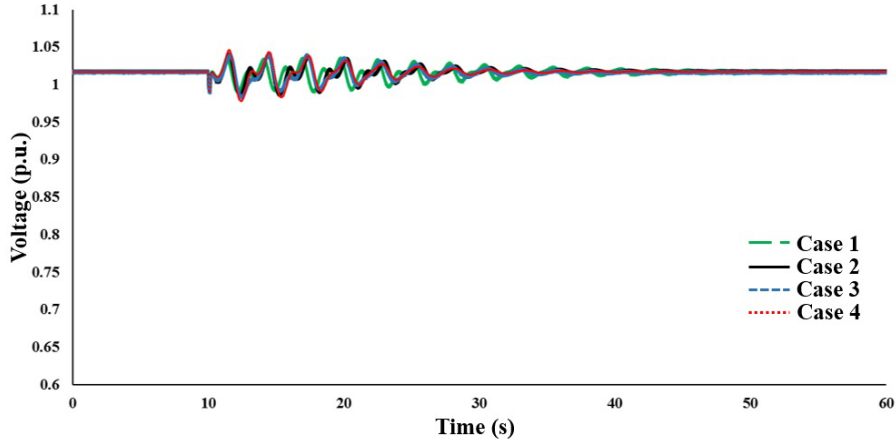
(e)

Fig. 4.10: PV plant and WPP output at the POI during fault and post fault conditions. (a) PV active power output. (b) PV reactive power output. (c) WPP active power output. (d) WPP reactive power output. (e) voltage output at POI.

Fig. 4.10(a) illustrates the PV plant's active power output at the POI. The damping curve in a PV plant is restricted to 1 p.u. due to active power limitations. Because the output of the other examples is negligible for this usage, only Case 1 and Case 3 are plotted here. It has been observed that Case 3, works much faster than Case 1. Hence, we concluded that the reactive POD from the WPP has provided significant support to dampen the oscillation.

Fig. 4.10(b) shows the reactive power needed for damping the inter-area low-frequency oscillation in the present PV plant capacity. Cases 3 and 4 seem to provide an equal amount of reactive power to dampen the oscillations. The full capacity of the PV can also be used in Case 4. However, sufficient damping has been offered even after putting a current limiter to limit its reactive power capacity.

Fig. 4.10(c) depicts the WPP's active power output during and after the fault clearance. The power has been restricted by using current limiters in the control loops because the operating voltage is the same in all circumstances. Case 4 seems to be much more efficient compared to the other schemes. This is due to the support provided by the PV to dampen the oscillation with its

61

reactive POD.

Fig. 4.10(d), highlights the reactive power output of the different POD schemes implemented in the WPP. The fluctuation is the highest for Case 3 due to the need for more reactive power compared to PV, as the capacity of the PV plant is less. The oscillation mitigates the fastest for cases 3 and 4.

The voltage fluctuation is almost the same for all the cases in Fig. 4.10(e). All the schemes maintain the voltage within the acceptable limit with slight fluctuations.

4.5 Conclusion

In conclusion, Chapter 4 has undertaken a comprehensive analysis of the potential of leveraging a utility-scale Photovoltaic (PV) and Wind Power Plant (WPP) in damping inter-area low-frequency oscillations through the application of various Power Oscillation Damping (POD) schemes. In the context of a two-area system, a fault simulation at area 1 for a duration of 0.2 seconds served as the testing ground for these schemes. The anticipated goal was to assess their effectiveness in dampening oscillations induced by the fault and its subsequent clearance.

The findings of this study revealed that the proposed POD schemes in Cases 3 and 4 exhibited remarkable efficiency in dampening inter-area low-frequency oscillations at a quicker rate compared to the regular dual POD scheme. Despite the localized operation of reactive power, the addition of the reactive POD in these cases demonstrated promising results. This suggests that combining the dual POD and reactive POD simultaneously, with appropriate coordination based on the time of day, can yield efficient and faster damping than conventional POD schemes.

Looking ahead, Chapter 6 will further enhance our understanding by evaluating the power output of the respective areas. This additional analysis will provide valuable insights into the

damping provided by this coordinated scheme, offering a more holistic perspective on its effectiveness in mitigating inter-area low-frequency oscillations.

Chapter 5

Development of AVR For Type 5 WTG and Power Oscillation Damping with Type 5 WPP

In recent times, the energy sector has experienced a significant transformation due to the widespread adoption of renewable energy generation (REG). Recent data reveals that there has been a remarkable increase in global REG capacity. In 2019, it grew by 176 GW [66], and by the end of 2020, the annual REG capacity had reached approximately 2800 GW [67]. Among various renewable energy sources, wind power has emerged as the fastest-growing technology for energy generation on both onshore and offshore. According to the GWEC, more than 90 GW of new wind power was installed in 2020 [68]. In comparison to 2019, the global newly installed wind capacity expanded by 53% in 2020, comprising 86.9 GW onshore and 6.1 GW offshore [68]. Consequently, the total installed wind capacity now stands at 743 GW.

Type-3 and Type-4 wind turbine generators, known as modern variable-speed wind turbines, utilize power electronics converters, either partially or fully rated, to enable variable-speed operation. This design approach serves the dual purpose of meeting the operational demands of the turbines themselves and facilitating integration with the power system [69]. As the integration of renewable energy continues to grow and conventional SGs plants are being replaced, WTGs are now expected to assume the role of reliable energy sources for the electric grid, a responsibility traditionally held by SGs. This shift has prompted a keen interest among power system engineers in the grid-forming (GFM) control of Type-3 and Type-4 wind turbine generators [70], [71].

It has been observed that droop-controlled GFM converters, operating as first-order nonlinear systems, exhibit superior stability compared to phase-locked loop (PLL)-based grid-

following (GFL) converters, which function as second-order nonlinear systems. Despite the recent advancements in GFM control of Type-3 and Type-4 wind turbine generators, there are still several unresolved issues that require further investigation.

One of the uncertainties surrounding GFM inverters is their ability to achieve successful resynchronization after a fault is cleared without relying on grid information during the fault, even though they may offer "virtual inertia." Additionally, these inverters are not economically viable for providing high fault currents. Furthermore, inverters have been found to have high failure rates, lacking the longevity and reliability offered by the combination of SGs and AVRs. While the concept of an inertialess grid solely reliant on IBRs may theoretically address certain grid stability issues, it is not a practical solution, particularly during the transitional phase. It is important to note that IBRs will heavily depend on software for managing grid-scale coordination, which represents a significant departure from the robust electromechanical behavior of SGs that has historically ensured grid stability since the late 19th century. These issues can be partially mitigated by either oversizing the capacity of GFM inverters or with large-scale deployments of synchronous condensers (SCs), but both solutions are not cost-effective [69].

A solution for grid-forming wind turbine generators that maintains grid strength has been in existence since the 1990s. However, limitations in mechanical advancements and an excessive focus on power electronics hindered its progress in the energy market. This solution is commonly referred to as synchronous wind power or Type-5 wind turbines. These turbines operate as variable-speed systems and interface with the grid through a fixed-speed SG. Two methods are employed: a hydrodynamic coupling between the SG's shaft and the gearbox (e.g., the German DeWind D8.2 2-MW wind turbine) [72], or a hydrostatic torque reaction incorporated in the turbine gearbox with torque limiting (e.g., the SyncWind powertrain concept utilized in Windflow

wind turbines in New Zealand) [73].

Type-5 turbines consist of a standard wind turbine generator with a variable-speed drive train connected to a torque/speed converter that interfaces with a synchronous generator [69]. The torque/speed converter ensures a constant output shaft speed by converting the variable speed of the rotor shaft. The synchronous generator is appropriately designed for a specific desired speed (typically 6 or 4 poles) and voltage (usually medium voltage for higher capacities). This approach necessitates speed and torque control of the torque/speed converter, along with the inclusion of a voltage regulator, synchronizing system, and generator protection system inherent to a grid-connected synchronous generator. Consequently, the utilization of Type-5 wind turbine generators, which operate without power converters, provides comparable features to traditional power plants while being adapted to the requirements of variable-speed operation driven by a prime mover (the wind rotor, in this case).

In recent years, research and practice investigations have been carried out on transient stability with high penetration of WPPs. Different FRT schemes are studied for IBR-based WPPs, such as adding a crowbar with dc link chopper [74], crowbar with battery [75], bridge type fault current limiter (FCL) [76] dynamic voltage restorer with FCL function [77]. As in frequency control, the first step in an additional POD controller for WPP is to imitate the PSS from the synchronous generators [53]. Proper tuning to adjust PSS parameters provided promising results [54]. The voltage of the POI of the WPP is chosen as input and a variation of power reference as output. The conventional PSS scheme has been evaluated by inputs such as local and remote signals and voltage variation as output [42].

However, the limitations of IBRs with high voltage and current make the Type 5 wind turbine generators (WTGs) a better option to ride through the fault with regularly used excitation

control available in the market. Auxiliary services like FRT or supporting the grid to damp out the power oscillation can easily be incorporated on the Type 5 WTGs. The excitation system must take responsibility for providing these services. The basic requirement for excitation systems is to provide and adjust the excitation current of generators to maintain the terminal voltage in the right levels. Over the years, different excitation systems have been applied for different stability purposes [78].

In this section, the theoretical framework of the dynamic model for various types of AVRs designed for Type 5 synchronous generators has been explored. Subsequently, a dynamic model for a suitable AVR has been created using electromagnetic transient (EMT) modeling software called "PSCAD." The effectiveness of the selected AVR model has been demonstrated through different case studies. Furthermore, the capacity of the AVR model to dampen power oscillations has been assessed within the context of a two-area model.

5.1 Development of Theoretical Concept

This section describes the theoretical concept of exciter suitable for Type 5 WTGs to provide various functionality by covering mathematical model and control frameworks. This section deal with the followings: Comparison of different available exciter models, a dynamic model of the AVR for Type 5 synchronous generator wind power, development of the mathematical model and control framework for the AVR and specifics of AVR control to operate during normal transients with appropriate damping in strong and weak grid conditions.

A. Comparison of different AVR models

The primary function of excitation systems is to supply and regulate the excitation current of generators in order to maintain the terminal voltage at appropriate levels. Over the years, various excitation systems, such as static, AC, and DC exciters, have been employed for different stability

objectives [78]. Static exciters typically utilize commutators, slip rings, and brushes. However, the utilization of this solution has declined significantly in recent times due to drawbacks such as significant resistive voltage drops caused by brushes and the need for periodic maintenance and replacement of the slip rings due to mechanical wear and tear [79].

A more robust and modern approach to address these issues is the utilization of Brushless Excitation (BLE) systems, which provide field current without any voltage drop in brushes [80]. BLE systems essentially function as Auxiliary Synchronous Generators (ASGs), delivering rectified AC voltage to the excitation winding in the rotor of the main SG. The AC voltage generated by the ASG is converted to DC through a passive diode-bridge rectifier, thereby producing the excitation current for the exciter of the main generator. BLEs are commonly employed in aircraft and marine applications where safety and reduced maintenance are paramount concerns.

Compared to static excitation systems, conventional exciters exhibit poor transient response of the field current due to two key factors: (a) The inability of the diode bridge rectifier to generate a negative voltage across the field winding, and (b) The indirect control of the main field current through the exciter field current [81].

It should be noted that both synchronous generators and excitation systems must comply with grid standards [82]. This entails adherence to ceiling voltage and step response standards [83]. For instance, the UK grid code mandates that when the field voltage changes from 90% to 100% during open circuit conditions, the generator's terminal voltage should reach 1 per unit (p.u.) within 0.6 seconds. Another important requirement of grid codes is the provision of a higher ceiling voltage, which enhances the response time of the field winding current. Additionally, excitation systems should possess fault-ride-through capability. Consequently, the excitation system of Type-

5 WPPs can be expected to deliver similar performance in this regard.

In Fig. 5.1, a static exciter is depicted, featuring a negative current logic that is not present in BLE systems. The terminal voltage, V_T, is compared with a reference voltage, V_{Ref}, and then passed through a phase compensator and a washout component. Similar steps are followed in BLE systems, but without the application of negative current logic. Despite a few drawbacks associated with BLE, its reliability as an excitation system outweighs any potential negative circumstances, making it the preferred choice for providing efficient excitation to the system.
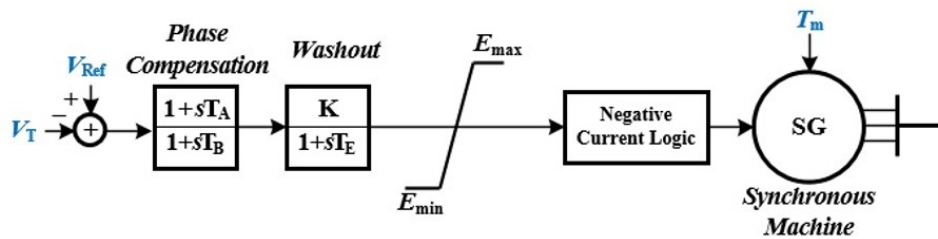
Fig. 5.1 Block diagram of a Static Exciter

Figure 5.2 illustrates the active power output during a 100ms (usually we use 5 - 9 cycles in most grid-codes) three-phase to ground fault at the terminal in a grid-connected Type-5 wind turbine. In Fig. 5.2(a), the output power is compared using a static exciter, while Fig. 5.2(b) displays the output using a rotating BLE system. Both excitation systems exhibit similar performance in terms of output. Although the static exciter appears to have a slightly faster response, the advantages of reduced maintenance and enhanced safety make the BLE the preferred choice for Type-5 wind turbines.

(a)

BLE System
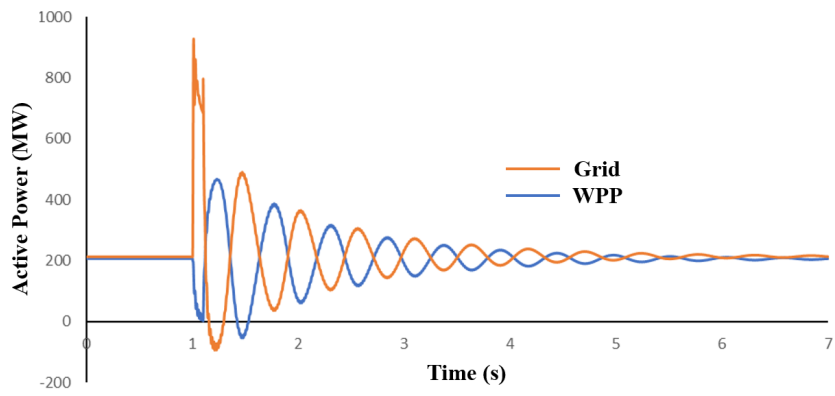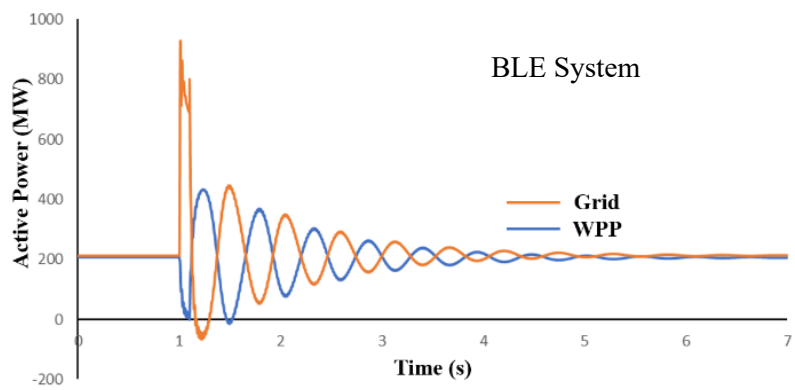
(b)
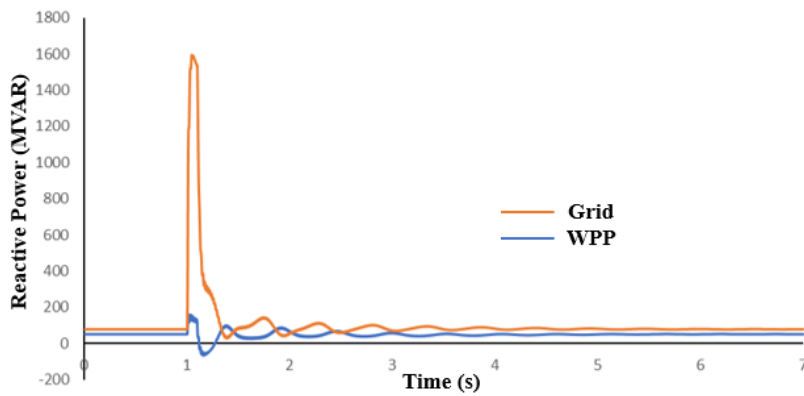
(c)
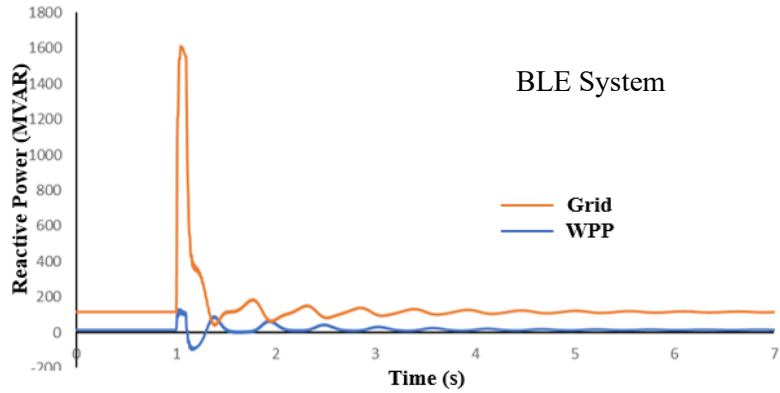
(d)
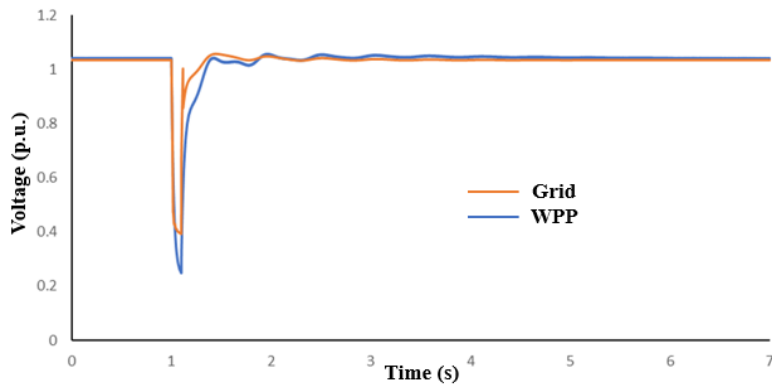
(e)
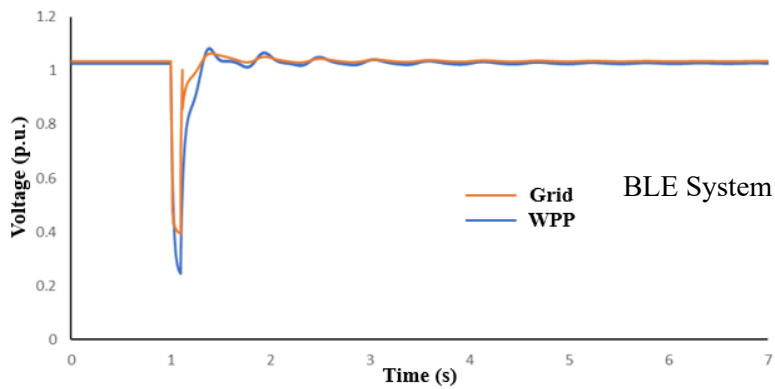
(f)

Fig. 5.2 Output of the Grid and WPP. a) active power output with static exciter (ST4A), b) active power output with rotating brushless exciter (AC1A), c) reactive power output with static exciter (ST4A), d) reactive power output with rotating brushless exciter (AC1A), e) voltage at the terminal with static exciter (ST4A), f) voltage at the terminal with rotating brushless exciter (AC1A)

Subsequently, the comparison of the reactive power output and the corresponding terminal voltages as shown in Fig. 5.2(c) through Fig. 5.2(f) convinced us that the performance of the BLE System is almost identical to the conventional exciter.

5.2 Proposed dynamic model of the AVR for Type 5 WTG

The Standard BLE system comprises an exciter, an inverted synchronous generator, and an uncontrolled rotating diode bridge rectifier that provides excitation to the synchronous generators. Fig. 5.3 depicts a representation of a synchronous generator with a brushless excitation system. The primary advantage of this configuration is the elimination of the power slip ring-brush system on the rotor winding of the synchronous generator, resulting in reduced maintenance costs.
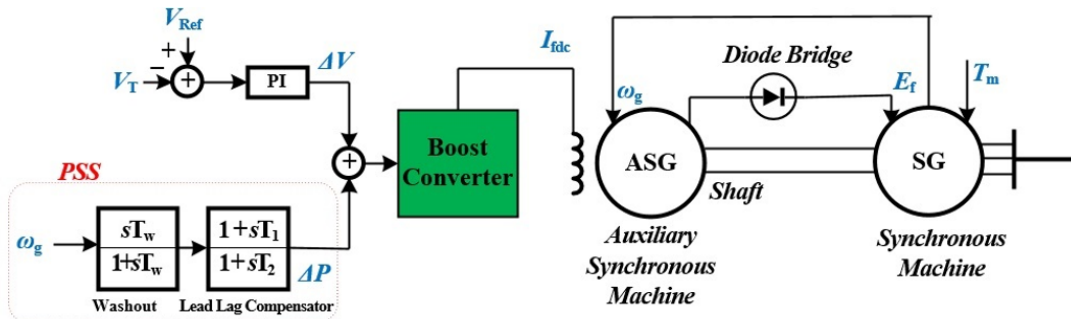
Fig. 5.3 Block diagram of the BLE

Previous studies [84] have indicated that the performance of BLE systems is constrained by the inability to rapidly de-excite the generator due to the rotating diode bridge's incapability to deliver negative excitation voltage. This limitation reduces the dynamic response of the generator's voltage regulation during load shedding and may lead to voltage overshoot at the synchronous generator's terminal [84]. To enhance the dynamic behavior of the voltage regulation loop,

researchers have proposed advanced control strategies [85]. However, these control strategies are unable to mitigate the generator voltage overshoot during load rejections because of the inherent limitation of the diode bridge, which cannot generate negative excitation voltages.

However, their improved efficiency, reduced maintenance requirements, and adaptability make them a compelling option for various industries and applications. However, their successful implementation requires careful design, monitoring, and maintenance of the associated control systems. Therefore, a simplified aggregated BLE system has been developed in PSCAD, focusing on its advantages, and disregarding its disadvantages.

A.1 Main Synchronous Generator

The main synchronous generator of the Type 5 WPP is designed as shown in Fig. 5.4. A constant torque from the torque converter is provided to the SG. The field winding is fed by the ASG.
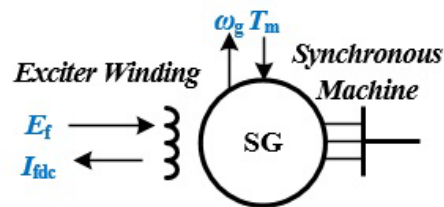
Fig. 5.4 Schematic diagram of the main SG.

A.2 AVR and PSS

The voltage error is passed through a PI controller and is added to the output of PSS. Addition of them provides the duty ratio, DR, used in boost converter.
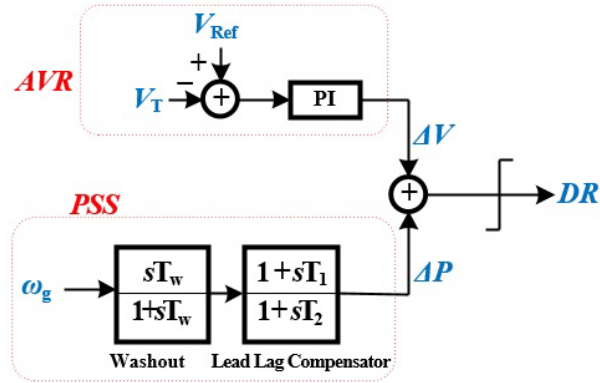
Fig. 5.5 Schematic diagram of AVR and PSS

A.3 Auxiliary SG

Fig. 5.6 illustrates the configuration of the ASG in the system. The ASG supplies power to the diode bridge rectifier. The resulting DC voltage, E_f, is then supplied to the main SG. The output of the diode bridge rectifier is regulated by the current of the exciter in the main SG. Both the main SG and ASG are mounted on the same shaft, allowing the speed of the SG to be fed back to the ASG. The field voltage, E_{af}, is provided by the boost converter.
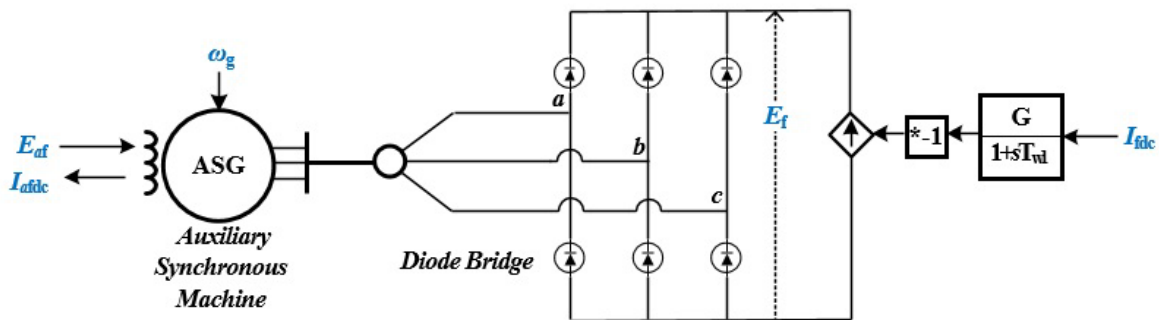
Fig. 5.6 Schematic diagram of ASG.

A.4 Boost Converter

The boost converter provides the voltage, E_{af} to the ASG. The duty ratio, DR from the combination of AVR and PSS is compared with a triangular wave to produce the switching signal for the IGBT switch in the boost converter.
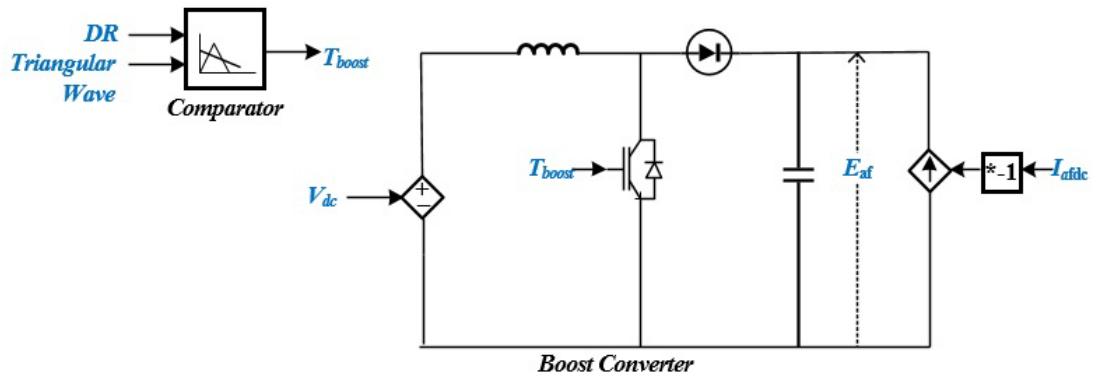
Fig. 5.7 Schematic diagram of the boost converter

B. Develop mathematical model and control framework of the system

In this section the mathematical model and control framework of the system has been discussed.

B.1 WPP System Model

The configuration of an aggregated WPP model used in this paper is depicted in Fig. 5.8. The WPP model consists of a wind turbine, drive train, hydrostatic torque converter, synchronous generator, and brushless exciter.
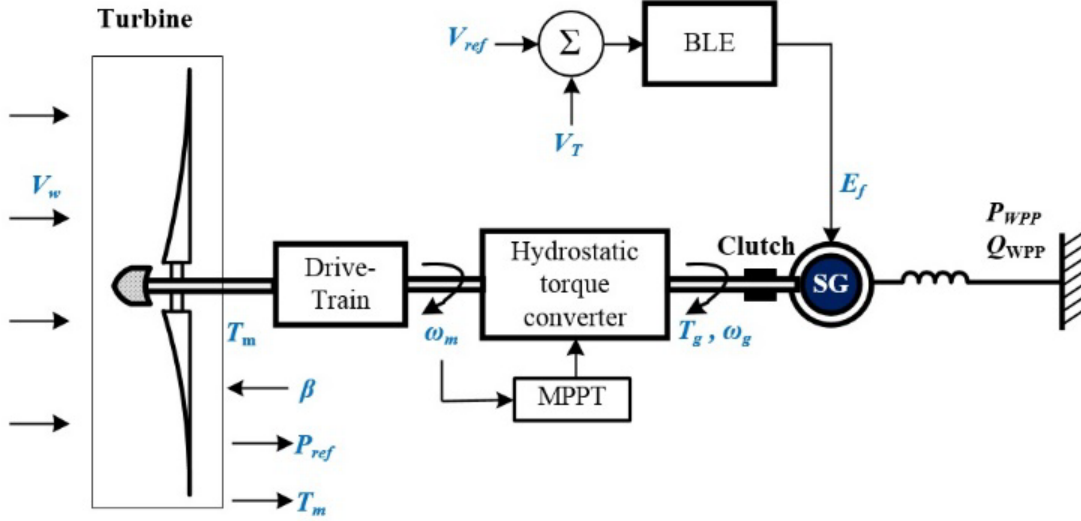
Fig. 5.8 WPP system model configuration.

The power extracted by the turbine blade can be calculated using:

$$P_w = \frac{1}{2}.\rho.\pi.R^2.V_w{}^3.c_p(\lambda,\beta) \qquad (5.1)$$

where P_w represents the extracted mechanical power from wind in Watts, R is the radius of turbine blade, β is the blade pitch angle in degrees, λ is the tip speed ratio determined by:

$$\lambda = \frac{\omega_t.R}{V_w} \qquad (5.2)$$

where ω_t is the mechanical rotational speed of the turbine in rad/s. c_p and λ were interpolated using non-linear equations.

The maximum output power of the wind turbine is obtained by tracking the rotor speed to the optimum point λ_{opt} that yields the maximum aerodynamic efficiency. Therefore, the optimum wind turbine speed is given as:

$$\omega_{t,opt} = \frac{\lambda_{opt}.V_w}{R} \qquad (5.3)$$

The machine's rotational speed ω_m, can be found from the gear ratio, GR, in the drive train,

$$\omega_{m,opt} = \omega_{t,opt}.GR \qquad (5.4)$$

Therefore, the maximum power is obtained as:

$$P_{MPPT} = \frac{1}{2} . \rho . \pi . R^2 . \left(\frac{\omega_{m,opt} . R}{\lambda_{opt}}\right)^3 . c_{p,max} \tag{5.5}$$

Equation (5) can be rewritten as:

$$P_{MPPT} = K_g \omega_m^3 \tag{5.6}$$

where K_g is the coefficient of the MPPT curve.

The turbine end of the torque converter is connected to the impeller side, and the generator side is connected to the turbine. The torque is converted by the static reactor placed in the middle of the impeller and the turbine [86]. The torque limiting features can be applied to this. The lock-up clutch is connected to the turbine and shaft of the synchronous generator.

The torque provided to the synchronous generator by the torque converter can be expressed as:

$$T_g = H(s) . \left(\frac{P_{MPPT}\left(\omega_m^3, \ \beta\right)}{\omega_g}\right)^3 \tag{5.7}$$

where ω_g is the mechanical rotational speed of the SG in rad/s.

The simplified dynamics of the torque converter, *H(s)*, is represented by a second order transfer function.

B.2 Brushless Exciter

The excitation system for this paper is a combination of ASG and diode bridge rectifier coupled and driven by the same shaft as the main SG. The DC field current of the field winding of the ASG is supplied by the boost converter connected with two control loops. The excitation of the ASG comprises two separate loops - one loop for regulating the terminal voltage and another loop to replicate the PSS added to the dependent voltage source.

The difference in the SG's terminal voltage, V_T, and the reference voltage, V_{Ref} controls the AVR loop. The difference is sent through a PI controller to get the ΔV.

To implement and integrate the active POD (simulated PSS) into the BLE System, the rotational speed of the main SG, ω_g, is fed to the washout filter to remove the steady-state component. The lead-lag compensator has compensated for the delay. The real power reference for the PSS, ΔP, is obtained by:

$$\Delta P_{oscillation} = \omega_g \cdot \frac{sT_w}{1+sT_w} \cdot \frac{1+sT_1}{1+sT_2} \tag{5.8}$$

where T_w is the time constant of the washout filter. T_1 and T_2 are the lead and the lag time constant, respectively. In this case, we can say the design logic of PSS is same for conventional SG and Type 5 wind turbine (refer to the control diagram shown in Figure 5).

The ac voltage of the ASG is transformed to dc (E_f) by a non-controlled rectifier, this way producing the excitation current of the main generator. The output torque, T_m, from the torque converter, is also fed to the main SG.

5.3 Case Studies

The model demonstrates the stable performance in grid forming mode and provide several services to the grid, including:

5.3.1 Case 1: Single Machine connected to Grid via Transmission line.

A. Normal operation under realistic wind conditions

Here the normal operation of the Type 5 with BLE has been evaluated in PSCAD software. In Fig. 5.9, a 200 MW WPP with Type 5 WTGs is connected to the Grid in area 2 via transmission line. A three phase to ground faults has been made in the middle of the transmission line and the performance and contribution of the WPP has been investigated in this section.
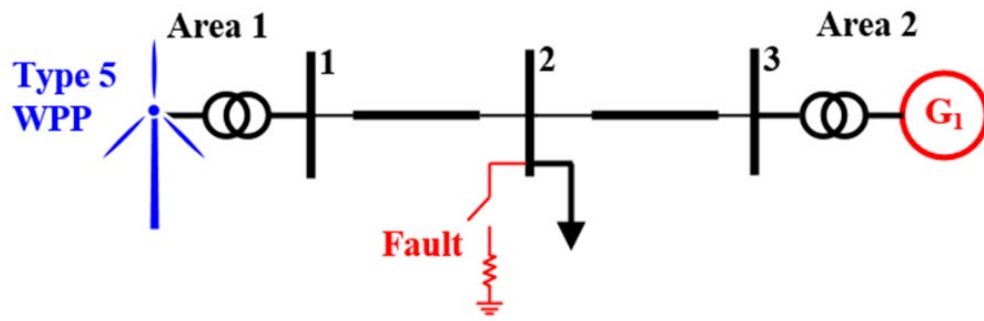
Fig. 5.9 Schematic diagram of Type 5 WTG connected to the Grid
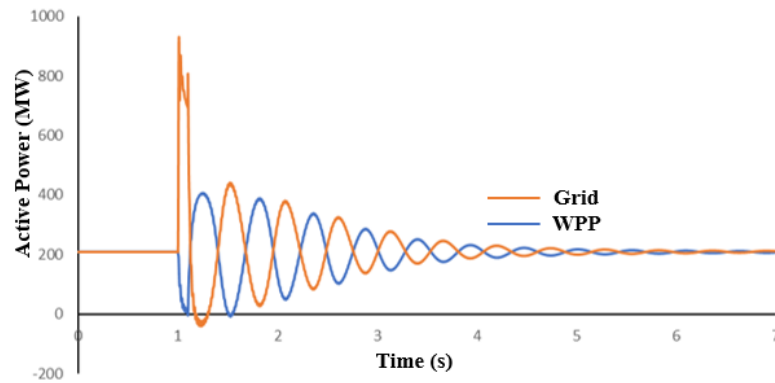
(a)
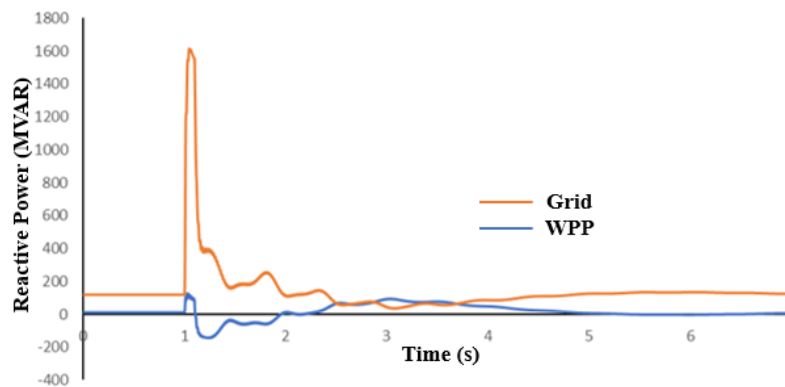
(b)
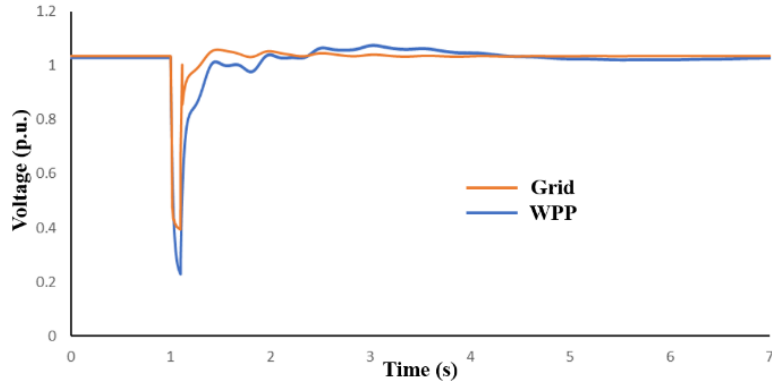
(c)

Fig. 5.10 The output of Grid and WPP during fault and post fault condition. (a) active power output. (b) reactive power output. (c) voltage output.

The output of the WPP in Fig. 5.10 shows the efficacy of the BLE modeled in PSCAD. The WPP is riding through the fault maintaining proper voltage at its output.

B. Operation under extreme simulated wind ramps

In this portion, the excitation system of the Type 5 plant is evaluated under different wind conditions. The wind speed is increased gradually from 18m/s to 30m/s. A three phase to ground fault of .10 s duration is made at 5 s. The WPP successfully rode through the fault. The WPP stopped producing active power when the wind speed went beyond 25m/s as this is the cut-off speed of the WTG.

.
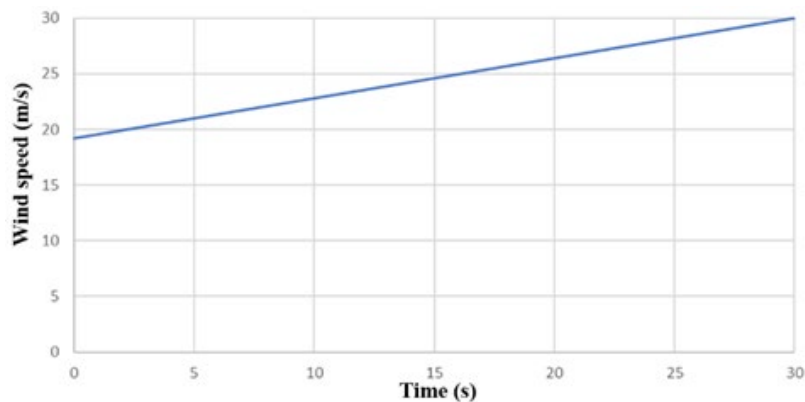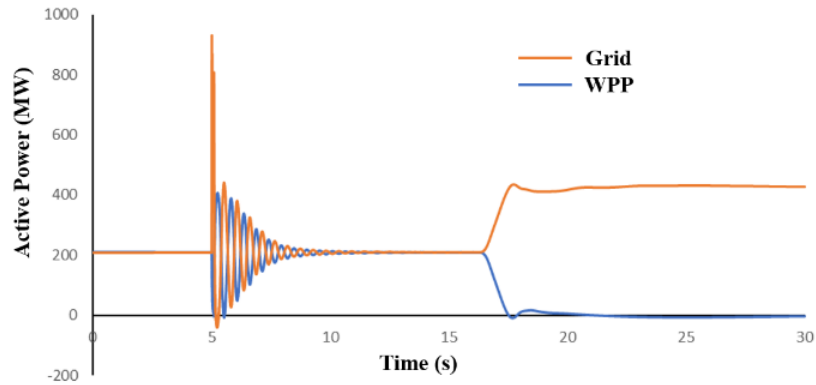
(b)
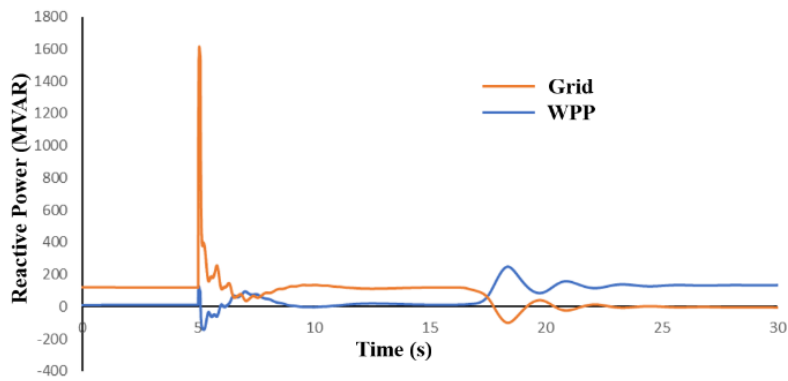
(c)
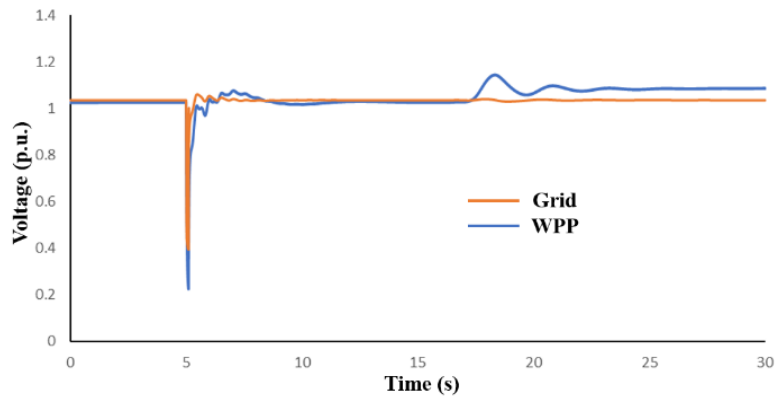
(d)

Fig. 5.11(a) Wind ramp with gradual increase in speed, (b) active power output, (c) reactive power output, (d) voltage output.

In this section, the wind speed data is obtained from the Turbsim software provided by

NREL. An average wind speed of 23 m/s has been generated and used to evaluate the performance of the WPP.

During the testing, a three-phase to ground fault with a duration of 0.10 s is introduced at 2 s to assess the fault-ride through capability of the WPP. The analysis of the output in Fig. 5.12 demonstrates that the WPP effectively withstands the fault and maintains its operation, indicating its ability to handle and recover from such disturbances.

However, it is important to note that when the wind speed exceeds 25 m/s, which is the cut-off speed of the Wind Turbine Generator (WTG), the WPP ceases to produce active power. This feature is implemented as a safety measure to protect the WTG from operating under extreme wind conditions.

(a)

(b)
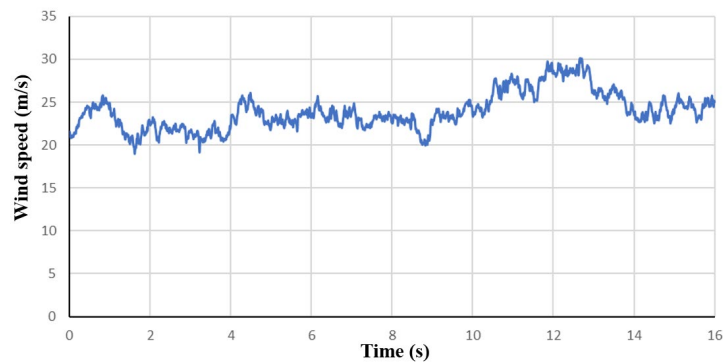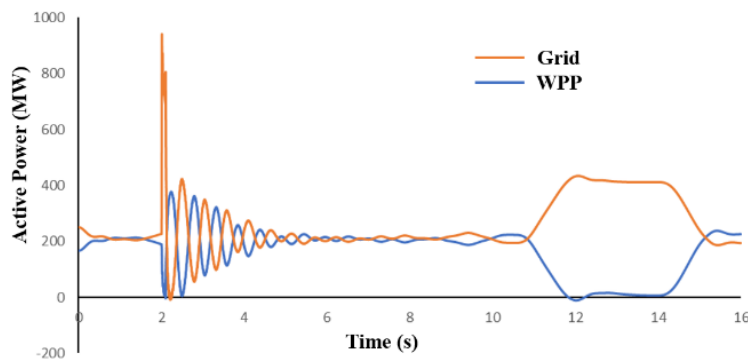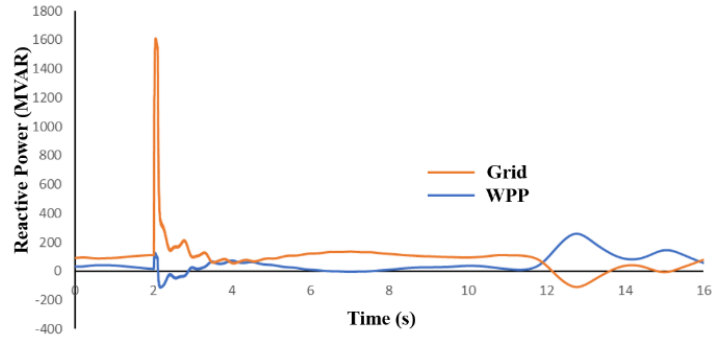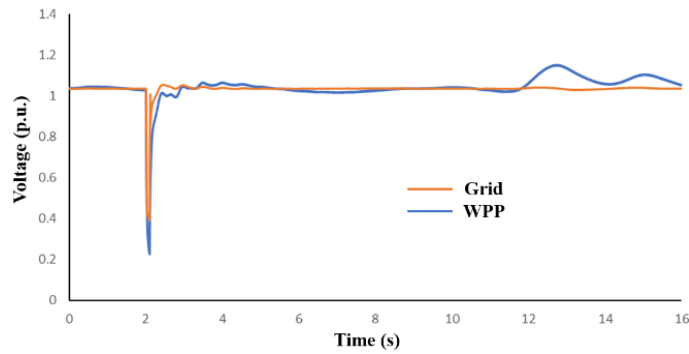
Fig. 5.12(a) Wind speed generated from Turbsim, (b) active power output, (c) reactive power output, (d) voltage output.

In this section, the wind speed data is obtained from the wind gust module in PSCAD. At 2 s, a wind gust is generated, causing the wind speed to increase from 27 m/s to 24 m/s within 1 sec. The performance of the Wind Power Plant (WPP) has been evaluated under this wind gust scenario. Additionally, a three-phase to ground fault with a duration of 0.10 s is introduced at 2 s. The analysis of the output in Fig. 5.13 indicates that the WPP successfully maintains its operation and effectively rides through the fault, demonstrating its resilience and fault-ride through capability.

(a)

(b)

(c)

(d)
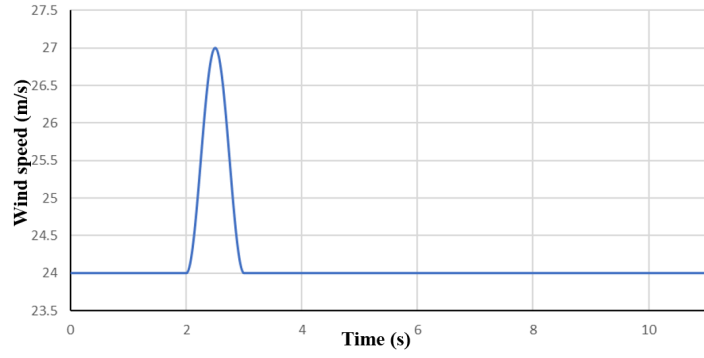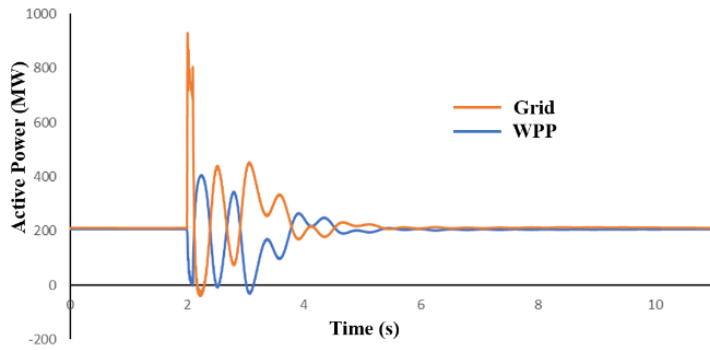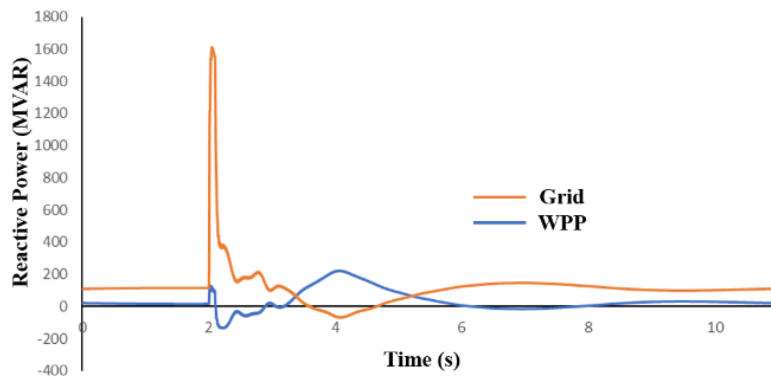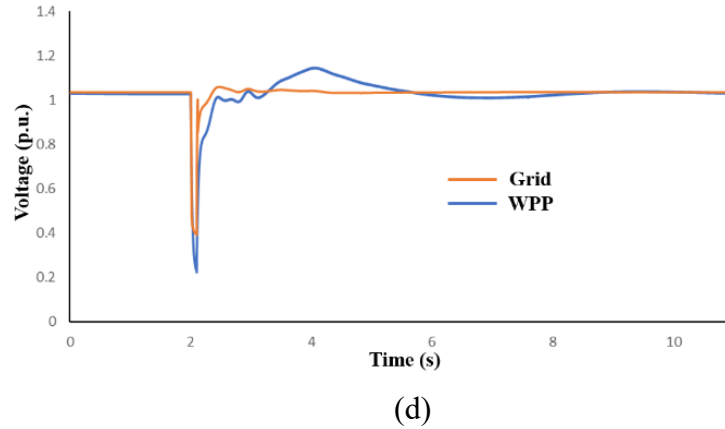
Fig. 5.13(a) Wind speed generated from Wind Gust block in PSCAD, (b) active power output, (c) reactive power output, (d) voltage output.

C. Operation under weak and strong grid conditions

The performance of the BLE system has been evaluated under weak grid conditions. To simulate a weak grid, the reactance of the transmission line has been increased to 0.1H from .005H while keeping the resistance value unchanged. The higher X/R ratio indicates the grid's weakness in terms of its reactance.

In this testing scenario, a three-phase to ground fault is introduced at 2 s and lasts for 0.1 s to assess the fault-ride through capability of the WPP equipped with the BLE system. As a result, some fluctuations are observed in the output of the WPP, indicating the presence of disturbances caused by the fault. However, the overall result indicates that the WPP successfully rides through the fault and continues to operate despite the system's inherent distortion and fluctuations.
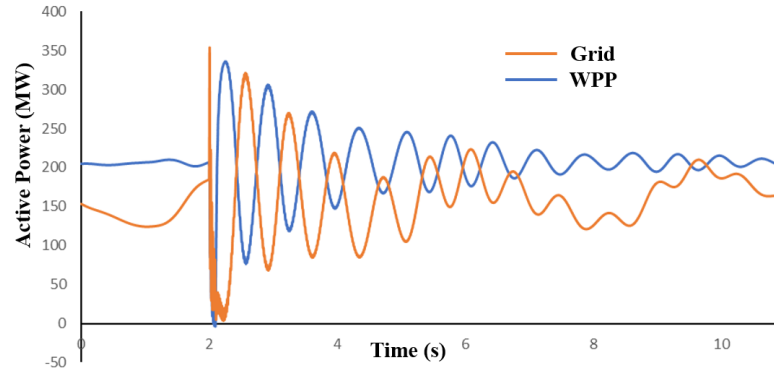
(a)
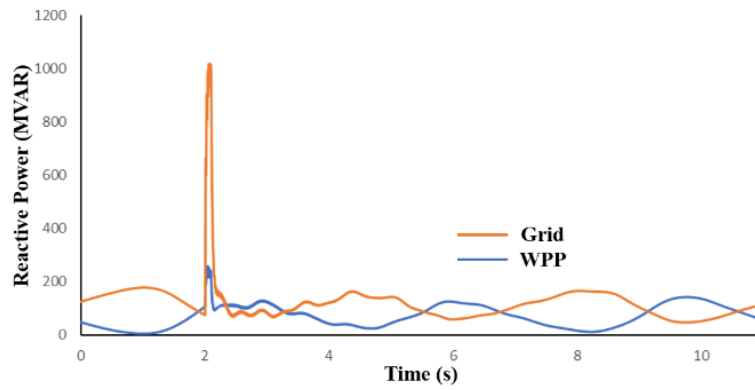
(b)
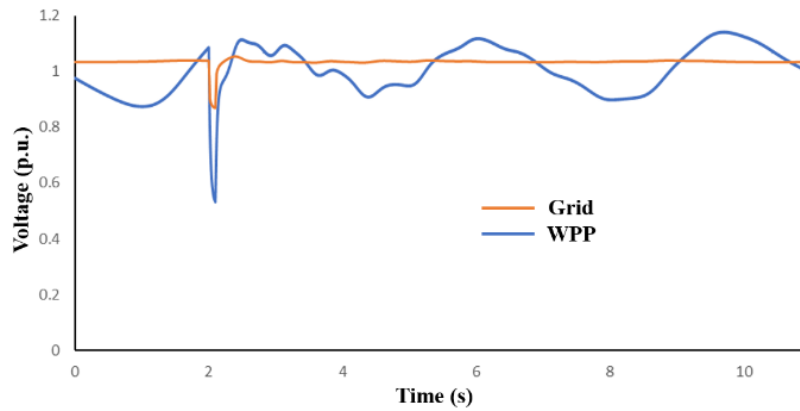
(c)

Fig. 5.15 The output of Grid and WPP during fault and post fault condition. (a) active power output. (b) reactive power output. (c) voltage output.

D. Operation as a synchronous condenser

When the wind speed falls below the cut-in speed, which in this case is 3m/s, the WPP is

unable to generate active power. In this situation, the main clutch is disengaged, and the WPP

operates in a mode similar to that of a synchronous condenser. Instead of producing active power,

the WPP focuses on providing reactive power to the system in order to maintain voltage stability.

Additionally, the WPP can implement a damping provision during this period. This means that it

can contribute to damping oscillations in the system, thereby enhancing stability. By adjusting the

reactive power output, the WPP can help mitigate voltage fluctuations and improve overall system

performance even when it is unable to generate active power due to low wind speeds.
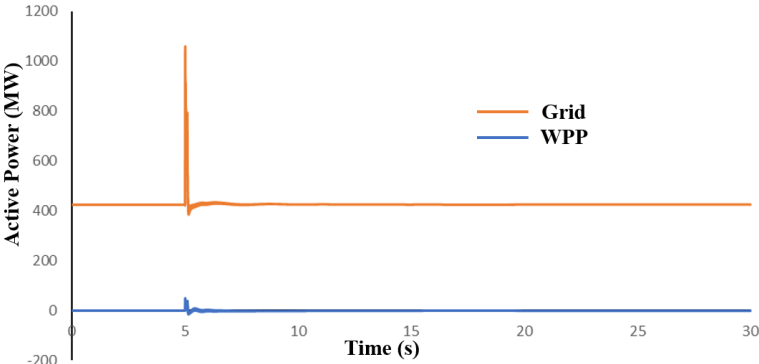
(a)
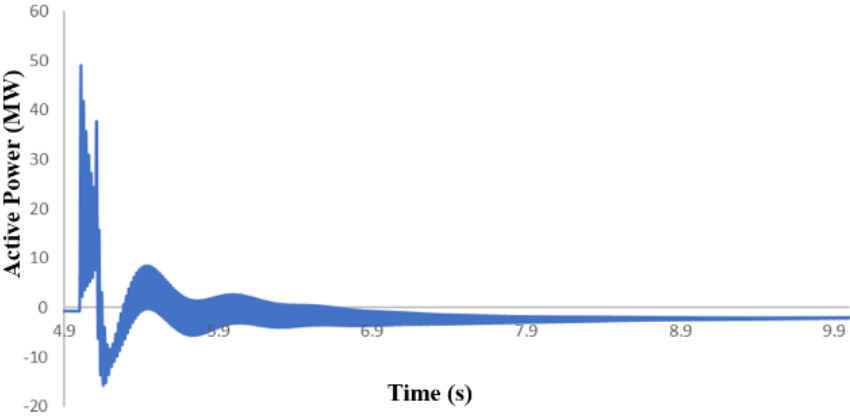
(b)
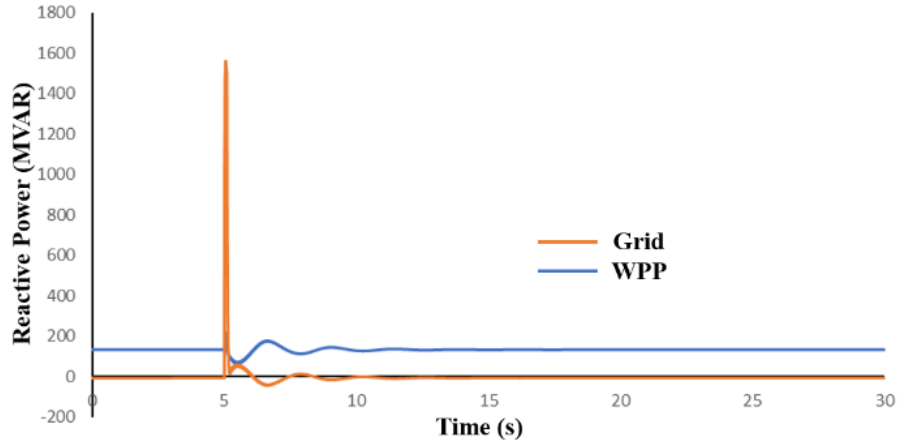
(c)
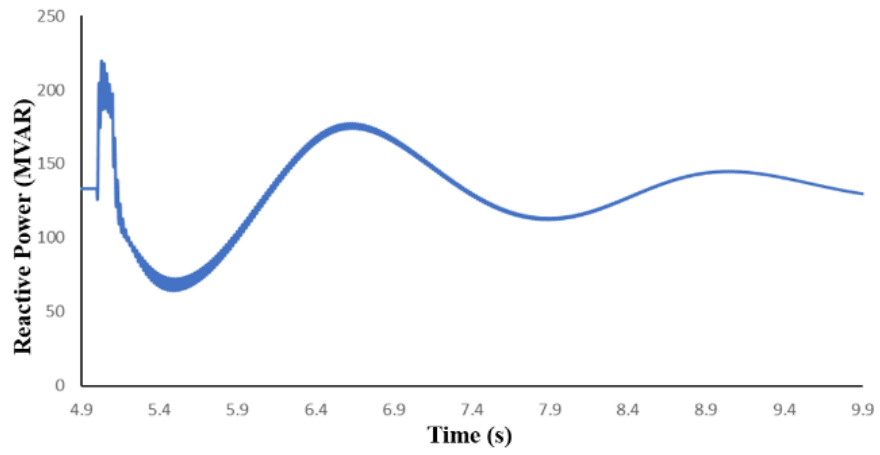
(d)
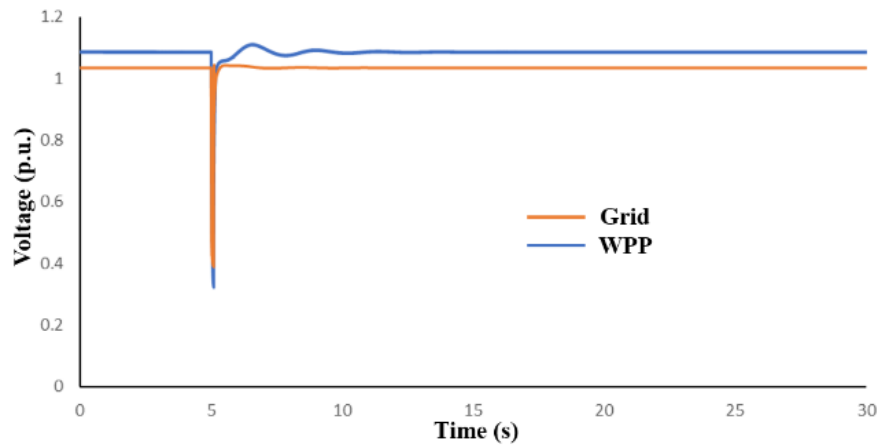
(e)
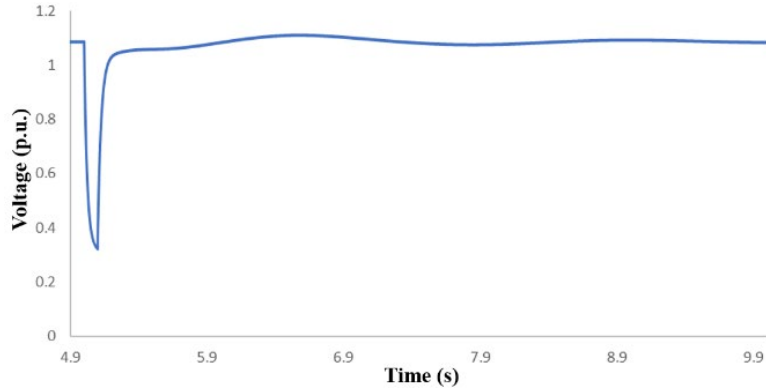
(f)

Fig. 5.16 The output of Grid and WPP during fault and post fault condition, (a) active power output, (b) zoomed in active power output for WPP, (c) reactive power output, (d) zoomed in reactive power output, (e) voltage output, (f) zoomed in voltage output.

5.3.2 Case 2: Type 5 in a Two-area system

A. Inter-area Oscillation

This case study investigates the efficacy of utilizing a large-scale WPP featuring Type 5 WTGs to address interarea oscillations within a two-area electrical system. The system comprises two 2-GW hydro generators, with a 200 MW Type 5 WPP incorporating BLE connected to area 2. The simulation, executed in PSCAD software, intentionally excludes PSSs in the hydro generators. A three-phase to ground fault is introduced at area 1 for 0.15s, providing the context for two primary objectives: firstly, the reduction of power oscillations post-fault clearance through the implementation of WPP controllers, and secondly, the evaluation of BLE's effectiveness in suppressing oscillations induced by the fault event. Additionally, a capacitor bank is deployed in area 2 to maintain voltage at the busbar 3 and optimize the Type 5 WPP's potential for damping oscillations in area 1. This study aims to contribute insights into the practical application of advanced WPP technology and its role in enhancing system stability and resilience in the face of fault events.
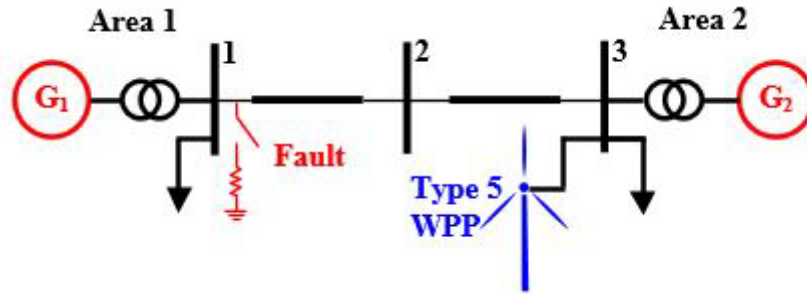
Fig. 5.17 Two-area system with the WPP in the middle of Area 1 and 2.

(a)

(b)

(c)
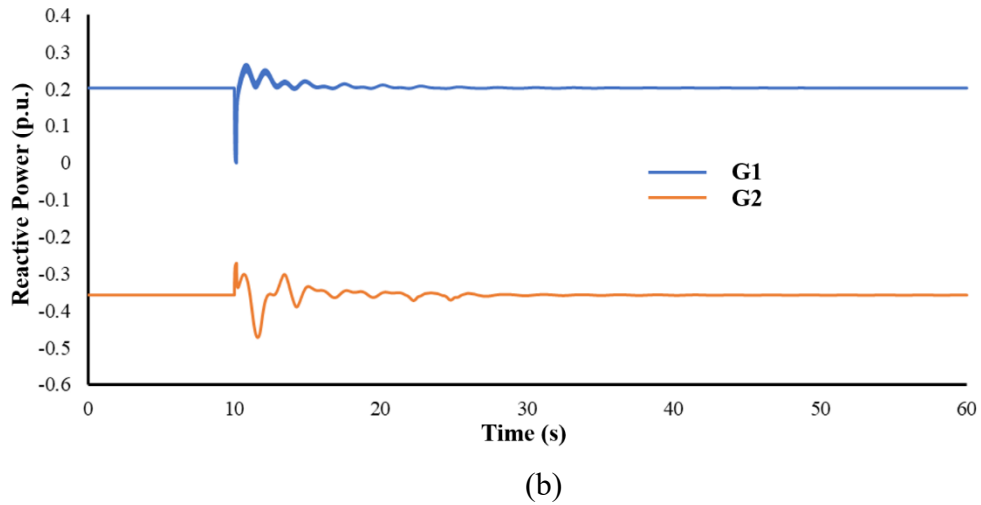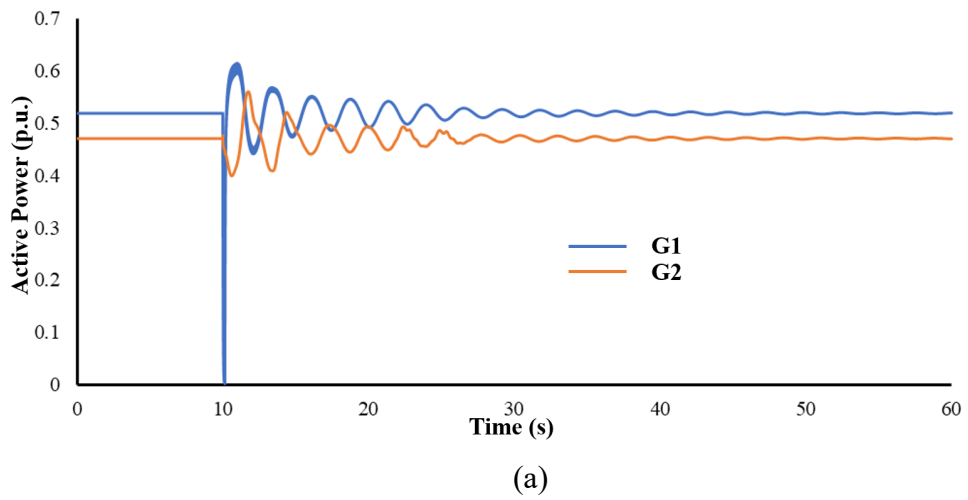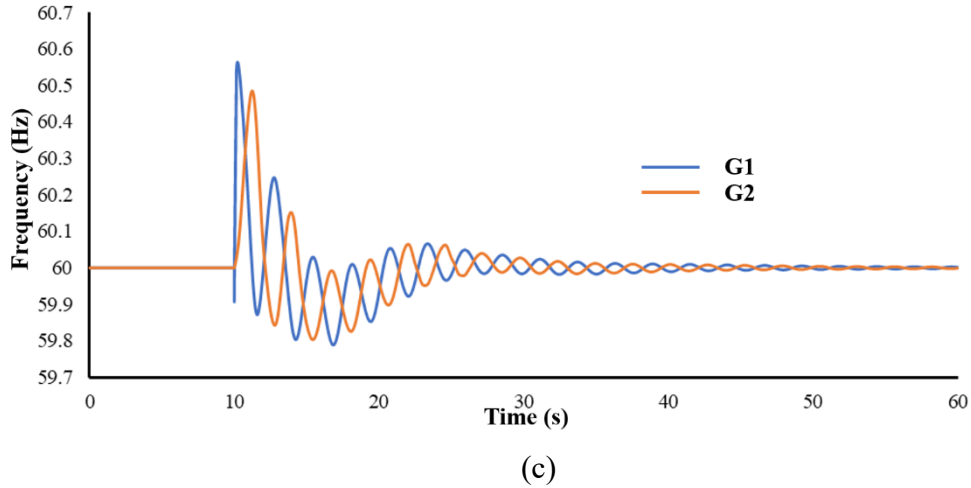
Fig. 5.18 Hydro generators output for area 1 and area 2 during fault and post fault condition. (a) active power output. (b) reactive power output. (c) frequency output.

Fig. 5.18(a) portrays the active power generation profiles of areas 1 and 2, respectively. The oscillation frequency is quantified at 0.3Hz for the interarea oscillation phenomenon. Results of Fig. 5.18 reveal that the oscillatory behavior experiences significant damping within a 30-second timeframe following the fault event. Consequently, we can affirm that the BLE scheme operated with notable efficiency in mitigating the oscillation.

Fig. 5.18(b) delineates the reactive power output characteristics of generators within areas 1 and 2. An observable fluctuation in the reactive power output is evident in both generators due to the fault occurrence. Subsequently, both generators' reactive power output profiles gradually return to their initial states once the oscillatory process subsides.

Fig. 5.18(c) exhibits the frequency profiles at the terminals of the generators in each respective area. In contrast to the power oscillations, the frequency fluctuations also undergo effective damping when subject to the proposed BLE control scheme.
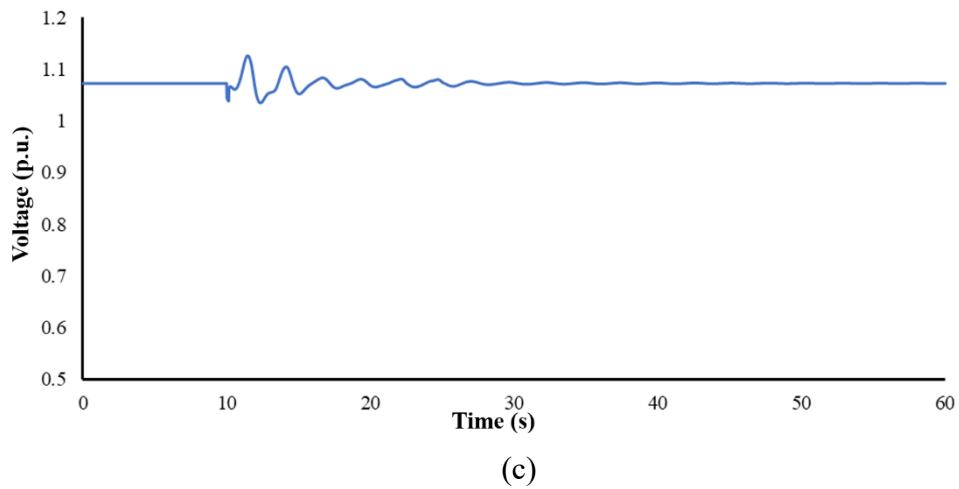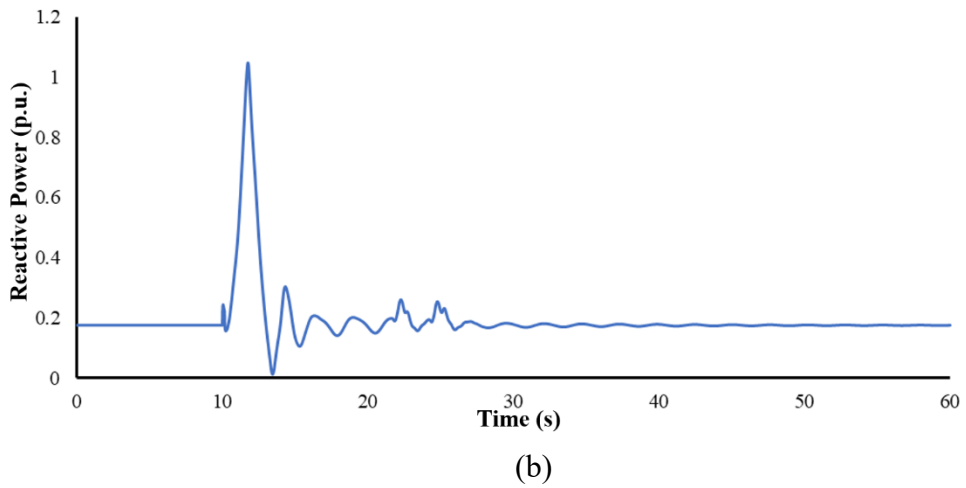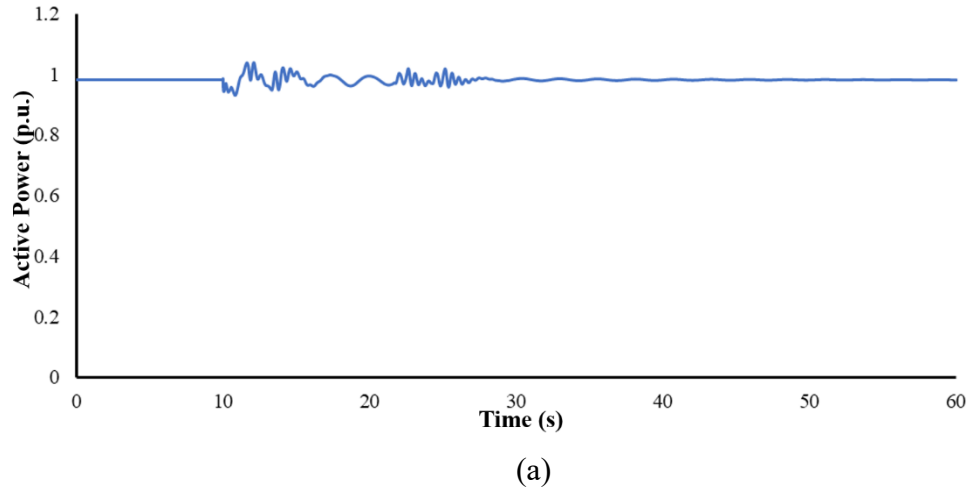
Fig.5.19 Output at the POI from Type 5 WPP during fault and post-fault condition. (a) active power output. (b) reactive power output. (c) voltage.

In Fig. 5.19(a), the Type 5 WPP's active power output effectively contributed to the damping of system oscillations without the need for power curtailment. This damping mechanism leveraged the inertia of the wind turbine. As a result, it can be deduced that the BLE scheme employed in the Type 5 WTG exhibited remarkable efficiency in providing damping in this specific scenario.

Furthermore, as demonstrated in Fig. 5.19(b), the reactive power output played a crucial role in preserving voltage stability within the system both during and after a fault occurrence. The proposed AVR integrated into the BLE's excitation system efficiently maintained voltage stability throughout the fault event, ensuring uninterrupted operation without disconnections or disruptions.

The voltage response depicted in Fig. 5.19(c) exhibits a discernible decline during the fault occurrence. However, aided by the excitation system, the voltage swiftly returned to its initial level. Notably, an elevation in voltage, reaching up to 1.1 p.u., is discerned because of the injection of reactive power from the Type 5 Wind Turbine Generator (WTG). Subsequently, as the oscillatory behavior abated, the voltage reverted to its nominal range.

5.4 Conclusion

This chapter focuses on the theoretical aspect of Automatic Voltage Regulators (AVRs). After a thorough comparison of various types of AVRs, the decision was made to utilize BLE due to its advantages of reduced maintenance and improved safety. A model of the BLE system was developed and implemented in the PSCAD software. The model was then tested using a Type 5 WPP provided by NREL, encompassing a range of scenarios to evaluate the inherent capabilities of the Type 5 machine.

During testing, the PSCAD model demonstrated the ability to ride through faults under

normal operating conditions. Furthermore, the performance of the BLE system was evaluated under different wind conditions, all of which yielded promising results in terms of fault ride-through. The BLE system was also tested under weak and strong grid conditions, resulting in some power and voltage fluctuations at the WPP output. However, the BLE system effectively dampened the oscillations, ensuring stable operation. It is also tested on a two-area model and performed efficiently.

Additionally, the performance of the BLE system was assessed in its role as a synchronous condenser. The reactive power output of the WPP provided valuable support for system stability. Moving forward, further testing of the BLE system will be conducted at NREL using the Controllable Grid Interface (CGI), enabling a comprehensive understanding of the effectiveness of BLE in real-life scenarios.

In Chapter 6, an additional layer of analysis will be introduced through Prony, a sophisticated tool for signal processing. Prony will be instrumental in dissecting the output signals, extracting valuable insights into the exponential sinusoids present. This innovative use of Prony in Chapter 6 is poised to facilitate a more in-depth comparison with other schemes proposed in the preceding chapters, enriching our comprehension of the BLE system's performance in the realm of power system oscillation damping.

Chapter 6
Prony Analysis

Prony analysis stands out as an innovative method in the domain of power system engineering, representing a significant advancement beyond traditional Fourier analysis. Its unique capability to directly estimate the frequency, damping, strength, and relative phase of modal components within a signal position it as a valuable tool for extracting crucial information from transient stability program (TSP) simulations and large-scale system tests or disturbances. In the context of power system oscillation damping, Prony analysis becomes particularly noteworthy for its potential contributions to TSP output analysis. This method holds the promise of offering parametric summaries for damping studies, facilitating data compression and simplification of complex datasets. Moreover, it provides quantified information that is instrumental in adjusting remedial controls, enabling sensitivity analysis and thorough performance evaluation. Prony analysis not only enhances our understanding of power system dynamics by offering insight into modal interaction mechanisms through modal analysis but also contributes to practical efficiency by reducing simulation times for damping evaluation, thereby enhancing predictive capabilities in power system stability assessment.

The technique employed in this study, based on Prony's method, utilizes an exponential parameter estimation approach. This method involves fitting a linear combination of exponential terms to a uniformly sampled signal, allowing for the extraction of four essential parameters for each mode within the signal: amplitude, phase, frequency, and exponential damping [87]. Originally developed by Baron de Prony in the 1790s, this approach was computationally intensive and remained dormant until the era of modern, fast, and efficient computers. Subsequently, it has

become a practical and widely employed tool in modern spectrum analysis [88]. Notably, it is only in the last two decades that Prony's method has found practical application in power system contexts, particularly in extracting modal information from transient stability programs and system field tests [87]. Its unique capability to extract modal damping coefficients gives it an advantage over Fourier analysis, making it particularly suitable for analyzing electromechanical oscillations characterized by exponentially decreasing (or increasing) waveforms.

6.1 Prony's Method Description

Consider y(t) as the function derived from the signals measured in the simulation of the two-area system. Let y(k) represent the measured signal for y(t), composed of N equally spaced samples at intervals K = 0, 1, 2, …, N-1. Prony's method aims to characterize the nature of the measured signals by aligning a comparable structure with the recorded output.

$$\hat{y}(t) = \sum_{i=1}^{p} B_i e^{\lambda_i t} \tag{6.1}$$

This exponential structure, which can also be presented as a sum of exponentially damped sinusoids shown in (6.2), is thus suitable to estimate the individual properties like frequencies and dampings of modes in the active power output of the SGs connected in area 1 and area 2 shown in the previous chapters.

$$\hat{y}(t) = \sum_{i=1}^{Q} A_i e^{\sigma_i t} \cos(2\pi f_i t + \phi_i) \tag{6.2}$$

In (6.2) A_i, σ_i, f_i, φ_i are the amplitude, exponential damping, frequency and phase values of the ith modal component.

The discrete-time version $\hat{y}(k)$ and $\hat{y}(t)$ can be written in a convenient form as shown in (6.3).

$$\hat{y}(k) = \sum_{i=1}^{P} B_i z_i^k \tag{6.3}$$

In (6.3), z_i is the exponential part of the modal component as shown in (6.4).

$$z_i = e^{\lambda_i \Delta t} \tag{6.4}$$

Expanding (3.7) for sample instants k=0,1,2... N-1 gives (6.5). $y(0) = B_1 + B_2 + B_3 + \cdots + B_n$

$$y(1) = B_1 z_1 + B_2 z_2 + B_3 z_3 + \cdots + B_n z_n \tag{6.5}$$

$$y(2) = B_1 z_1^2 + B_2 z_2^2 + B_3 z_3^2 + \cdots + B_n z_n^2$$

$$\ldots$$

$$y(N-1) = B_1 z_1^{N-1} + B_2 z_2^{N-1} + B_3 z_3^{N-1} + \cdots + B_n z_n^{N-1}$$

Rewriting (6.5) in matrix form gives (6.6).

$$\begin{bmatrix} y(0) \\ y(1) \\ \vdots \\ y(N-1) \end{bmatrix} = \begin{bmatrix} B_1 z_1^0 + \cdots + B_n z_n^0 \\ B_1 z_1^1 + \cdots + B_n z_n^1 \\ \vdots \\ B_1 z_1^{N-1} + \cdots + B_n z_n^{N-1} \end{bmatrix} = \begin{bmatrix} z_1^0 & z_2^0 & \cdots & z_n^0 \\ z_1^1 & z_2^1 & & z_n^1 \\ \vdots & & \ddots & \vdots \\ z_1^{N-1} & z_2^{N-1} & \cdots & z_n^{N-1} \end{bmatrix} \begin{bmatrix} B_1 \\ B_2 \\ \vdots \\ B_n \end{bmatrix} \tag{6.6}$$

$$[Y] = [Z]\,[B] \tag{6.7}$$

In (6.7), Y, B and Z represent matrices as shown in (6.8).

$$Y = \begin{bmatrix} y(0) \\ y(1) \\ \vdots \\ y(N-1) \end{bmatrix}, B = \begin{bmatrix} B_1 \\ B_2 \\ \vdots \\ B_n \end{bmatrix}, Z = \begin{bmatrix} z_1^0 & z_2^0 & \cdots & z_n^0 \\ z_1^1 & z_2^1 & & z_n^1 \\ \vdots & \vdots & \ddots & \vdots \\ z_1^{N-1} & z_2^{N-1} & \cdots & z_n^{N-1} \end{bmatrix} \tag{6.8}$$

The procedure for Prony's method formulated in linear prediction theory to solve the linear equations (6.6) for B_i's and z_i's can be summarized in the following steps [10]:

(1) Build a linear prediction model (LPM) for $y(k)$ where the nth sample is a function of n past samples and unknown prediction coefficients {α1, α2, ...αn}

$$y(n) = \alpha_1 y(n-1) + \alpha_2 y(n-2) + \cdots + \alpha_n y(0) \tag{6.9}$$

Apply this model for all successive samples as shown in (6.10)

$$y(n + 1) = \alpha_1 y(n) + \alpha_2 y(n - 1) + \cdots + \alpha_n y(1)$$

$$\cdots \qquad (6.10)$$

$$y(N - 1) = \alpha_1 y(N - 2) + \alpha_2 y(N - 3) + \cdots + \alpha_n y(N - n - 1)$$

Rearranging (6.10) in matrix form gives (6.11)

$$\begin{bmatrix} y(n-1) & y(n-2) & \cdots & y(0) \\ y(n-0) & y(n-1) & \cdots & y(1) \\ y(n+1) & y(n-0) & \cdots & y(2) \\ \vdots & \vdots & \ddots & \vdots \\ y(N-2) & y(N-3) & \cdots & y(N-n-1) \end{bmatrix} \begin{bmatrix} \alpha_1 \\ \alpha_2 \\ \vdots \\ \alpha_n \end{bmatrix} = \begin{bmatrix} y(n+0) \\ y(n+1) \\ y(n+2) \\ \vdots \\ y(N-1) \end{bmatrix} \qquad (6.11)$$

(2)   Solve the LPM shown in (6.11) to find the predictor coefficients $\{\alpha 1, \alpha 2, \ldots \alpha n\}$.

The α's in the linear equations shown in (6.11) can be solved directly if N=2n or by the method of least squares if N>2n

(3)   Construct the LPM's associated characteristic polynomial P(z) using the predictor coefficients as shown in (6.11)

$$P(z) = z^n + \alpha_1 z^{n-1} + \alpha_2 z^{n-2} + \cdots + \alpha_n \qquad (6.11)$$

(4) Determine the roots of the polynomial P(z). These roots are the required complex frequencies z_i .

(5) Substitute z_i and $y(k)$ in (6.6) and solve the resulting linear equations by using the least squares method to determine B_i.

(6) Substitute z_i in (6.4) to find λ_i.

Important Parameters regarding Prony Analysis

Drawing from the experiences with Prony's method, a set of general guidelines has been devised for parameter configuration, primarily tailored for extracting power system torsional modal information. It is noteworthy that guidelines for real signal measurements deviate slightly

from those pertaining to transient stability program (TSP) output signals, owing to the presence of measurement noise and other nonlinearities in actual signal measurements.

The modal order parameter (numModes) necessitates careful consideration, given the inherent noise and nonlinearities in real signal measurements. To address this, opting for a larger numModes is recommended; however, determining the precise value is challenging in a single step. Typically, an iterative approach is employed, where the user sets the numModes parameter and executes Prony's method. The output modes are then utilized to reconstruct the signal, and if the fit is unsatisfactory, the numModes parameter is increased incrementally until a suitable fit for TSP output signals or a reasonably good fit for real measurement signals is achieved.

In selecting window location and size parameters, for TSP output records, a later window position is suggested due to the slower decay of torsional modes in comparison to shorter duration modes. Conversely, for real measurement records, an earlier window position is advisable, especially as the record length increases, increasing the likelihood of non-linear phenomena distorting the linearity of the overall signal. The window size is recommended to include at least two cycles of the lowest modal frequency in most cases.

The sampling rate parameter provides an avenue for adjusting numModes and total record length. Ensuring a sampling rate with at least four samples per cycle, aligned with the Nyquist criteria, is essential. While increasing the sampling rate parameter can enhance fit quality, excessive increments should be avoided, as the matrices involved in Prony's analysis tend to become singular, leading to inaccurate results.

In conclusion, the process of parameter selection for Prony's method is intricate, demanding careful consideration of numerous parameters that directly influence results and accuracy. Unlike Fourier analysis, each data record must be approached individually. While there

are empirical rules, user training and practice are essential for achieving reliable results. The pivotal parameter, numModes, is crucial not only for fitting signal modes but also for accommodating any noise or non-linearities present in the signal.

6.2 Prony analysis for the POD schemes

A Prony analysis Matlab code has been devised to discern the exponential sinusoids embedded in the simulation data derived from various Power Oscillation Damping (POD) approaches delineated in preceding chapters. In the context of Dual POD, where both active power and reactive power loops contribute to power oscillation damping within the system, identifying the damping components becomes intricate. Establishing a baseline for comparing damping outputs from the PV plant or WPP is challenging due to the dual contributions.

To overcome this challenge, the active power output from area 1 is selected as the signal for analysis, providing a basis for comparing the damping effects across different studies conducted in prior chapters. In the subsequent section, our focus shifts towards extracting the exponential sinusoids from the active power output of area 1. Given that a three-phase fault occurred in area 1 and damping was facilitated by area 2, considering the worst-case scenario wherein the oscillations in one area are dampened by another through PODs and excitation systems serves as a robust benchmark. Analyzing area 1's active power signals in the aftermath of such an event allows for an insightful assessment of the impact exerted by area 2 on area 1's active power dynamics. In our Prony analysis, we focused on reproducing the graph of active power output from area 1 seen in earlier chapters. To simplify comparisons among different schemes, we consistently chose 14 modes. The selection window for each simulation was determined from the end of the fault until the point of achieving the mean after damping or when the oscillation ended. We adjusted the sampling rate to create the desired plot from the collected data while ensuring a

minimum of four samples in each cycle.

A. *Prony Analysis on PV plant*

The exclusive focus of the Prony analysis was directed towards the scenario involving the implementation of Dual Power Oscillation Damping (POD). This choice was deliberate, as the Dual POD scheme exhibited the most rapid damping of oscillations. Consequently, the analysis concentrated on extracting and scrutinizing the active power output from area 1 in this particular context.
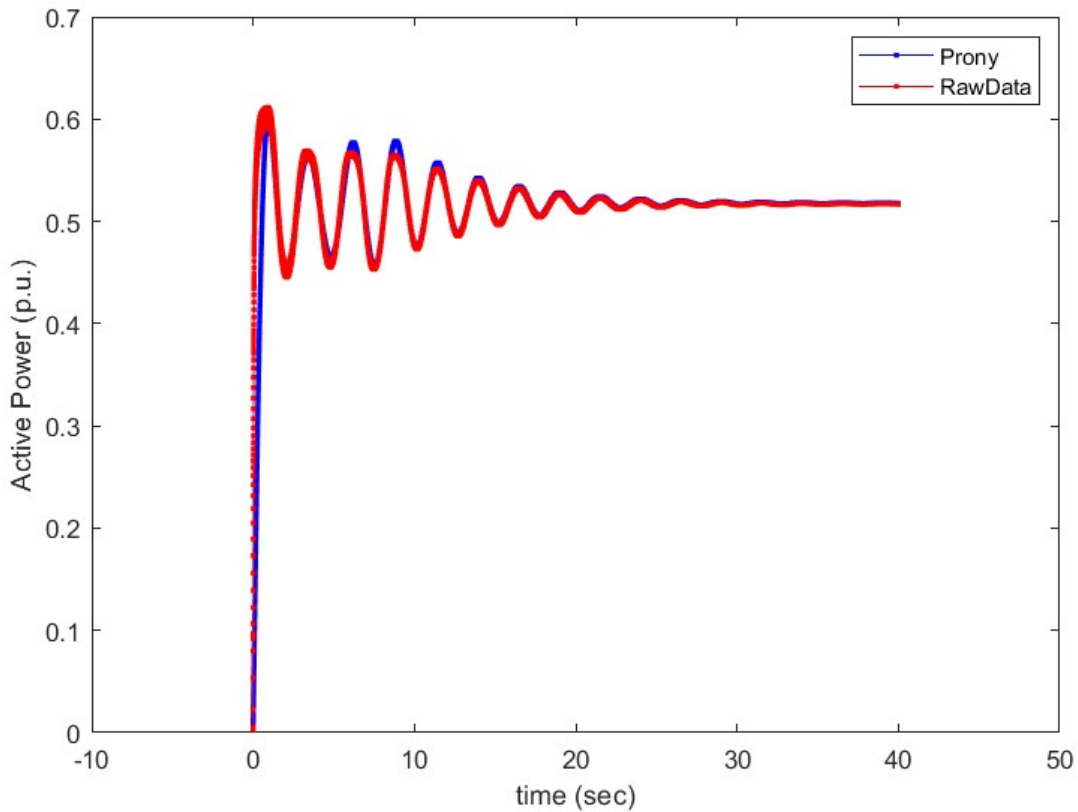
Fig. 6.1 A comparison of the Prony graph and the simulation data from Dual POD of PV

Fig. 6.1 presents a comparison between the simulation data obtained from Chapter 2 and the corresponding Prony graph. As the graph originates from simulated data and not from real-time phase measurements using a Phase Measurement Unit (PMU), it exhibits minimal noise. This

characteristic allows a small number of modes to furnish the necessary data. The output from Prony's analysis appears in a random order, making it challenging to discern genuine modes from noise. To address this issue, a separate sorting algorithm is essential. Various sorting algorithms can be employed based on parameters like magnitude, frequency, or exponential decay. However, each approach has its inherent limitations. In this scenario, the focus has been on considering the top three exponential components for analysis and interpretation.

TABLE 6.1

MODE, MAGNITUDE, DECAY, FREQUENCY AND PHASE ANGLE

Mode#	Magnitude	Decay	f(Hz)	phi
1	0.4081	-0.5339	0.324	2.4823
2	0.2765	-0.5186	0.0319	2.4299
3	0.0664	-0.4061	0.2679	2.6995

B. *Prony analysis on WPP*

Fi. 6.2 illustrates a comparison between the actual data obtained from the dual Power Oscillation Damper (POD) simulation in Chapter 3 and the corresponding Prony graph. Similar to the case of the PV plant data in Chapter 2, the graph stemming from the Wind Power Plant (WPP) simulation lacks significant noise, as it is not derived from real-time Phase Measurement Unit (PMU) measurements. This characteristic enables the extraction of the required information with a minimal number of modes. The Prony analysis output is unordered, posing a challenge in distinguishing true modes from noise. To overcome this challenge, a distinct sorting algorithm is employed. Various sorting algorithms, based on parameters such as magnitude, frequency, or exponential decay, can be considered, each with its own set of limitations. In this context, the

analysis has focused on the top three exponential components for meaningful interpretation and comparison.
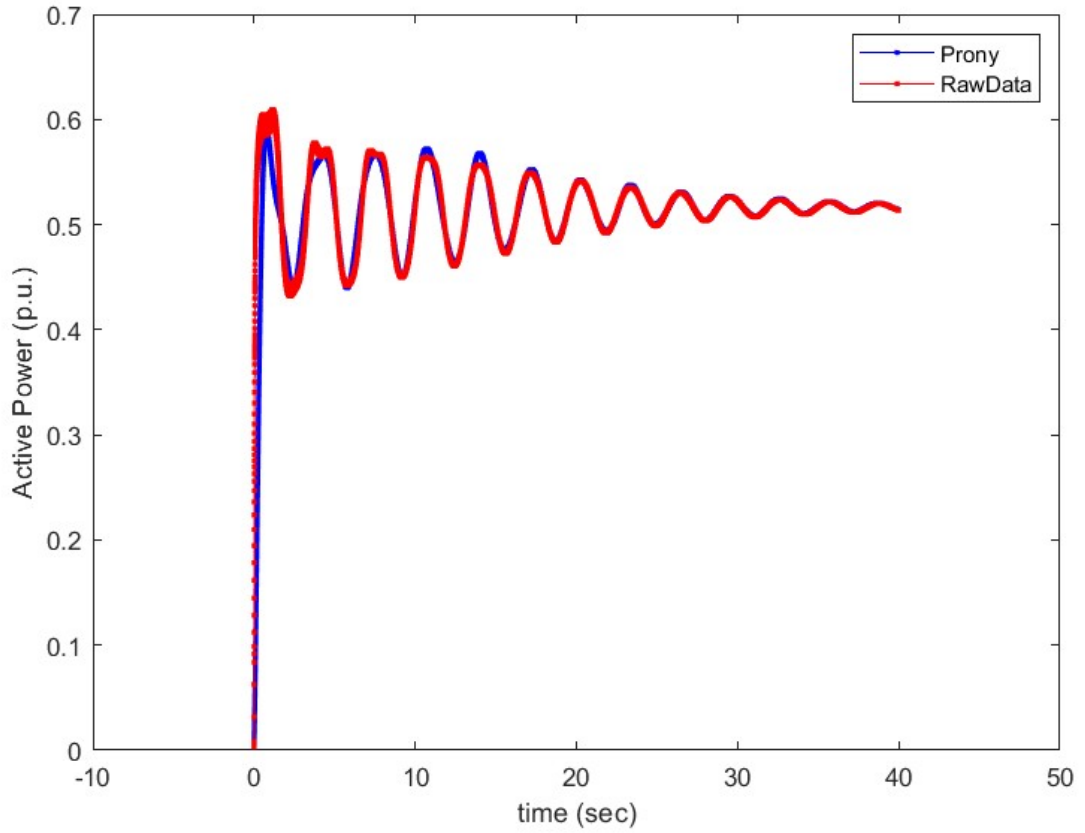
Fig. 6.2 A comparison of the Prony graph and the simulation data from Dual POD of WPP

TABLE 6.2

MODE, MAGNITUDE, DECAY, FREQUENCY AND PHASE ANGLE

Mode#	Magnitude	Decay	f(Hz)	phi
1	0.2501	-0.3194	0.2766	1.4546
2	0.0137	-0.1846	0.2169	0.1171
3	0.5728	-0.1783	0.3213	1.718

C. Prony analysis on coordinated PV and WPP

In this context, both the Wind Power Plant (WPP) and Photovoltaic (PV) plant operate in coordination. In Case 3, the PV plant functions in dual Power Oscillation Damper (POD) mode, while the WPP supplies reactive power. Conversely, in Case 4, the WPP operates in dual mode, and the PV plant provides reactive power based on the time of day. Figure 6.3 illustrates the comparison between actual data and Prony analysis results for Case 3, while Figure 6.4 does the same for Case 4. The simulated data from both plants, obtained from Chapter 4, features minimal noise compared to real-time Phase Measurement Unit (PMU) measurements, enabling effective analysis with a reduced number of modes. Similar to the PV and WPP scenarios discussed earlier, the Prony analysis outputs are unordered, necessitating the application of a sorting algorithm. For this purpose, the focus has been on considering the top three exponential components. Tables 6.3 and 6.4 present the extracted modes for Case 3 and Case 4, respectively, incorporating data from the synchronous generator in area 1.
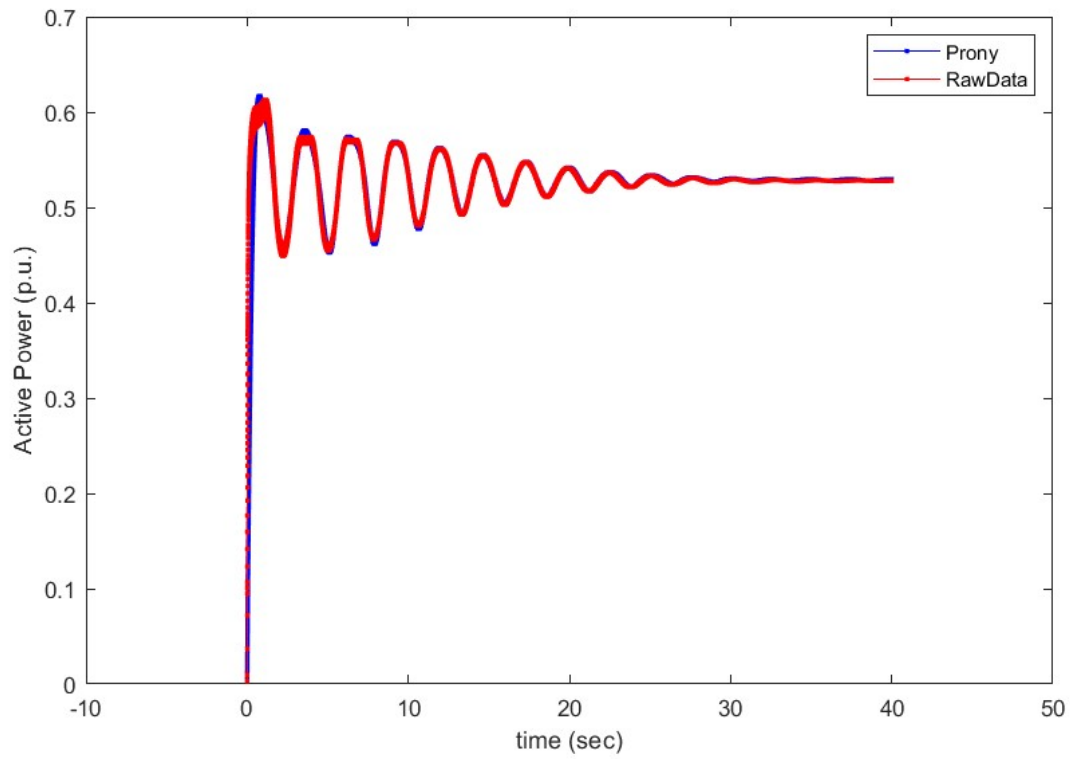
Fig. 6.3 A comparison of the Prony graph and the simulation data of Case 3 from Chapter 4

Table 6.3

MODE, MAGNITUDE, DECAY, FREQUENCY AND PHASE ANGLE

Mode#	Magnitude	Decay	f(Hz)	phi
1	0.0235	-0.3835	0.0712	0.5856
2	0.0548	-0.2962	0.3053	1.5453
3	0.0404	-0.2438	0.6892	0.6732
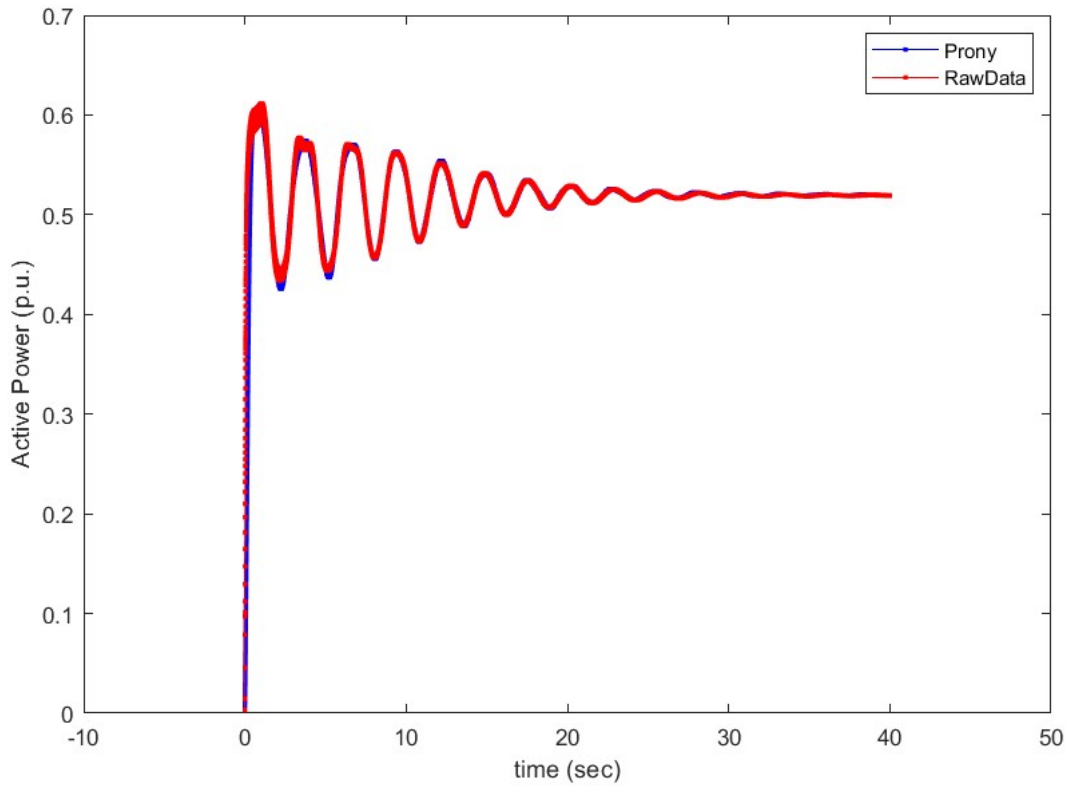
Fig. 6.4 A comparison of the Prony graph and the simulation data of Case 4 from Chapter 4

TABLE 6.4

MODE, MAGNITUDE, DECAY, FREQUENCY AND PHASE ANGLE

Mode#	Magnitude	Decay	f(Hz)	phi
1	0.2854	-0.6325	0.3061	2.4112
2	0.0356	-0.3182	0.657	1.2206
3	0.4398	-0.2778	0.3544	1.3925

D. Prony analysis on Type 5 WPP

Prony analysis has been performed on the Type 5 Wind Power Plant (WPP) data obtained in Chapter 5. Fi. 6.5 and Table 6.5 present the corresponding data, allowing for a comprehensive

comparison and evaluation of the Prony analysis results for the Type 5 WPP.
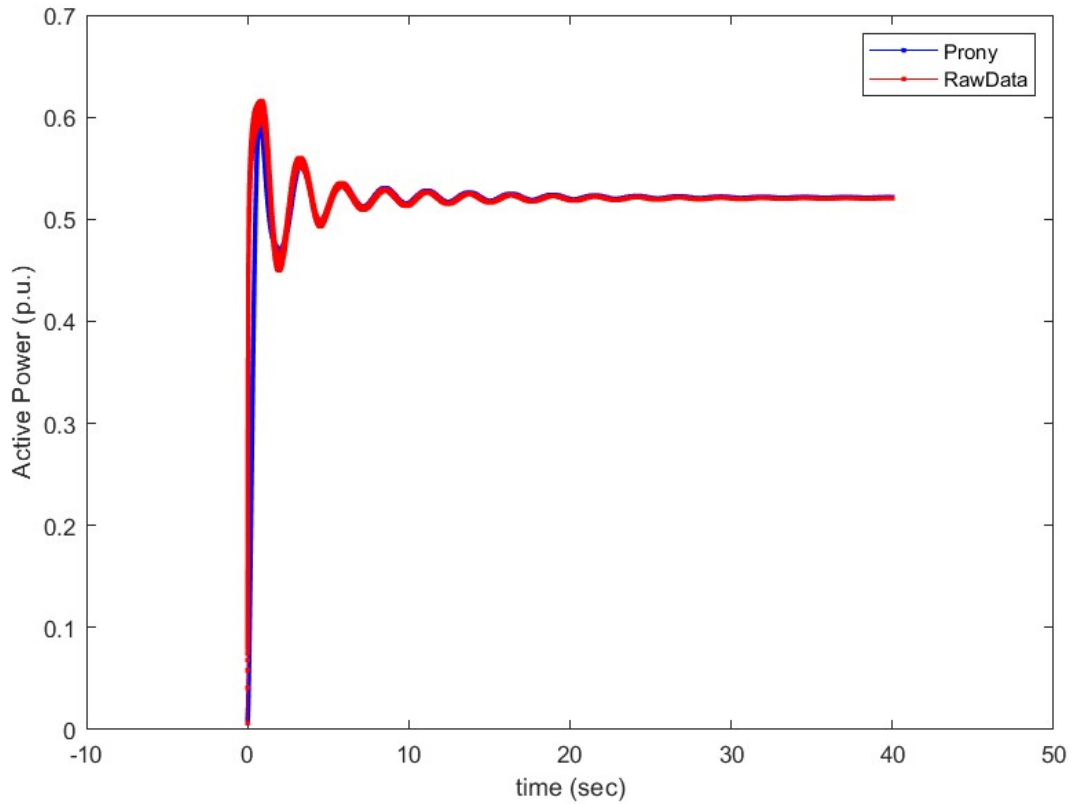
Fig. 6.5 A comparison of the Prony graph and the simulation data of Type 5 WPP

TABLE 6.5

MODE, MAGNITUDE, DECAY, FREQUENCY AND PHASE ANGLE

Mode#	Magnitude	Decay	f(Hz)	phi
1	0.2535	-0.7264	0.4541	2.5921
2	0.0055	-0.4861	0.1678	2.3818
3	0.0054	-0.4059	0.5238	2.6779

6.3 Conclusion

In conclusion, Chapter 6 provides valuable insights into the Prony analysis conducted on

the Type 5 Wind Power Plant (WPP) data from Chapter 5. The analysis reveals that the Prony results for the Type 5 WPP exhibit the highest magnitude in the exponential components. This signifies the effectiveness of the Type 5 WPP in providing substantial damping to power system oscillations.

Furthermore, the comparison between the Dual Power Oscillation Damper (POD) and the normal Dual POD in Chapter 6 demonstrates that the Dual POD with additional reactive power damping by the Reactive POD yields superior exponential components. The incorporation of reactive power modulation enhances the damping capabilities of the system, resulting in more pronounced and effective exponential components.

The Prony analysis, a sophisticated technique used to decompose signals into exponential components, plays a crucial role in extracting meaningful information from the simulated data. By considering the top three exponential components, as detailed in Tables 6.3, 6.4, and 6.5, the analysis focuses on the most significant modes contributing to the system response. The careful selection of the analysis parameters, such as the number of modes and the sampling rate, ensures accurate representation and comparison of the exponential components.

In summary, the Prony analysis conducted on the Type 5 WPP data affirms its exceptional damping characteristics, showcasing the prominence of certain exponential components and average damping ratio (ζ) of 0.27. Additionally, the investigation into Dual POD schemes emphasizes the advantage of incorporating reactive power damping, leading to enhanced damping performance and more pronounced exponential components. These findings contribute to a deeper understanding of the power oscillation damping capabilities of Type 5 WPPs and the effectiveness of specific control strategies in improving system stability.

Chapter 7
Conclusion

In concluding this PhD thesis, the extensive investigation conducted across various chapters underscores the pivotal role of Type 5 Wind Power Plants (WPPs) in power system stability. The inherent characteristics of Type 5, marked by greater inertia and enhanced current capabilities, position it as a frontrunner in providing superior damping compared to other resources. The dissertation's primary innovation, Power Oscillation Damping (POD), emerges as a transformative element, with the Dual POD scheme showcasing remarkable efficiency in swiftly reducing inter-area oscillations in utility-scale Photovoltaic (PV) plants, as demonstrated in Chapter 2.

The exploration extends to Wind Power Plants (WPP) in Chapter 3, where the Dual POD scheme proves highly effective in mitigating low-frequency oscillations. Chapter 4 introduces a coordinated control scheme that involves both PV and WPP, unveiling improved damping performance through synchronized operations. The theoretical model of Automatic Voltage Regulators (AVRs) for Type 5 synchronous generators in WPPs, discussed in Chapter 5, emphasizes the benefits of Brushless Excitation (BLE) systems in maintaining stable operation across diverse conditions.

The conclusive Chapter 6 synthesizes findings from Prony analysis, underscoring the superior damping characteristics of Type 5 WPPs, particularly evident in pronounced exponential components. Notably, the exploration of Dual POD schemes highlights their enhanced effectiveness, especially when incorporating reactive power damping.

In summary, this research significantly contributes to advancing the field of power system stability and renewable energy integration. The insights gained not only affirm the efficacy of

specific damping strategies in PV and WPP systems but also underscore the critical importance of innovative control schemes and the role of reactive power modulation in enhancing overall system performance. These findings are instrumental in shaping resilient and stable renewable energy systems in the dynamic landscape of power generation.

Bibliography

1. Solar Power Europe, "Global market outlook for solar power 2022-2026," Solar Power Europe, Brussels, Belgium, Tech. Rep., May 2022. [Online]. Available: Global Market Outlook for Solar Power. [Online]. Available: https://solarpowereurope.org

2. U.S. Energy Information Administration, "Annual Energy Outlook 2021," U.S. Department of Energy, Washington, DC, USA, Tech. Rep., Feb. 2021. [Online]. Available: https://www.eia.gov/pressroom/presentations/AEO2021_Release_Presentation.pdf

3. Global Wind Energy Council (GWEC), "Global Wind Energy Outlook 2014," October 2014. [Online]. Available: https://gwec.net/wpcontent/uploads/2015/03/GWEC_Global_Wind_2014_Report_LR.pdf

4. ERCOT, "ERCOT Fact Sheet," [Online]. Available: https://www.ercot.com/files/docs/2020/11/10/ERCOT_Fact_Sheet_11.10.20.pdf (accessed Dec. 16, 2020).

5. "Fast Facts: An Overview of the SPP System," [Online]. Available: https://www.spp.org/about-us/fast-facts/ (accessed).

6. "SPP sets wind and renewable penetration records," ed. 2017.

7. "Global-electricity-review-2022," [Online]. Available: https://ember-climate.org/insights/research/global-electricity-review-2022/

8. E. Rodrigues, A. Bizuayehu, and J.P. Catalao, "Analysis of requirements in insular grid codes for large-scale integration of renewable generation" IEEE PES T&D Conference and Exposition, Chicago, USA, 2014, pp. 1–5.

9. T. Aziz, T. K. Saha, and N. Mithulananthan, "A review of interconnection rules for large-scale renewable power generation," Large Scale Renewable Power Generation: Springer, pp. 151–171, 2014.

10. T. Alquthami, H. Ravindra, M. O. Faruque, M. Steurer and T. Baldwin, "Study of photovoltaic integration impact on system stability using custom model of PV arrays integrated with PSS/E," North American Power Symposium 2010, Arlington, TX, 2010, pp. 1–8.

11. N. W. Miller, M. Shao, S. Venkataraman, C. Loutan and M. Rothleder, "Frequency response of California and WECC under high wind and solar conditions," IEEE Power and Energy Society General Meeting, San Diego, USA, 2012, pp. 1-8,

12.   E. Kabir, P. Kumar, S. Kumar, and A. A. Adelodun, K. -H. Kim, "Solar energy: potential and future prospects," Renewable and Sustainable Energy Reviews, vol. 82, pp. 894–900, Feb. 2018.

13.   R. Yan, N. -Masood, T. Kumar Saha, F. Bai and H. Gu, "The Anatomy of the 2016 South Australia Blackout: A Catastrophic Event in a High Renewable Network," IEEE Trans. Power Syst., vol. 33, no. 5, pp. 5374–5388, Sept. 2018.

14.   A. Safayet, P. Fajri, and I. Husain, "Reactive power management for overvoltage prevention at high pv penetration in a low-voltage distribution system," IEEE Trans. Ind. Appl., vol. 53, no. 6, pp. 5786– 5794, Nov. 2017.

15.   Q. A. Al-Shetwi, M. Z. Sujod, and F. Blaabjerg, "Low voltage ride-through capability control for single-stage inverter-based grid-connected photovoltaic power plant," Solar Energy, vol. 159, pp. 665–681, Nov. 2018.

16.   M. Deakin and M. McCulloch, "Voltage regulation of large scale PV: A comparative case study," IEEE Manchester Powertech, Manchester, UK, 2017, pp. 1–6.

17.   J. L. Domínguez-García, D. J. Rogers, C. E. Ugalde-Loo, J. Liang, O. Gomis-Bellmunt, "Effect of non-standard operating frequencies on the economic cost of offshore AC networks," Renewable Energy, vol. 44, pp. 267–280, Aug. 2012.

18.   O. Gomis-Bellmunt, A. Junyent-FerrÉ, A. Sumper and J. Bergas-JanÉ, "Ride-Through Control of a Doubly Fed Induction Generator Under Unbalanced Voltage Sags," in IEEE Trans. Ener. Conv., vol. 23, no. 4, pp. 1036-1045, Dec. 2008.

19.   A. Sumper, O. Gomis-Bellmunt, A. Sudria-Andreu, R. Villafafila-Robles and J. Rull-Duran, "Response of Fixed Speed Wind Turbines to System Frequency Disturbances," IEEE Trans. Power Syst., vol. 24, no. 1, pp. 181-192, Feb. 2009.

20.   O. Anaya-Lara, N. Jenkins, J. Ekanayake, P. Cartwright, M. Hughes, "Wind Energy Generation: Modeling and Control," 2009 John Wiley & Sons, Ltd.

21.   J. L. Domínguez-García, O. Gomis-Bellmunt, F. D. Bianchi, A. Sumper, "Power oscillation damping supported by wind power: A review," Renewable and Sustain. Energy Rev., vol. 16, pp. 4994–5006, Mar. 2012.

22.   R. Shah, N. Mithulananthan, and R. C. Bansal, "Damping performance analysis of battery energy storage, ultracapacitor and shunt capacitor with large-scale PV plants," Applied Energy Special Issue Smart Grid, vol. 96, pp. 235–244, Aug. 2012.

23.   C. Zhang, X. Cai, Z. Li, A. Rygg, and M. Molinas, "Properties and physical interpretation of the dynamic interactions between voltage source converters and grid: Electrical oscillation and its stability control," IET Power Electronics, vol. 10, no. 8, pp. 894–902, Feb. 2017.

24.   X. Y. Bian, Y. Geng, K. L. Lo, Y. Fu, and Q. B. Zhou, "Coordination of PSSs and SVC Damping Controller to Improve Probabilistic Small-Signal Stability of Power System with Wind Farm Integration," IEEE Trans. Power Systems, vol. 31, no. 3, pp. 2371–2382, 2016.

25.   N. Mithulananthan, C. A. Canizares, J. Reeve, and G. J. Rogers, "Comparison of PSS, SVC, and STATCOM controllers for damping power system oscillations," IEEE Trans. Power Systems, vol. 18, no. 2, pp. 786–792, 2003.

26.   A. M. Simões, D. C. Savelli, P. C. Pellanda, N. Martins, and P. Apkarian, "Robust design of a TCSC oscillation damping controller in a weak 500-kV interconnection considering multiple power flow scenarios and external disturbances," IEEE Trans. Power Systems, vol. 24, no.1, pp. 226–236, 2009.

27.   B. Tamimi, C. Canizares, and K. Bhattacharya, "Stability impact of largescale and distributed solar photovoltaic generation: The case of Ontario, Canada," IEEE Trans. Sustain. Energy, vol. 4, no. 3, pp. 680–688, Jul. 2013.

28.   M. Yagami, N. Kimura, M. Tsuchimoto, and J. Tamura, "Power system transient stability analysis in the case of high-penetration photovoltaics," in Proc. IEEE Power Tech, Grenoble, France, 2013, pp. 1–6, No.A5306MY.

29.   W. Du, H.F. Wang, and L.-Y. Xiao, "Power system small-signal stability as affected by grid-connected photovoltaic generation," European Transactions on Electrical Power, vol. 21, pp. 688–703, 2011.

30.   R. Shah, N. Mithulananthan, and KY. Lee, "Contribution of PV systems with ultra-capacitor energy storage on inter-area oscillation,". IEEE Power Energy Society General Meeting, pp. 1–8, 2011.

31.   R. Shah, N. Mithulananthan, and R.C. Bansal, "Oscillatory stability analysis with high penetrations of large-scale photovoltaic generation," Energy Conversion and Management, vol. 65, pp. 420–429, 2013.

32.   R. Yan, N. -Masood, T. Kumar Saha, F. Bai and H. Gu, "The Anatomy of the 2016 South Australia Blackout: A Catastrophic Event in a High Renewable Network," IEEE Trans. on Power Systems, vol. 33, no. 5, pp. 5374–5388, Sept. 2018.

33.   A. Safayet, P. Fajri, and I. Husain, "Reactive power management for overvoltage prevention at high pv penetration in a low-voltage distribution system," IEEE Trans. Ind. Appl., vol. 53, no. 6, pp. 5786– 5794, Nov. 2017.

34.   Ali Q. Al-Shetwi, Muhamad Zahim Sujod, Frede Blaabjerg, "Low voltage ride-through capability control for single-stage inverter-based grid-connected photovoltaic power plant," Solar Energy, vol. 159, pp. 665–681, 2018.

35.   E. Rodrigues, A. Bizuayehu, and J.P. Catalao, "Analysis of requirements in insular grid codes for large-scale integration of renewable generation" IEEE PES T&D Conference and Exposition, Chicago, USA, 2014, pp. 1–5.

36.   T. Aziz, T. K. Saha, and N. Mithulananthan, "A review of interconnection rules for large-scale renewable power generation," Large Scale Renewable Power Generation: Springer, pp. 151–171, 2014.

37.   M. Deakin and M. McCulloch, "Voltage regulation of large scale PV: A comparative case study," IEEE Manchester Powertech, Manchester, UK, 2017, pp. 1–6.

38.   Endegnanew, A. G., Tedeschi, E., Marvik, J. I., Torres-Olguin, R. E., & d`Arco, S. (2013). 'Marinet deliverable 2.26—Collation of European grid codes' (Technical Report). Network, Marine Renewables Infrastructure.

39.   H. Maleki and R. K. Varma, "Coordinated control of PV solar system as STATCOM (PV-STATCOM) and Power System Stabilizers for power oscillation damping," 2016 IEEE Power and Energy Society General Meeting (PESGM), Boston, MA, 2016, pp. 1–5.

40.   R. K. Varma and H. Maleki, "PV solar system control as STATCOM (PV-STATCOM) for power oscillation damping," IEEE Trans. Sustain. Energy, pp. 1–1, 2018.

41.   R. K. Varma and M. Akbari, "Simultaneous Fast Frequency Control and Power Oscillation Damping by Utilizing PV Solar System as PV-STATCOM," IEEE Trans. Sustain. Energy, vol. 11, no. 1, 2020, pp. 415–425.

42.   M. Basu, V. R. Mahindara, J. Kim, and E. Muljadi, "Effect of high penetrated reactive power support-based Inverter-Based-Resources on the power stability of microgrid

distribution system during faults," 2020 IEEE Industry Applications Society Annual Meeting, Detroit, MI, 2020.

43.   H. D. Silva-Saravia, H. A. Pulgar, L. M. Tolbert, D. A. Schoenwald and W. Ju, "Enabling Utility-Scale Solar PV Plants for Electromechanical Oscillation Damping," IEEE Trans. Sustain. Energy, vol. 12, no. 1, pp. 138–147, 2020.

44.   R. Shah, N. Mithulananthan, and R. C. Bansal, "Damping performance analysis of battery energy storage, ultracapacitor and shunt capacitor with large-scale PV plants," Applied Energy Special Issue Smart Grid, vol. 96, pp. 235–244, Aug. 2012.

45.   C. Zhang, X. Cai, Z. Li, A. Rygg, and M. Molinas, "Properties and physical interpretation of the dynamic interactions between voltage source converters and grid: Electrical oscillation and its stability control," IET Power Electronics, vol. 10, no. 8, pp. 894–902, Feb. 2017.

46.   M. Singh, A. Allen, E. Muljadi and V. Gevorgian, "Oscillation damping: A comparison of wind and photovoltaic power plant capabilities," 2014 IEEE Symposium on Power Electronics and Machines for Wind and Water Applications, Milwaukee, WI, 2014, pp. 1–7.

47.   Y. Liu, L. Zhu, L. Zhan, J. R. Gracia, T. J. King, and Y. Liu, "Active power control of solar PV generation for large interconnection frequency regulation and oscillation damping," International Journal of Energy Research, vol. 40, no. 3, pp. 353–361, 2016.

48.   IEA (2022), "Wind Electricity" IEA, Paris https://www.iea.org/reports/wind-electricity, License: CC BY 4.0

49.   EERE, "Land-Based Wind Market Report-2022" https://www.energy.gov/eere/wind/articles/land-based-wind-market-report-2022-edition

50.   C. Jauch, S. M. Islam, P. Sørensen, and B. B. Jensen, "Design of a wind turbine pitch angle controller for power system stabilization," in Renewable energy, vol. 32, pp. 2334–2349, Nov. 2007.

51.   C. Jauch, T. Cronin, P. Sørensen, and B. B. Jensen, " A fuzzy logic pitch angle controller for power system stabilization," in Wind energy, vol. 10, pp. 19–30, July 2006.

52.   M. Basu, V. R. Mahindara, J. Kim, R. M. Nelms and E. Muljadi, "Comparison of Active and Reactive Power Oscillation Damping With PV Plants," in IEEE Trans. Ind. Appl., vol. 57, no. 3, pp. 2178–2186, Feb. 2021.

53.   E. V. Larsen, and D. A. Swann, "Applying power system stabilizers part I: general concepts, " in IEEE Trans. Power App. syst., vol. 6, pp. 3017-3024, June 1981.

54.   J. L. Domínguez-García, O. Gomis-Bellmunt, F. Bianchi, and A. Sumper, "Power system stabilizer control for wind power to enhance power system stability," PHYSCON, 2011.

55.   F. Giraud, "Analysis of a utility-interactive wind-photovoltaic hybrid system with battery storage using neural network," Ph.D. dissertation, Univ. Mass., Lowell, 1999.

56.   P. E. Bett and H. E. Thornton, "The climatological relationships between wind and solar energy in Britain," Renewable Energy, vol. 87, no. 1, pp. 96-110, 2016.

57.   S. Shanghavi, W. M. Grady, and B. Schwarz, "Evaluating the impact of wind turbine shadows on an integrated wind and solar farm," 2012 3rd IEEE PES ISGT Europe, Berlin, 2012, pp. 1-6.

58.   Y. Wang, J. Meng, X. Zhang and L. Xu, "Control of PMSG-based wind turbines for system inertial response and power oscillation damping," IEEE Trans. Sustain. Energy, vol. 6, no. 2, pp. 565-574, 2015.

59.   L. Xu, X. Ruan, C. Mao, B. Zhang, and Y. Luo, "An improved optimal sizing method for wind-solar-battery hybrid power system," IEEE Trans. Sustain. Energy, vol. 4, no. 3, pp. 774-785, 2013.

60.   U. Kalla, B. Singh, S. Murthy, C. Jain and K. Kant, "Adaptive sliding mode control of standalone single-phase microgrid using hydro, wind and solar pv array based generation," IEEE Trans. Smart Grid, vol. 9, no. 6, pp. 6806-6814, 2018.

61.   A. Merabet, K. Ahmed, H. Ibrahim, R. Beguenane, and A. Ghias, "Energy management and control system for laboratory-scale microgrid based wind-pv-battery," IEEE Trans. Sustain. Energy, vol. 8, no. 1, pp. 145-154, 2017.

62.   T. Hirose and H. Matsuo, "Standalone hybrid wind-solar power generation system applying dump power control without dump load," IEEE Trans. Ind. Electron., vol. 59, no. 2, pp. 988-997, 2012.

63.   A. Merabet, K. Ahmed, H. Ibrahim, R. Beguenane, and A. Ghias, "Energy management and control system for laboratory scale microgrid based wind-pv-battery," IEEE Trans. Sustain. Energy, vol. 8, no. 1, pp. 145-154, 2017.

64.   J. Zhang, X. Xie, D. Jiao and Z. Qian, "Stability problems and input impedance improvement for cascaded power electronic systems," Proc. APEC, 2004, vol.2, pp. 1018-1024.

65.   B. Mangu, S. Akshatha, D. Suryanarayana, and B. G. Fernandes, "Grid connected PV-wind-battery-based multi-input transformer-coupled bidirectional dc-dc converter for household applications," IEEE Trans. Emerg. Sel. Topics Power Electron., vol. 4, no. 3, pp. 1086-1095, 2016.

66.   International Renewable Energy Agency, IRENA, "Renewable Capacity Statistics 2020," Abu Dhabi, Apr. 2020.

67.   International Renewable Energy Agency, IRENA, "Renewable Capacity Highlights 2021," Abu Dhabi, Mar. 2021.

68.   Global Wind Energy Council (GWEC), "Global Wind Report 2021," Brussels, Nov. 2021.

69.   V. Gevorgian, S. Shah, W. Yan, and G. Henderson, "Grid-forming wind: getting ready for prime time, with or without inverters," IEEE Electrifi. Mag., vol. 10, no. 1, pp. 52–64, Mar. 2022.

70.   ESIG High Share of Inverter-Based Generation TaskForce, "Grid-forming technology in energy systems integration, 2022," [Online]. Available: https://www.esig.energy/wp-content/uploads/2022/03/ESIG-GFM-report-2022.pdf.

71.   S. Shah and V. Gevorgian, "Control, operation, and stability characteristics of grid-forming type III wind turbines," presented at the Wind Integration Workshop, Nov. 11-12, 2020.

72.   DeWind D8.2 - Technical Brochure, [Online]. Available: https://www.compositetechcorp.com/

73.   G. Henderson, "The latest development in synchronous wind turbine technology: how the LVS system can deliver low cost, broad-band variable turbine speed and type 5 grid connection," in Proc. Int. Work. on Large-Scale Inte. of Wind Power into Power Syst. as well as on Trans. Nets. for Offshore Wind Power Plants, 2021, pp. 360-366.

74.   K. E. Okedu, S. M. Muyeen, T. Rion, and T. Junji, "Wind farms fault ride through using DFIG with new protection scheme," IEEE Trans. Sustain. Energy, vol.3, no. 2, 242-254, Mar. 2012.

75.   C. Jin, and W. Peng, "Enhancement of low voltage ride-through capability for wind turbine driven DFIG with active crowbar and battery energy storage system," IEEE PES Gen. Meeting, Minneapolis, 2010, pp. 1-8.

76.   A. R. Fereidouni, V. Behrooz, and T. Hosseini, "The impact of solid state fault current limiter on power network with wind-turbine power generation," IEEE Trans. on Smart Grid, vol. 4, no. 2, pp. 1188-1196, June 2013.

77.   F. Jiang, C. Tu, Z. Shuai, M. Cheng, Z. Lan and F. Xiao, "Multilevel Cascaded-Type Dynamic Voltage Restorer With Fault Current-Limiting Function," IEEE Trans. Power Delivery, vol. 31, no. 3, pp. 1261-1269, June 2016.

78.   S. Nuzzo, M. Galea, C. Gerada and N. Brown, "Analysis, Modeling, and Design Considerations for the Excitation Systems of Synchronous Generators," IEEE Transactions on Industrial Electronics, vol. 65, no. 4, pp. 2996-3007, April 2018.

79.   T. L. Dillman, F. W. Keay, C. Raczkowsi, J. W. Skooglund, and W. H. South, "Brushless excitation," IEEE Spectr., vol. 9, no. 3, pp. 58–66, Mar. 1972.

80.   Z. Shushu, L. Chuang, N. Yinhang and T. Jie, "A Two-Stage Brushless Excitation Method for Hybrid Excitation Synchronous Generator," in IEEE Trans. on Magnetics, vol. 51, no. 6, pp. 1-11, June 2015.

81.   Fayc¸al Bensmaine, Abdallah Barakat, Slim Tnani, G´erard Champenois, Emile Mouni, "Dual control of synchronous generator for terminal voltage regulation-comparison with a single control," Electric Power Systems Research, Volume 91, 2012, Pages 78-86.

82.   R. Thornton-Jones, I. Golightly, N. Gutteridge, C. Huizer and D. Navratil, "Review of generator and excitation system specification and test requirements to satisfy multiple international grid code standards," 2012 IEEE Power and Energy Society General Meeting, San Diego, CA, 2012, pp. 1-2.

83.   J. K. Nøland, "A New Paradigm for Large Brushless Hydrogenerators - Advantages Beyond the Static System," PhD Thesis, 2017.

84.   A. Barakat, S. Tnani, G. Champenois, and E. Mouni, "Monovariable and multivariable voltage regulator design for a synchronous generator modeled with fixed and variable loads," IEEE Trans. Energy Convers, vol. 26, no. 3, pp. 811–821, 2011.

85.   M. Gunes and N. Dogru, "Fuzzy control of brushless excitation system for steam turbo generators," IEEE Trans. Energy Convers, vol. 25, no. 3, pp. 844–852, 2010.

86.   T. Hussain, J. Calderon and S. M. Alam, " Open Source High Fidelity Modeling of a Type 5 Wind Turbine Drivetrain for Grid Integration," Journal of Physics, https://doi.org/10.48550/arXiv.2305.15216.

87.   J.F. Hauer, C.J. Demeure, L.L. Scharf, "Initial results in Prony analysis of power system response signals," IEEE Transactions on Power Systems, vol. 5, no. 1, pp. 80-89, Feb. 1990.

88.   S.M. Kay and S.L. Marple, Jr., "Spectrum analysis—A modern perspective," Proceedings of the IEEE, vol. 69, no. 11, pp. 1380-1419, Nov. 1981.

89.   K. Sambarapu, "A Methodology for Estimating the Parameters of Steam Turbine Generator Shaft Systems for Subsynchronous Resonance Studies" PhD Thesis, Department of Electrical Engineering, Auburn University, Auburn, AL, 2012.

Appendix

The Matlab code for Prony Analysis of Type 5 dataset:

```
clc
clear
close all

% numModes
numModes = 14;
timestep = 0.5;

% importing data
rawData = readmatrix('WPPPVprony.xlsx');

% plotting the raw data
plot(rawData(:,1),rawData(:,2));
rawTimeStep = diff(rawData(:,1));


% start from where the oscillations begin
OscBeginID = find(abs(rawData(:,1) - 10.15)<0.0001);
OscEndID   = find(abs(rawData(:,1) - (10.15 + 40))<0.0001);
Data = rawData(OscBeginID(end):OscEndID(1),[1:2]);

% assigning as X0 and FX0 for downstream calculations
X0  = Data(:,1) - Data(1,1);
FX0 = Data(:,2);


% Interpolating raw data based on the time-step
x = [X0(1):timestep:X0(end)]';
fx = interp1(X0,FX0,x);

% Prony series calculation
fn_data = fx;


N = length(fn_data);
init_f = fn_data(1);
fn_data = fn_data(2:N)-fn_data(1:N-1);
numDataPoints = length(fn_data);

% A : #cols = number of modes
% A : #rows = number of data points - number of modes

A = zeros( numDataPoints-numModes, numModes);

for r = 1:numDataPoints-numModes
    for c = 1:numModes
        A(r,numModes-c+1) = fn_data(c+r-1);
    end
end
```

```matlab
% B is always a column vector (only one column)
% #rows = number of data points - number of modes
B = zeros( numDataPoints-numModes, 1);

for r = 1:numDataPoints-numModes
    B(r,1) = -fn_data(numModes+r);
end

X = A\B;

mu_ = roots([ 1 transpose(X)]);

vrFreqRad_n_Decay = log(mu_)/timestep;  % a1 and a2

% M : #cols = number of modes
% M : #rows = number of data points
M = zeros(numDataPoints, numModes);

for r = 1:numDataPoints
    for c = 1:numModes
        M(r,c) = (mu_(c)-1) * (mu_(c) )^(r-1);
    end
end

% F is always a column vector (only one column)
% #rows = number of data points

vrMagn_n_PhaseRad = M \ fn_data;  % C matrix
Dc_offset = init_f - sum(vrMagn_n_PhaseRad);

C = vrMagn_n_PhaseRad;
a = vrFreqRad_n_Decay;

y = zeros(length(X0),1);

% adding all the components to get resultant Prony approximation
for k = 1:numModes
    y = y + C(k)*exp(a(k).*X0);
end

% plotting the prony results vs actual data
figure(2)
hold on
plot(X0,y+mean(Data(:,2)),'.-b'); drawnow
plot(X0, FX0,'.-r');
legend('Prony','RawData')

xlim([-10 50])
xlabel('time (sec)')
ylabel('Active Power (p.u.)')
set(gcf,'color','w');
box on
```